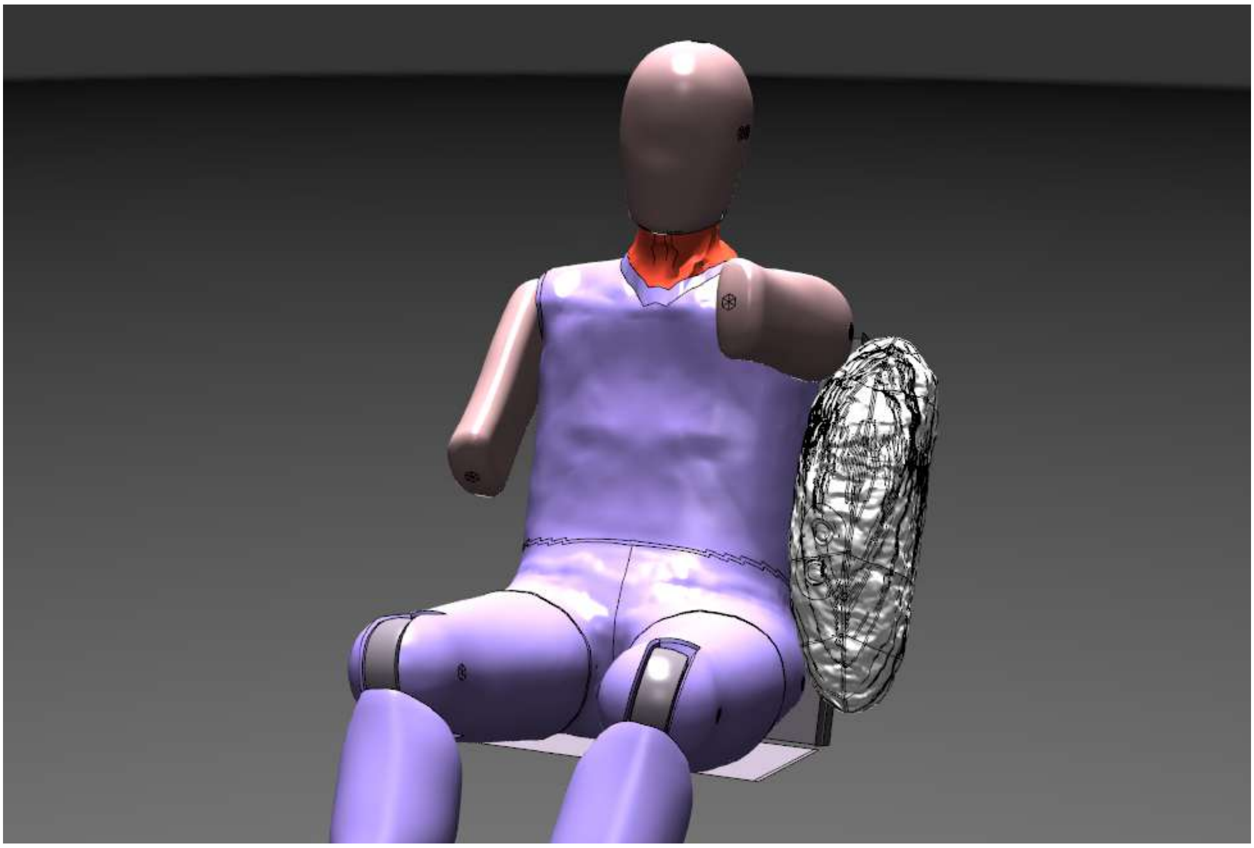

Evaluation of Advanced Gas Simulation Methodologies for Side Impact Airbags

A Comparative Study of CPG and CPM during the deployment interaction phase

Master's thesis in Mobility Engineering

ABHAY CHOUHAN
ELLIOT JONSSON

DEPARTMENT OF MECHANICS AND MARITIME SCIENCES
CHALMERS UNIVERSITY OF TECHNOLOGY
Gothenburg, Sweden 2026
www.chalmers.se

Master's Thesis in Mobility Engineering

Evaluation of Advanced Gas Simulation Methodologies for Side Impact Airbags

A Comparative Study of CPG and CPM during the deployment interaction phase

ABHAY CHOUHAN
ELLIOT JONSSON

CHALMERS
UNIVERSITY OF TECHNOLOGY

Department of Mechanics and Maritime Sciences
Division of Vehicle Safety
Chalmers University of Technology
Gothenburg, Sweden 2026

Evaluation of Advanced Gas Simulation Methodologies for Side Impact Airbags
A Comparative Study of CPG and CPM during the deployment interaction phase

Supervisors: Rahul Waghe & Jacob Wass, Volvo Cars Corporation
Examiner: Johan Iraeus, Department of Mechanics and Maritime Sciences

Master's Thesis 2026
Department of Mechanics and Maritime Sciences
Chalmers University of Technology
SE-412 96 Gothenburg
Sweden
Telephone +46 31 772 1000

Cover: Virtual simulation rendering of a Humanetics Hybrid III 5th percentile female anthropomorphic test device interacting with a side airbag. The image was captured using MetaPost software from BETA CAE Systems.

Typeset in LaTeX
Gothenburg, Sweden 2026

Evaluation of Advanced Gas Simulation Methodologies for Side Impact Airbags
A Comparative Study of CPG and CPM during the deployment interaction phase
ABHAY CHOUHAN
ELLIOT JONSSON
Department of Mechanics and Maritime Sciences
Division of Vehicle Safety
Chalmers University of Technology

Abstract

Side airbags are time-critical restraint systems in which gas flow, fabric deformation, and occupant contact strongly influence the predicted response. This thesis evaluates the recently introduced Continuum Particle Gas (CPG) method for side-airbag deployment simulations and compares it with the established Corpuscular Particle Method (CPM). The aim is to assess whether CPG improves the representation of side-airbag behaviour and occupant interaction during early deployment.

The comparison was performed through an inflator tank test, a linear impactor setup, and simplified airbag–occupant interaction tests. Several Anthropomorphic Test Device configurations and arm positions were investigated. The methods were evaluated using airbag pressure response, unfolding behaviour, arm trajectory, selected occupant-related response quantities, and computational time. Physical test data and Volvo Cars reference models were used as comparison bases where available.

The results show that both CPM and CPG capture the general pressure development and deployment response. However, CPG generally shows closer agreement with physical tests during early deployment, particularly regarding local airbag shape, crease formation, unfolding behaviour, and arm trajectory. CPG also shows improved agreement in several numerical occupant-related response metrics. During later pressure decay, CPM more often approaches the physical test pressure level, while CPG tends to remain slightly higher.

The main limitation of CPG is its substantially higher computational cost compared with CPM. This indicates that it is currently more suitable as a complement to CPM rather than a direct replacement. This is especially relevant in cases where detailed early deployment behaviour and local gas-flow effects are important.

Keywords: Side airbag, airbag deployment, occupant safety, side impact, CAE, LS-DYNA, Continuum Particle Gas, Corpuscular Particle Method, Anthropomorphic Test Device, airbag–occupant interaction

Preface

This report presents the outcome of our master's thesis project carried out at the Department of Mechanics and Maritime Sciences at Chalmers University of Technology during the spring of 2026. The thesis was carried out in collaboration with Volvo Cars Corporation and was conducted over six months of full-time work by two students from the Mobility Engineering master's programme. AI-based language tools were used during the writing process for proofreading, language refinement, and support in improving the academic formulation of the report.

Acknowledgements

As this project marks the completion of our master's studies, we would like to express our sincere gratitude to everyone who enabled the project from its inception and supported us throughout the process. We would particularly like to thank Johan Iraeus, Examiner at Chalmers University of Technology, for his interest in the project, his valuable feedback throughout the work, and his representation of the students' perspective in interactions with industry. We would also like to thank our industry supervisors, Rahul Waghe & Jacob Wass, for their substantial contributions at Volvo Cars. This project would not have been possible without their comprehensive introduction to the work and continuous technical support.

We would also like to extend our special thanks to the entire Side Airbag and Child Safety team at Volvo Cars, as well as to Malin Wetterlind, our project manager, for warmly welcoming us as thesis students.

Finally, we would like to thank everyone else involved in the project, including the test engineers, technical experts, software developers, and many others who contributed to the work. The project has been both highly rewarding and thoroughly enjoyable.

Abhay Chouhan, Elliot Jonsson, Gothenburg, June 2026

List of Acronyms

Below is the list of acronyms that have been used throughout this thesis listed in alphabetical order:

ATD	Anthropomorphic Test Device
CAE	Computer-Aided Engineering
CPG	Continuum Particle Gas
CPM	Corpuscular Particle Method
CPU	Central Processing Unit
FE	Finite Element
FEA	Finite Element Analysis
IIHS	Insurance Institute for Highway Safety
LHS	Left-hand side
MPP	Massively Parallel Processing
OoP	Out-of-Position
SAB	Side Airbag
SID-IIs	Small Side-impact dummy
TTF	Time to Fire
VCC	Volvo Cars Corporation
WorldSID-50M	Worldwide Harmonized Side Impact Dummy

Nomenclature

The following nomenclature summarizes the indices, sets, parameters, and variables used throughout this thesis.

Indices and Sets

i	Response signal index
c	Test-case index
s	Gas species index
m	Gas method, where $m \in \{\mathrm{CPM}, \mathrm{CPG}\}$
F	Response family used for grouped evaluation

Parameters

γ	Heat capacity ratio
n_s	Number of gas species
n_F	Number of response signals included in response family F
n_c	Number of test cases included in a grouped family-level average
f_s	Static friction coefficient
f_d	Dynamic friction coefficient

Variables

p	Gas pressure
W_k	Total translational kinetic energy of CPM particles
V	Airbag volume
U	Conservative state-variable vector used in the CPG formulation
ρ	Gas density
u_x, u_y, u_z	Gas velocity components in the x-, y-, and z-directions
$\mathbf{u}$	Gas velocity vector
E	Total gas energy
Y_s	Mass fraction of gas species s
R	Final reliability score
R_{phys}	Physical repeatability score
R_{CAE}	CAE comparability score
$\bar{x}_{\text{test},i}$	Physical-test reference value for response signal i
$x_{\text{Test 1},i}$	Signed peak response value from physical Test 1 for response signal i
$x_{\text{Test 2},i}$	Signed peak response value from physical Test 2 for response signal i
$x_{m,i}$	Signed peak response value from CAE method m for response signal i
$\Delta_{m,i}$	Signed deviation between CAE method m and the physical-test reference for response signal i
$\lvert\Delta_{m,i}\rvert$	Absolute deviation between CAE method m and the physical-test reference for response signal i
$E_{m,F}$	Case-level mean absolute difference for CAE method m and response family F
$E_{m,F,c}$	Case-level mean absolute difference for CAE method m, response family F, and test case c
$\bar{E}_{m,F}$	Overall family-level mean absolute difference for CAE method m and response family F
I_F	Relative reduction in mean absolute difference between CPM and CPG for response family F

Contents

List of Figures

List of Tables

1

Introduction

This chapter introduces the project by presenting its background, purpose, aim and objectives, scientific research questions, and limitations. The background explains the relevance of the subject, while the purpose, aim and objectives, and scientific research questions define the project-specific approach. Finally, the limitations clarify the aspects that are not investigated within the scope of the project.

1.1 Background

Airbags play a crucial role in protecting vehicle occupants and reducing the risk of severe injuries during traffic accidents. Side Airbags (SABs) are particularly important in side-impact collisions, where the clearance between the impacting structure and the occupant is limited. This makes the deployment phase highly time-critical, as the SAB must rapidly provide protection for body regions such as the thorax, pelvis, and ribs. Consequently, small differences in early unfolding behaviour may influence the subsequent occupant–airbag interaction.

During the development of SABs, both physical testing and virtual testing through Computer-Aided Engineering (CAE) are used. Physical testing with Anthropomorphic Test Devices (ATDs) enables observation of occupant, airbag, and surrounding-structure behaviour in controlled crash scenarios. However, such testing is time-consuming, expensive, and limited in terms of detailed analysis. CAE is therefore used as a complementary tool, offering improved repeatability and access to detailed response quantities. A key challenge in virtual simulations is to accurately represent the physical environment, particularly the gas flow during airbag inflation.

Airbag deployment is a fluid–structure interaction between the gas, fabric, and occupant. The gas model used in the simulation affects the unfolding behaviour, pressure response, and ultimately the predicted arm trajectory. The currently used method is the Corpuscular Particle Method (CPM), which represents the gas motion using a simplified particle-based approach. CPM provides a good balance between prediction accuracy and computational cost, but may compromise the representation of local gas flow, early deployment behaviour, and complex interactions. A newer method introduced in the industry, the Continuum Particle Gas (CPG) method, uses a more complex and realistic representation of continuous gas flow. This method is intended to better capture local gas flows, pressure gradients, and early unfolding behaviour. CPG is therefore expected to provide a more realistic airbag deployment response, but also to require a higher computational cost.

From an industrial perspective, the selection of an appropriate gas modelling method is important because simulation accuracy must be balanced against computational efficiency in the vehicle safety development process. A more representative gas model may support earlier and more reliable safety-related design decisions, while increased computational cost may limit its practical use. This provides the basis for comparing CPM and CPG in the present work, with focus on their influence on SAB deployment and occupant interaction.

1.2 Purpose

The purpose of the thesis is to conduct a comparison between two gas modelling methods for SAB inflation; CPG and CPM.

1.3 Aim & Objective

The overall aim of the project is to compare the CPG with CPM and to conclude which model better captures the real life response of SAB interaction with occupants.

The following objectives are defined:

- Validate the CPG and CPM inflator pressure response against physical reference in a tank test.
- Tune the CPG setup using a linear impactor model.
- Compare CPM and CPG in simplified rigid-seat test cases. Evaluate the methods using pressure response, unfolding behaviour, arm trajectory, and relevant Occupant Injury Criteria.
- Assess the computational cost of the methods and discuss the suitability of CPG compared to CPM.

1.4 Scientific research questions

While the aim describes the overall intention of the work and the objectives outline the practical steps taken, the research questions specify the scientific issues that the project seeks to investigate. They translate the aim into focused and measurable lines of inquiry that guide the analysis and evaluation of the CPG method. Based on the project aim, the following research questions are formulated:

1. Which differences does CPG demonstrate relative to CPM in reflecting airbag unfolding behaviour in CAE during the initial airbag deployment?
2. How does the predicted arm trajectory and loading response differ when using CPG versus CPM?

3. Considering computational cost and simulation fidelity, in which applications is CPG more suitable, and in which applications does CPM remain more appropriate?

1.5 Limitations/Demarcations

This chapter defines the boundaries of the thesis work by clarifying what aspects of SAB modelling and gas-method evaluation are included and excluded. Regulatory compliance, consumer-assessment scoring, and exact injury-criteria evaluation are outside the scope of this thesis. The focus is limited to the interaction between the SAB and occupant model during deployment, and to the comparison between the CPM and CPG airbag simulation methods. A detailed summary of these boundaries is provided in Table 1.1.

Table 1.1: Scope and delimitations of the thesis work.

Category	In scope	Out of scope
System	SAB system	Full-scale vehicle crash, other airbags, seatbelt
Gas modelling methods	CPM & CPG	UPM & ALE
Test Environment	Rigid seat model & plexiglass wall	Detailed seat structures, cushioning, real door panel
Test envelope	Static SAB deployment setup.	Dynamic SAB crash scenario with vehicle motion, crash pulse, and structural intrusion.
Occupant Models	ATD	Human Body Models
Injury-related response metrics	Occupant injury criteria values and response plots are used to compare CAE results with corresponding physical test data.	No assessment of occupant injury risk is performed.
Resources	LS-DYNA, ANSA, META, Oasys PRIMER, D3PLOT	External software not used at Volvo Cars
Timeline	≈ 20 weeks, full time	Significantly shorter or longer than 20 weeks

2 Theory

This chapter presents the theoretical background required to understand the methods and analyses used in this thesis. The chapter introduces Side Airbag systems, occupant models, finite element modelling, and the airbag inflation methods relevant for CAE-based side-impact simulations.

2.1 Characteristics of Side Airbags

SABs are commonly integrated into the outboard side of the seat backrest, close to the door-side occupant environment, as illustrated in Figure 2.1. Balavich et al. [5] describe seat-mounted side-impact airbags as systems packaged in the outboard seat bolster, which must deploy from the seat and move into position between the occupant and the interior door surface before the available gap closes. SABs are therefore designed for rapid deployment in a confined lateral space. Schneider et al. [26] further describe thorax–pelvis SABs as a means of reducing thoracic and pelvic injury levels in side-impact crashes [24].

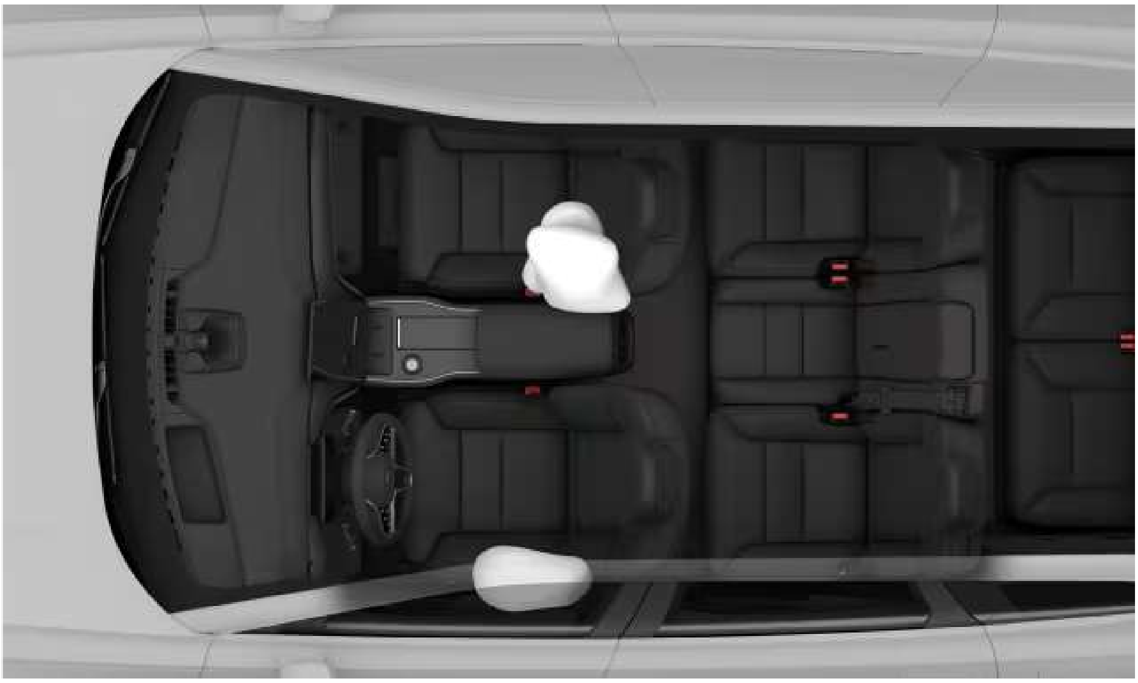

Figure 2.1: Top-down view of a Volvo EX90 illustrating the mounting and deployment of a SAB, designed to protect the occupant's thorax and pelvis [29].

The airbag fabric structure must withstand the pressure and mechanical loading associated with rapid deployment. Airbag fabrics are commonly woven textile structures, typically made from coated or uncoated synthetic materials, where low air permeability, flexibility, tensile strength, and durability are important material requirements [21]. Due to the limited packaging space, SABs are smaller than many frontal airbags. Porkolab and Lakatos [24] report typical SAB volumes in the range of approximately 15–20 litres, with short time-to-fire values. Depending on the protection target, SABs may also be designed with separate regions or chamber-like subdivisions to address different body areas. Schneider et al. [26], for example, studied a thorax–pelvis SAB concept in which the airbag was divided into upper, middle, and lower regions with different design parameters.

The inflation of the SAB may be driven by a hybrid inflator, which combines stored compressed gas with a limited amount of pyrotechnic material to achieve the required deployment performance [4]. Once deployed, the airbag should provide controlled deceleration of the occupant rather than acting as a rigid barrier. This behaviour is influenced by gas outflow through vent openings and leakage through the fabric. Hirth et al. [7] describe vent-hole design, material behaviour, porosity, and gas–fabric interaction as important aspects of airbag deployment simulation, while Lin et al. [18] show that inflator characteristics, venting, and fabric-related heat transfer can influence the predicted pressure response and deployment behaviour.

From a CAE perspective, SAB deployment represents a strongly transient interaction between gas flow, fabric deformation, venting, and contact with the occupant model. The limited space and short deployment time make the predicted airbag shape, pressure development, and local interaction behaviour sensitive to the selected modelling approach. This is consistent with Hirth et al. [7], who describe the need to represent the interaction between internal gas flow and the deforming airbag structure, and with Lin et al. [18], who evaluate particle-based airbag modelling for side-impact airbag deployment applications.

2.2 Explicit Finite Element Analysis

Finite element analysis (FEA) is a numerical method used to approximate the mechanical response of complex structures by dividing the physical domain into a finite number of elements connected through nodes. Within FEA, dynamic problems may be solved using either implicit or explicit time integration schemes. In explicit time integration, the equations of motion are evaluated based on the known response from the previous time step, whereas implicit methods evaluate the response at the new time step [2]. This makes explicit integration particularly relevant for transient dynamic problems where the response changes rapidly over time.

Explicit FEA is commonly applied in crash and restraint-system simulations because these problems involve short-duration loading, large deformation, complex contact interactions, and nonlinear material behaviour. Khalil and Sheh [15] describe FE crash simulation as a nonlinear mechanics problem and present an integrated vehicle–dummy–airbag model for occupant protection analysis. In this type of simulation, the response of the model is advanced incrementally in time, making the method suitable for load cases where geometry, loading, and contact conditions change rapidly.

A characteristic feature of explicit analysis is that small time steps are required to maintain numerical stability. The Ansys Explicit Dynamics Theory Guide states that explicit time integration uses a central-difference scheme and that the time step is limited by the Courant–Friedrichs–Lewy stability condition [3]. The stable time step is influenced by the characteristic element dimension and the local material sound speed, meaning that small elements can reduce the allowable time step and increase the number of increments required for the simulation [3]. For airbag simulations, this is relevant because the deployment process occurs over a short time period and involves interaction between the airbag fabric, gas inflation, surrounding structures, and occupant model.

2.3 CAE Modelling for Airbag Simulations

Airbag deployment simulations are commonly performed using explicit FE CAE methods due to the short-duration and highly dynamic nature of the deployment event. Hirth et al. [7] describe airbag deployment simulation as a standard application of explicit FE codes, where the numerical model is used to represent the interaction between the inflating gas and the deforming airbag structure. In this context, the physical system is represented through numerical models that approximate the mechanical and physical behaviour relevant to the investigated load case.

A CAE model for airbag simulation may include several interacting parts, such as structural vehicle components, an occupant model represented by a FE ATD model, the airbag fabric structure, gas inflation, venting, and contact definitions. Humanetics describes virtual crash-test dummy models as numerical counterparts to physical ATDs, developed using geometry and material data from physical dummy design and testing [11]. The LS-DYNA Keyword User's Manual provides the corresponding modelling framework for defining airbag inflation, fabric material behaviour, contact interactions, and other model components used in explicit crash simulations [1].

Airbag deployment is a highly dynamic and nonlinear process involving gas flow, fabric deformation, pressure development, and contact interaction. Hirth et al. [7] describe how airbag simulation has developed from simplified pressure-based methods towards more detailed approaches that include deployment kinematics, vent-hole design, material behaviour, porosity, and the interaction between internal gas flow and the fabric airbag structure. Lin et al. [18] further show that modelling choices related to inflator characteristics, venting, fabric heat transfer, and gas representation can influence the predicted pressure response and deployment behaviour. The following sections therefore describe the element formulations and airbag inflation methods relevant for CAE-based airbag simulations.

2.3.1 Element Formulations

In FEA, the structure is discretised using elements with different theoretical assumptions and mechanical capabilities. Wai et al. [30] show that the choice of element type should be adapted to the geometry of the structure, the desired analysis results, and the available computational resources. Therefore, different element formulations may be used for different parts of a model.

The element formulations relevant to this thesis include shell, membrane, solid, beam, and discrete elements. Shell elements are commonly used for thin structural components where bending stiffness is relevant, while membrane elements are suitable for thin and flexible fabric components that mainly carry tensile loads. Solid elements can be used for components where three-dimensional stress states are important, whereas beam and discrete elements are typically applied when simplified structural or connection behaviour is sufficient. The specific definitions and available formulations for these element types are described in the LS-DYNA Keyword User's Manual [1].

2.3.2 Airbag Inflation Modelling

Airbag deployment in CAE requires a gas modelling method because the structural response of the airbag fabric is governed by the inflation process and by the interaction between the gas and the surrounding fabric. The model must therefore represent the relevant parts of the inflation sequence, including pressure build-up, gas inflow from the inflator, venting, fabric motion, and contact with the occupant or surrounding structures. Hirth et al. describe airbag deployment simulation as a problem in which both the gas dynamics and the coupling between the gas and the deforming airbag structure must be represented to capture the deployment behaviour [7]. The LS-DYNA Keyword User's Manual also describes several airbag formulations with different levels of modelling detail, ranging from simplified pressure-based approaches to more advanced gas-flow methods [1].

Different airbag modelling approaches are therefore available depending on the purpose of the simulation. Uniform-pressure or control-volume-based methods represent the gas response in a simplified internal volume and are mainly suited to cases where the global pressure response is of primary interest [1], [19]. ALE-based airbag modelling represents the gas in an Eulerian fluid domain coupled to the deforming Lagrangian airbag structure, allowing spatial gas-flow effects to be considered [7], [19]. Particle-based methods, such as CPM, instead describe the gas using particles and have been applied to side-impact airbag deployment simulations in LS-DYNA [18]. The newer CPG method is also defined as a particle-based gas solver, but uses a continuum-based formulation intended to improve the representation of gas-flow behaviour during airbag deployment [1], [31]. These approaches provide different levels of physical detail and computational demand, and the selected method should therefore reflect the objective of the simulation.

2.3.3 Corpuscular Particle Method

CPM is a particle-based gas modelling approach used for airbag inflation simulations in LS-DYNA. In CPM, the gas is represented by numerical particles that move within the airbag volume and interact with each other and with the surrounding fabric structure through momentum exchange [1], [18]. This principle is schematically illustrated in Figure 2.2, where particles with mass m_i and velocity v_i move within the airbag volume V. The enlarged views illustrate the two main interaction mechanisms considered in this representation: particle–particle interaction and particle–fabric interaction.

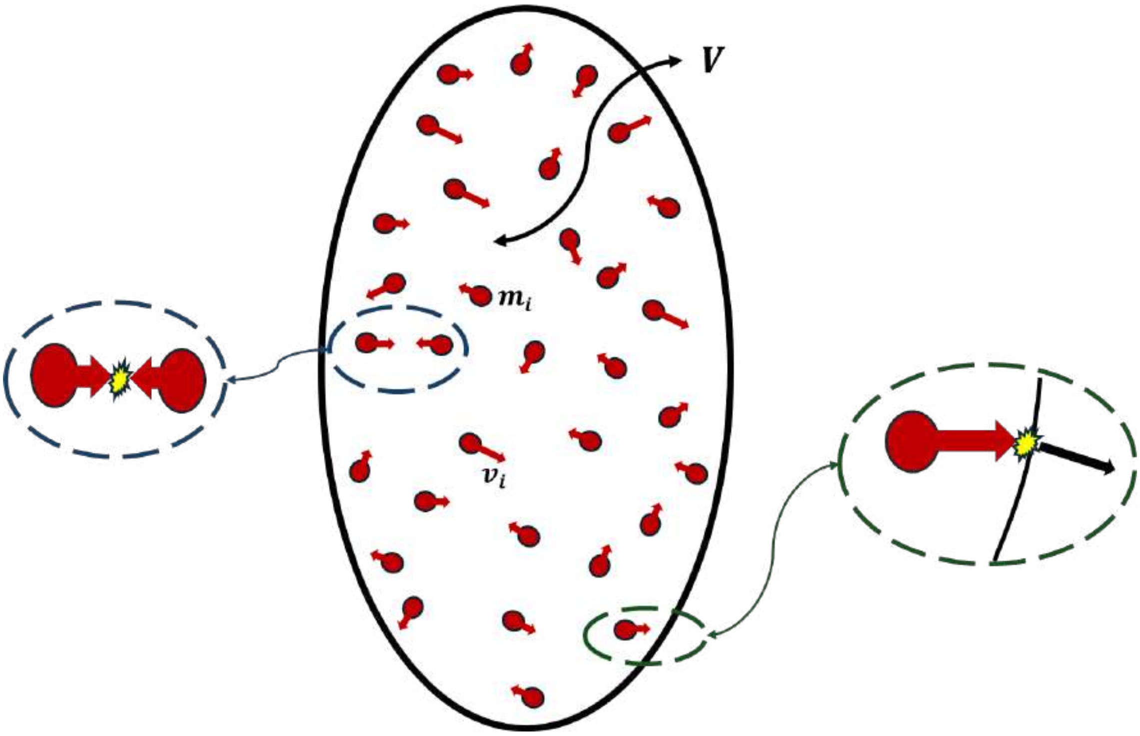

Figure 2.2: Simplified schematic illustration of CPM, where numerical particles move within the airbag volume V. The enlarged views illustrate particle–particle interaction and particle–fabric interaction.

This differs from uniform-pressure or control-volume-based methods, where the gas response is represented in a simplified internal volume. Since CPM resolves the gas through discrete particles, it can represent local gas-flow effects, such as inflator jet directionality and non-uniform pressure loading, to a greater extent than simplified pressure-based methods [18], [19]. This is particularly relevant during the early deployment phase and during initial occupant contact, where the airbag response may be influenced by local gas behaviour [18].

The pressure formulation used in CPM is based on the kinetic-theory relation between particle motion and gas pressure. According to the LS-DYNA Keyword User's Manual, the pressure can be related to the translational kinetic energy of the particles as [1]

$$p = \frac{2}{3}\frac{W_k}{V}, \tag{2.1}$$

where W_k is the total translational kinetic energy of the particles and V is the airbag volume. The pressure is directly related to the kinetic energy of the particle system and inversely related to the airbag volume. This means that, for a given volume, an increase in particle kinetic energy corresponds to an increase in the predicted gas pressure. The CPM pressure loading is therefore generated from the motion of the particles inside the airbag and their interaction with the surrounding fabric structure.

2.3.4 Continuum-based Particle Gas

CPG is a particle-based airbag gas modelling approach available in LS-DYNA. Although it uses a particle framework, the gas is described through continuum flow variables rather than as independent corpuscular particles [1], [31]. This principle is schematically illustrated in Figure 2.3, where a continuum-based particle distribution is shown within the airbag volume V, together with local continuum-particle interaction and distributed pressure loading on the airbag fabric. This formulation enables CPG to describe local gas-flow behaviour, pressure development, inflator jet effects, and flow through confined regions [31]. Such effects are relevant for SAB deployment, where limited space and early interaction between the inflating airbag, surrounding structures, and occupant model may influence the predicted response.

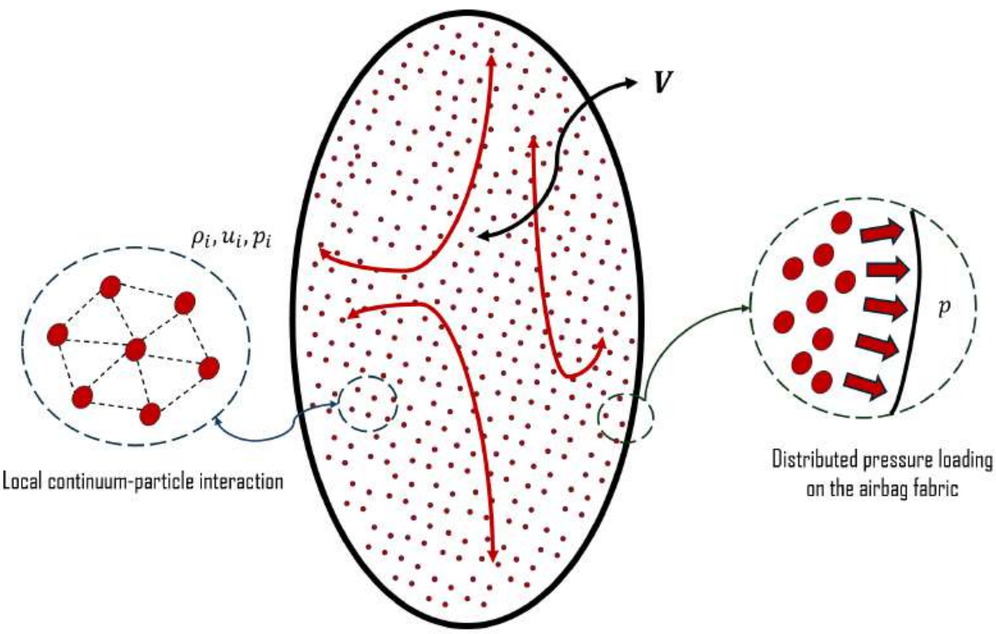

Figure 2.3: Simplified schematic illustration of CPG, where the gas is represented by a continuum-based particle distribution within the airbag volume V. The enlarged views illustrate local continuum-particle interaction and distributed pressure loading on the airbag fabric.

The governing gas state in CPG is described using conservative flow variables. Following the CPG formulation presented by Yreux et al. and the LS-DYNA documentation, the conservative state vector used to represent the gas state is given in Equation (2.2) [1], [31]:

$$\mathbf{U} = \{\rho, \rho u_x, \rho u_y, \rho u_z, E, Y_1, \ldots, Y_{n_s}\}, \tag{2.2}$$

where ρ is the gas density, ρu_x, ρu_y, and ρu_z are the momentum components, E is the total energy, and Y_s are the gas species mass fractions. The state vector shows that the gas particles in CPG carry continuum flow quantities such as density, momentum, energy, and species information. This illustrates that CPG is not only based on particle motion, but also on a continuum description of the gas state.

The pressure is then obtained from the continuum energy relation. Using the same formulation, the local gas pressure at CPG point i is expressed by Equation (2.3) [1], [31]:

$$p_i = (\gamma - 1)\left(E_i - \frac{1}{2}\rho_i |\mathbf{u}_i|^2\right). \tag{2.3}$$

Here, $\mathbf{u}_i = (u_{x,i}, u_{y,i}, u_{z,i})$ is the local gas velocity vector at CPG point i, and E_i is the corresponding local total energy density. The term $\frac{1}{2}\rho_i |\mathbf{u}_i|^2$ represents the local kinetic-energy contribution. The pressure relation therefore shows that the local pressure is calculated from the internal-energy part of the total energy density after subtracting the kinetic-energy contribution associated with the gas velocity field. Together, the state vector and pressure relation show how CPG represents the gas using continuum flow variables while still operating within a particle-based framework.

2.4 Physical and Virtual Occupant Models

In the development and evaluation of automotive restraint systems, occupant kinematics and injury-related responses are assessed using both physical and virtual human surrogates. ATDs are standardized physical crash-test dummies used in vehicle safety testing. In 49 CFR Part 572, ATDs are described as devices used for compliance testing of motor vehicles and motor vehicle equipment, with design and performance criteria intended to provide repetitive and correlative results under similar test conditions [20]. To complement physical testing, computational ATD models are used within CAE environments. These virtual FE dummy models represent the geometry, mass distribution, and mechanical response of their corresponding physical ATDs, allowing occupant response to be evaluated numerically before or alongside physical testing [11]. Different ATDs are developed for different crash configurations, such as frontal, rear, and side-impact loading.

Occupant protection must account for differences in occupant size and body shape. Modern crash-test dummies are therefore commonly described using percentile classifications, where the dummy size is related to anthropometric dimensions in the population. Humanetics explains that a 50th percentile male dummy represents a body size larger than 50% of the adult male population, while a 95th percentile male dummy represents a body size larger than 95% of that population [6]. These percentile classifications provide a practical way of representing different occupant sizes in crash testing, although they cannot fully describe the complete diversity of vehicle occupants [6].

Physical and virtual occupant models have complementary roles in vehicle safety development. Physical testing with ATDs provides measured dummy responses from controlled crash or sled tests, while virtual testing enables corresponding load cases to be evaluated numerically. Euro NCAP describes validation as the process of determining how well a model represents the real-world response for its intended use, where model predictions are compared with physical reference data [28]. In this context, physical testing provides a reference for assessing the predictive capability of the CAE model, while virtual testing supports repeated analyses and parameter variations before or alongside hardware testing. In this thesis, this combined physical and virtual approach is used to compare physical ATD configurations with corresponding virtual models in side-impact airbag loading cases.

2.4.1 The SID-IIs ATD by Humanetics

The small side-impact dummy (SID-IIs) is an ATD currently supplied by Humanetics. According to Humanetics, the SID-IIs was introduced in the mid-1990s for the evaluation of advanced automotive side-impact protection systems, particularly SABs [10], [13]. The dummy is based on the Hybrid-III 5th female ATD and represents a small occupant, corresponding approximately to a 5th percentile female or a 12–13-year-old child, with a height of about 1.50 m and a mass of approximately 44 kg [10], [13].

The SID-IIs is specifically intended for side-impact applications and is therefore relevant for evaluating occupant response in lateral crash scenarios. In these cases, the interaction between the occupant, restraint system, SAB, seat, and surrounding vehicle structures is of particular importance.

In physical testing, the SID-IIs is used to assess occupant kinematics and loading for smaller occupants during side-impact events. The Insurance Institute for Highway Safety (IIHS) side-impact rating guidelines, for example, use instrumented SID-IIs dummies representing small 5th percentile women in both the driver and rear passenger positions [14]. In this thesis, the SID-IIs is used as one of the occupant models for comparing the physical ATD configuration with the corresponding virtual model, as illustrated in Figure 2.4.

(a) Front view. **(b)** Left-Hand Side view. **(c)** Angled view.

Figure 2.4: Visual representation of the SID-IIs ATD.

2.4.2 The WorldSID-50M ATD by Humanetics

The Average Male Worldwide Harmonized Side Impact Dummy (WorldSID-50M) by Humanetics is a side-impact ATD representing a 50th percentile adult male occupant. It is developed for side-impact crash testing and is used to evaluate occupant response under lateral loading conditions. The ATD has an overall size of approximately $1100.0 \times 484.3 \times 1120.8$ mm, a seated height of 877.4 mm, and a total mass of 76.7 kg [12].

Compared with smaller occupant models such as the SID-IIs, the WorldSID-50M represents an average-sized adult male occupant. Its size and mass make it suitable for evaluating side-impact occupant response in relation to thoracic, pelvic, and shoulder loading. A visual representation of the ATD is shown in Figure 2.5.

(a) Front view. **(b)** Left-Hand Side view. **(c)** Angled view.

Figure 2.5: Visual representation of the WorldSID-50M ATD.

2.4.3 Hybrid III ATD by Humanetics

The Hybrid III ATD by Humanetics is 5th percentile female ATD that was created using a scaled down version of its Hybrid 50th male counterpart. The dummy has an overall size of approximately $653.3 \times 361.2 \times 153.2$ mm, a seated height of 787.4 mm, and a total mass of 49 kg [9]. A visual representation of the ATD is shown in Figure 2.6.

(a) Front view. **(b)** Left-Hand Side view. **(c)** Angled view.

Figure 2.6: Visual representation of the Hybrid III 5th female ATD.

2.4.4 Instrumentation in Side-Impact ATDs

Side-impact ATDs are equipped with instrumentation to measure occupant response during lateral loading. In the SID-IIs user manual, Humanetics specifies that the dummy can be equipped with several measurement channels, including accelerometers, load cells, and other sensors in body regions such as the head, neck, shoulder, thorax, spine, abdomen, pelvis, and ribs [8]. These sensors allow the physical dummy response to be quantified during impact testing and provide measurable response quantities that can be compared with corresponding outputs from CAE simulations.

For side-impact applications, thoracic and pelvic responses are of particular importance. The IIHS side-impact rating guidelines include several injury-related response quantities from these regions, such as thoracic rib deflection, abdominal rib deflection, shoulder deflection, shoulder force, pelvic acceleration, and pelvic force [14]. IIHS further states that dummy injury measures in side-impact tests often reach their peak values while the dummy is loaded by the SABs, intruding structure, or interior trim components [14]. This supports the relevance of evaluating rib deflections, thoracic accelerations, pelvic accelerations, and shoulder responses when assessing occupant interaction during side-impact loading. In virtual models, equivalent response quantities can be extracted from corresponding nodal or element-based locations, allowing comparison between physical and numerical results.

2.4.5 Dummy Pre-Positioning and Seat Squashing

Dummy pre-positioning is an important preparation step in occupant safety simulations, since the initial posture, contact state, and interaction with the seat may influence the subsequent occupant response. In simulation-based positioning procedures, the occupant model is moved into the desired posture while accounting for the geometrical constraints of the surrounding vehicle interior [16], [17].

A common approach is to use a pre-simulation in LS-DYNA, where selected dummy or occupant regions are guided towards a target position rather than being positioned only through rigid transformations in a pre-processor. Oasys PRIMER provides such a dummy-positioning workflow, where an LS-DYNA positioning analysis can be generated to move the occupant model towards the intended configuration [22]. Similar simulation-based positioning procedures have also been described using marionette-type methods, where selected body landmarks or regions are guided towards a desired posture during the pre-simulation [16].

Seat squashing is closely related to this positioning step and refers to the adjustment of the seat shape to represent compression caused by the occupant weight [16]. By including seat squashing in the pre-positioning procedure, the occupant-seat contact condition can be established before the main impact or deployment simulation.

3
Methodology

This chapter presents the methodology used to evaluate and compare the CPM and CPG airbag modelling approaches. It describes the verification steps performed before the complete airbag–occupant interaction simulations, followed by the physical and virtual test setups, instrumentation, evaluation strategy, and computational-time assessment.

3.1 Airbag Inflator Model – Tank Test

Before implementing CPM and CPG in the complete airbag–occupant interaction setup, the inflator model was evaluated in a simplified tank test configuration. This step was performed to verify the pressure response generated by the inflator under controlled conditions, before introducing additional complexities such as airbag fabric deformation, occupant interaction, contact conditions, and surrounding test rig components.

The tank test consists of an airbag inflator positioned inside a closed and rigid container, as shown in Figure 3.1. The tank volume was 28.3 L in both the CAE model and the corresponding physical test setup. When the inflator is activated, gas is released into the enclosed volume, resulting in a pressure build-up inside the tank. Since the tank does not deform and no occupant interaction is present, the pressure-time response becomes the primary quantity used to evaluate the inflator behaviour.

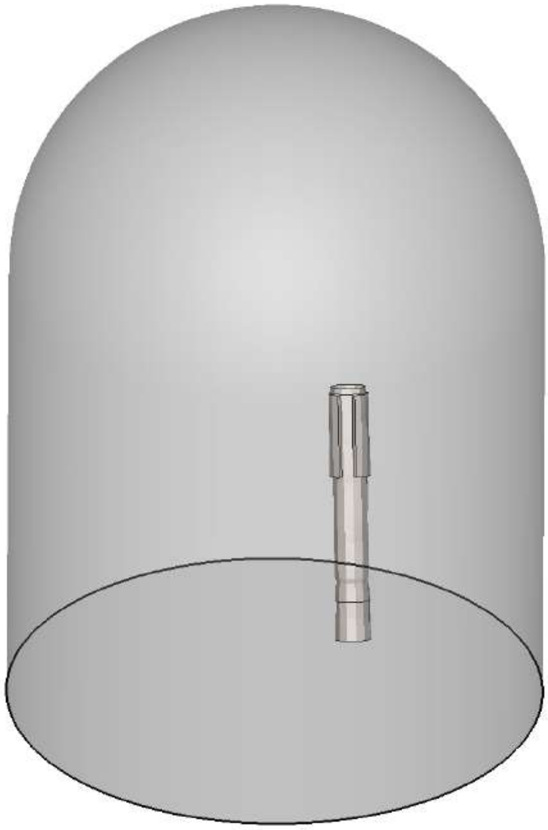

Figure 3.1: Transparent tank test model showing the inflator positioned inside the rigid tank.

The pressure response from the CAE simulations was compared with corresponding physical tank test data. The inflator input data used in the CAE simulations were provided by VCC and were applied consistently for the CPM and CPG models. Due to confidentiality restrictions, the detailed inflator input parameters are not presented in this report. The comparison focused on the pressure build-up, peak response, timing of the peak, and overall shape of the pressure-time curve. These quantities were used to assess whether CPM and CPG produced a physically reasonable inflator response before the methods were applied to the more complex rigid-seat test setup.

In the physical tank test, pressure was measured at different sensor locations inside the tank. In the CAE simulations, no specific pressure probe was modelled. Instead, the pressure response was evaluated using the average pressure inside the tank. This difference should be considered when comparing the physical and numerical pressure responses, since the physical measurements may be influenced by the local sensor position relative to the inflator outlet and the surrounding tank geometry, whereas the CAE response represents a spatially averaged pressure quantity.

By using the tank test as an initial verification case, differences related specifically to the inflator and gas modelling could be evaluated separately from the full airbag deployment environment. This provided a controlled basis for assessing the suitability of the inflator model prior to its implementation in the complete airbag–occupant interaction simulations.

3.2 Airbag Interaction Response – Linear Impactor Test

Following the tank test, a linear impactor setup was used to evaluate the airbag response under mechanical loading. The setup consists of an inflator, an airbag cushion, a rigid wall, and a linearly moving impactor, as shown in Figure 3.2. During the simulation, the inflator deploys the airbag while the impactor compresses the cushion against the rigid wall. This configuration introduces airbag fabric deformation, venting, and contact interaction, while remaining more controlled than the complete airbag–occupant interaction model.

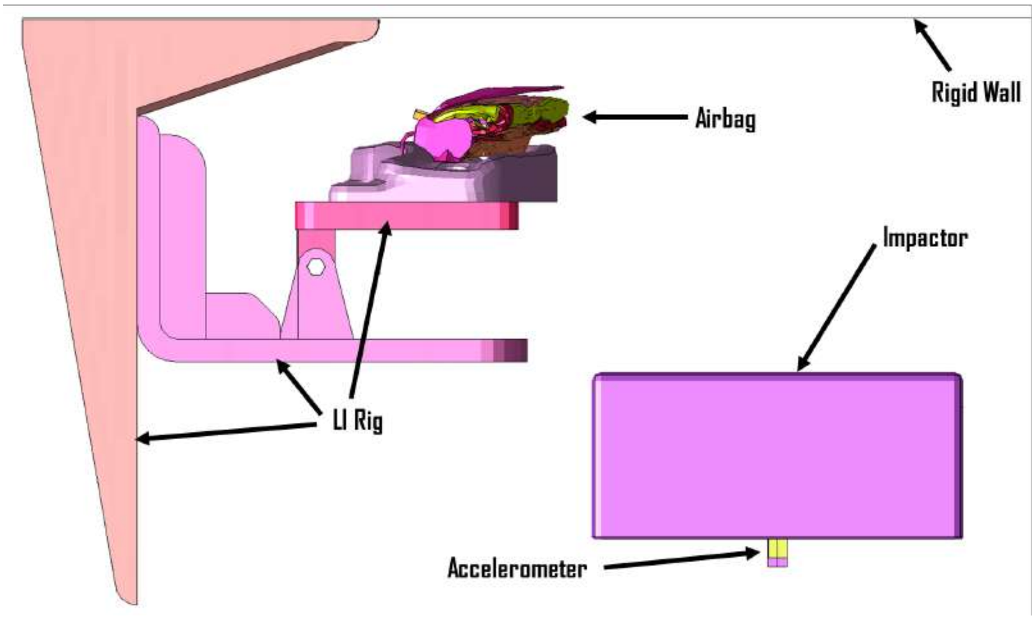

Figure 3.2: CAE setup of the linear impactor test, showing the main components and loading direction.

The compressed airbag state from the CPM simulation is shown in Figure 3.3. This illustrates the mechanical loading condition introduced by the impactor during the linear impactor test.

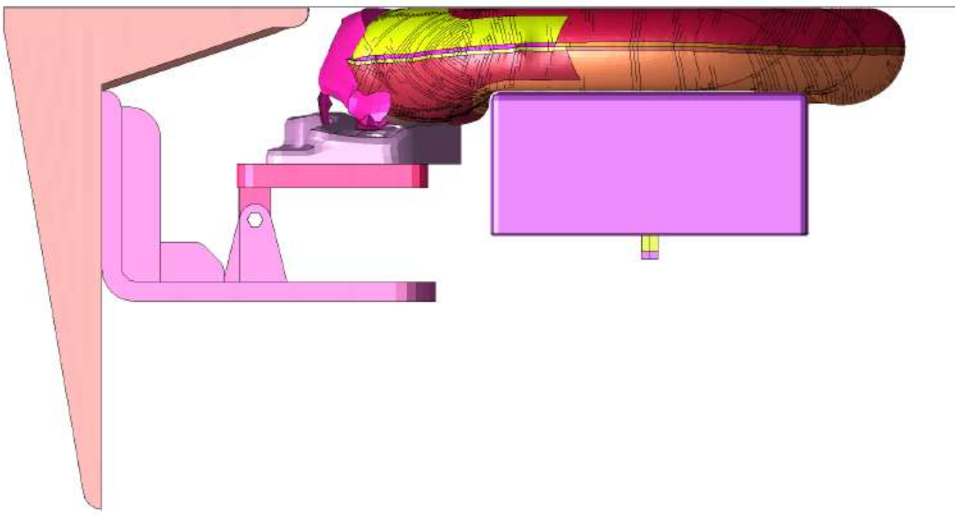

Figure 3.3: Compressed airbag state in the CPG linear impactor simulation.

The main parameters defining the linear impactor setup are summarized in Table 3.1. These include the venting size, impactor mass, impactor velocity, trigger distance, and friction coefficient between the SAB and the impactor.

Table 3.1: Linear impactor setup parameters.

Vent hole diameter [mm]	Mass [kg]	Velocity [m/s]	Trigger distance [mm]	Friction coefficient (SAB–impactor)
24	35	6	190.5	$f_s = 0.3$ $f_d = 0.05$

Note: f_s = static friction coefficient; f_d = dynamic friction coefficient.

The CPM model was provided by VCC and had previously been correlated against an internally conducted linear impactor test. Since no additional physical linear impactor data were available within this project, the correlated CPM model was used as the reference configuration. The CPG model was therefore evaluated relative to the CPM response under the same linear impactor setup and boundary conditions.

The evaluation was based on airbag pressure, impactor displacement, impactor velocity, impactor acceleration, force–displacement response, and energy–displacement response. The comparison focused primarily on curve shape, timing, and overall response trend, while peak values were used as supporting indicators. If notable deviations were observed between CPG and the CPM reference, relevant CPG modelling parameters, contact definitions, or airbag setup parameters were adjusted before applying the method to the rigid-seat dummy interaction simulations.

The initial CPG model was implemented using the same input definitions as the CPM reference model. This included the same inflator input, two vent definitions with identical venting size, and the same module leakage part, denoted as *inflator_out*. However, the CPM airbag card included a scaling factor parameter for the module leakage, whereas the corresponding CPG keycard did not include this scaling parameter yet. As a result, the initial configuration did not provide fully equivalent leakage conditions between the two gas methods, even though the same leakage part was used.

During the CPG tuning procedure, the module leakage definition was therefore modified to obtain more comparable leakage conditions. The original module leakage part, *inflator_out* (green), was replaced by a smaller part, denoted as *inflator_wall* (gold). The original and adjusted module leakage definitions are shown in Figure 3.4. The adjusted CPG configuration was then used for the continued evaluation against the correlated CPM reference and was carried forward to the rigid-seat dummy interaction simulations.

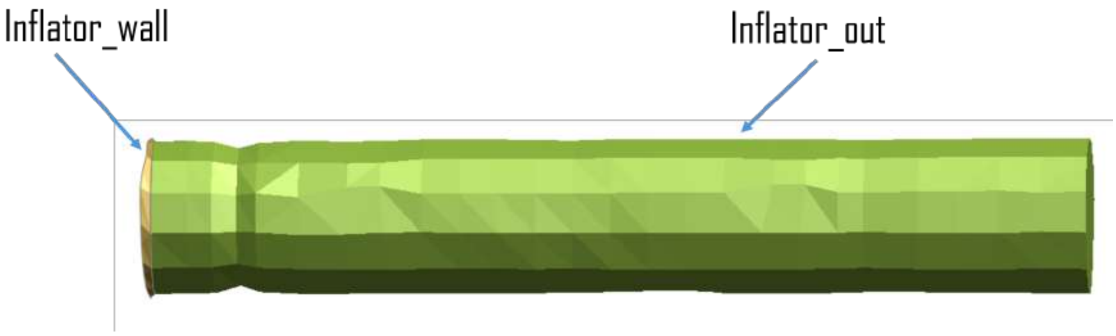

Figure 3.4: Comparison of the original module leakage part, *inflator_out*, and the adjusted module leakage part, *inflator_wall*, used in the CPG linear impactor model.

3.3 Airbag–Occupant Interaction

Following the tank test and the linear impactor test, the airbag model was evaluated in a more representative airbag–occupant interaction setup. This step was introduced to assess how the CPM and CPG airbag models behaved when applied to a configuration including more interacting components than the linear impactor test. The setup consisted of a simplified rigid-seat, a plexiglass wall, a SAB, and an ATD occupant model. Two testcases also featured a steering-wheel.

This setup introduced a more complex interaction between the airbag fabric, the occupant model, the seat environment, and the surrounding structure. Physical tests were conducted to provide a reference for the CAE models, enabling an assessment of whether the two airbag modelling approaches could reproduce the main response trends observed experimentally.

The evaluation focused on the airbag unfolding behaviour, airbag pressure response, arm trajectory, and overall dummy response. These quantities were selected because they describe both the behaviour of the airbag during deployment and its interaction with the occupant model.

A test matrix was defined by varying the occupant model, arm configuration, arm position, and distance between the seat and the plexiglass. The investigated configurations are summarized in Table 3.2. In total, eight test configurations were considered, where each configuration was physically tested twice, resulting in a total of 16 physical tests. The y-displacement denotes the lateral distance between the seat and the plexiglass structure.

Table 3.2: Test matrix with physical test coverage.

#	ATD category	Arm configuration	Arm position	y-displacement [mm]
1	50th percentile male	Half-arm	–	80
2	50th percentile male	Half-arm	–	120
3	5th percentile female or 13-year-old child	Half-arm	–	80
4	5th percentile female or 13-year-old child	Half-arm	–	120
5	5th percentile female or 13-year-old child	Full arm	Driver	80
6	5th percentile female or 13-year-old child	Full arm	Driver	120
7	5th percentile female or 13-year-old child	Full arm	Passenger	80
8	5th percentile female or 13-year-old child	Full arm	Passenger	120

During the setup definition, several initial distances between the seat and the plexiglass were considered. The distances of 80 mm and 120 mm were selected for further investigation because they provided a suitable balance between arm interaction, loading response on occupant model, and available clearance on the test rig. These distances were therefore used in the physical tests and in the corresponding CAE simulations.

3.3.1 Physical test setup

The physical tests were conducted using an existing test rig at VCC. The rig was lightly adapted for the present study in order to provide a controlled and repeatable environment for evaluating the interaction between the SAB and the occupant. The objective was not to reproduce a complete vehicle interior, but to isolate the main interaction between the deployed airbag and the ATD. Consequently, vehicle interior components such as trim panels, dashboard geometry, seat cushioning, and other surrounding structures were excluded from the setup.

The test configuration was planned together with the VCC test team. The existing rig was modified by reinforcing the plexiglass frame structure with additional bracing and by adding a steering wheel assembly to enable driver-position arm configurations. The final physical setup consisted of a rigid seat structure, a plexiglass wall, the ATD, the SAB, and a steering wheel for the driver-position cases. The main parts of the physical test setup are visualized in Figure 3.5.

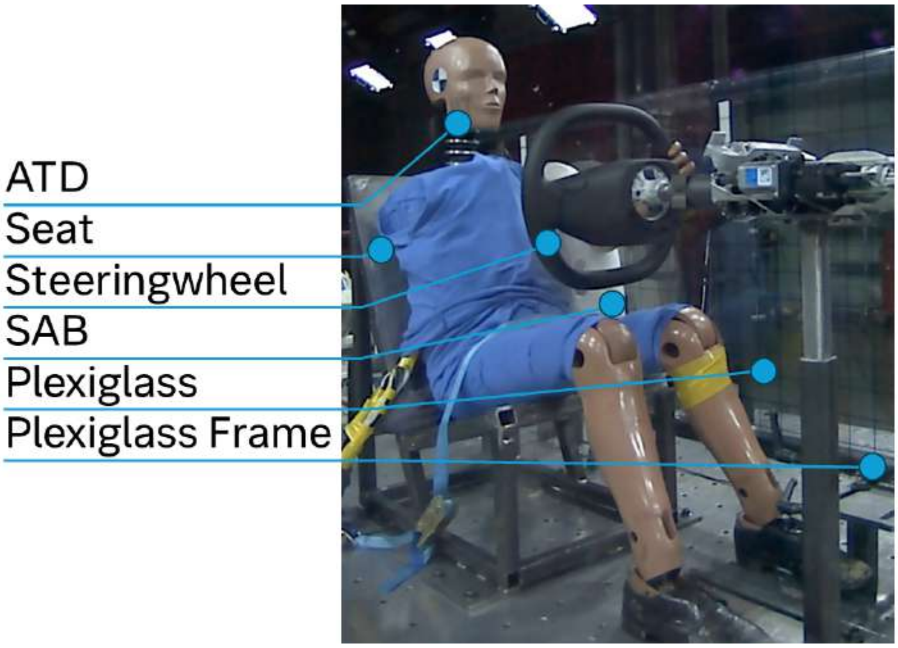

Figure 3.5: Simplified parts list for the physical tests.

The main components of the physical test setup are summarized in Table 3.3. These components define the boundary conditions of the simplified test environment and were selected to support repeatable positioning of the ATD, SAB, plexiglass boundary, and steering wheel assembly.

Table 3.3: Overview of the main components in the physical test setup.

Component	Material	Position	Function
Rigid seat pan	Stainless steel	Lower part of the seat structure	Provides a rigid seating surface for the ATD.
Rigid seatback	Stainless steel	Rear part of the seat structure	Supports the ATD torso.
Plexiglass wall	Plexiglass	Lateral side of the seat and airbag	Represents the lateral boundary surface.
Wall frame	Stainless steel	Around the plexiglass wall	Supports and positions the plexiglass wall.
Slotted mountings	Stainless steel	Between the frame and plexiglass mounting points	Enables adjustment of the seat-to-plexiglass distance.
Countersunk screws	Steel	Between plexiglass and frame	Clamp plexiglass to frame
Additional bracing	Stainless steel	Around the plexiglass frame	Reduces unwanted deformation of the plexiglass support structure.
Steering rack mount	Steel	In front of the ATD	Supports the steering wheel assembly.
Steering wheel	Vehicle component	In front of the ATD upper body	Enables driver-position arm configurations.

Relevant distances and positioning references were measured in the CAE environment and then provided to the VCC test team as setup instructions for the physical tests. Examples of the dimensional references used during this process are shown in Figure 3.6. During test preparation, these measurements were used to position the ATD, plexiglass wall and steering wheel consistently between each physical test.

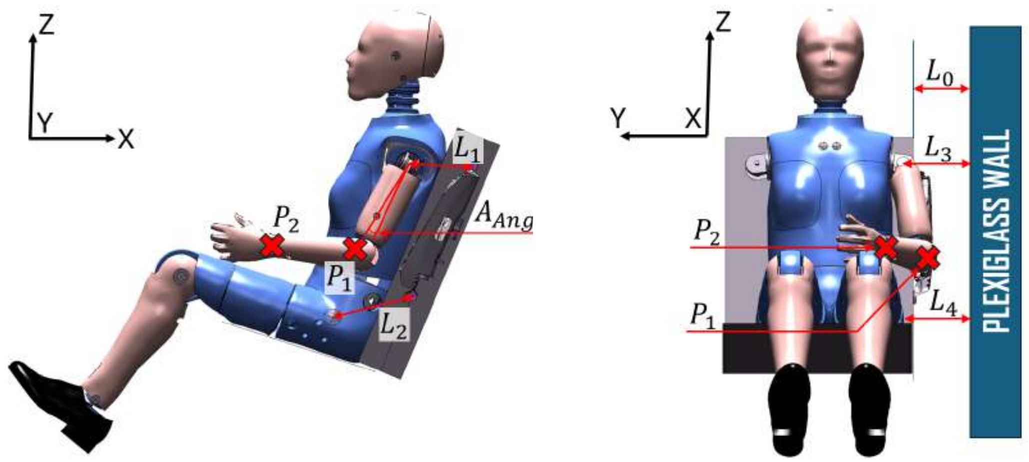

(a) Example of measurements in X–Z view.

(b) Example of measurements in Y–Z view.

Figure 3.6: Examples of measurement references provided to the VCC test team.

Table 3.4 provides an example of the dimensional setup information supplied to the

VCC test team. The values correspond to testcase 8 described in Table 3.5 . The elbow and hand joint coordinates, denoted P_1 and P_2, are expressed relative to the H-point. In this context, the H-point was used as the reference measurement point between the ATD hip joints, and the reported coordinates were adjusted accordingly.

Table 3.4: Example of dimensional setup references for the full-arm SID-IIs 120 mm relaxed-position test case.

Annotation	Measured plane	Description	Value
L_0	X	Plexiglass distance to seat	120 mm
L_1	X–Z	Left shoulder joint to upper SAB rig mount distance	$(X, Z) = (146.6, 3.4)$ mm
L_2	X–Z	Left hip joint to lower SAB rig mount distance	$(X, Z) = (173.6, 48.3)$ mm
L_3	Y	Left shoulder joint to plexiglass distance	90.2 mm
L_4	Y	Left hip joint to plexiglass distance	128.6 mm
A_{ANG}	X–Z	Arm angle relative to torso	35°
P_1	X–Y–Z	Elbow joint coordinate relative to H-point	$(X, Y, Z) = (17.6, -170.0, 170.0)$ mm
P_2	X–Y–Z	Hand joint coordinate relative to H-point	$(X, Y, Z) = (-183.4, -78.0, 142.0)$ mm

3.3.1.1 ATD Setup

For the physical testing the ATD setup is provided in Table 3.5. Note that the safety team at VCC was able to provide a custom SID-IIs setup with a full arm attatchment mounted on the left arm.

Table 3.5: ATD setup for physical tests.

#	ATD model	Arm configuration	Posture	y-displacement [mm]
1	WorldSID-50	Half arm	–	80
2	WorldSID-50	Half arm	–	120
3	SID-IIs	Half arm	–	80
4	SID-IIs	Half arm	–	120
5	Custom SID-IIs	Left full arm, right no arm	Driver	80
6	Custom SID-IIs	Left full arm, right no arm	Driver	120
7	Custom SID-IIs	Left full arm, right no arm	Passenger	80
8	Custom SID-IIs	Left full arm, right no arm	Passenger	120

3.3.1.2 Pressure Measurement

The physical test evaluation included custom-fitted airbag pressure probes, which were used to capture the temporal pressure response inside the SAB during deployment. The probes were installed with the intention of minimising their influence on the airbag deployment behaviour. For this reason, the airbag was not opened during installation. The external placement of the pressure probe on a deployed airbag is shown in Figure 3.7a. The corresponding internal placement is shown in Figure 3.7b, where the probe tip was positioned below the nozzle to reduce the influence of ignition pressure vibration effects on the measurement.

(a) External placement of the SAB pressure probe, coloured in blue.

(b) Internal placement of the SAB pressure probe.

Figure 3.7: Pressure probe placement for the SAB, shown from the external and internal view.

3.3.2 Virtual Test Setup

The CAE environment was configured to represent the physical test setup as closely as possible, while selected simplifications were introduced to balance computational cost and model complexity. The simplified assembly names used throughout this work are shown in Figure 3.8. It should be noted that each assembly consists of several individual parts, often with different materials, boundary conditions, and assigned attributes. A detailed description of every individual component is therefore considered unnecessary for the scope of this report. Instead, this subsection provides an overview of the main assemblies included in the CAE model.

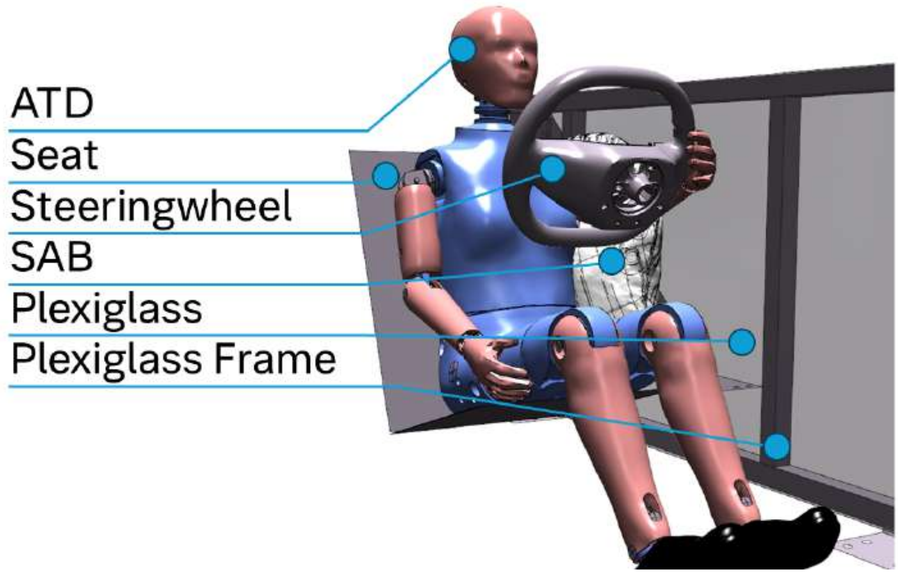

Figure 3.8: Simplified assembly list for the CAE model.

Table 3.6 summarises the main assemblies included in the CAE model, together with representative example parts and a brief description of their use in the CAE context.

Table 3.6: Model components and example parts included in each assembly.

Assembly	Example parts	Description
ATD	Left hand, right hand, left foot, pelvis accelerometer, etc.	Humanetics dummy model consisting of several elements and components.
Seat	Seat bottom, seat back, ghost seat bottom, ghost seat back, etc.	Rigid seat assembly consisting of several components used to represent the seat configuration and seat-squash technique.
Steering wheel	Rim, bezel, foam, etc.	Steering wheel model provided by VCC for hand interaction, including a rigidified hub. This assembly is included only in full-arm driver-position test cases.
SAB	Inflator, bracket, fabric, etc.	SAB assembly provided by VCC and mounted to the seat model using boundary constraints.
Plexiglass rig	Plexiglass, frame, leg post, etc.	Rig assembly consisting of the plexiglass panel and supporting frame structure used for mounting and test representation.

3.3.2.1 ATD Setup

For the virtual simulations the ATD setup is provided in Table 3.7. Considering the time and resource constraints on this project VCC weren't able to provide a virtual SID-IIs ATD with a full-arm configuration. Therefore a compromise was made and the Hybrid III ATD emerged as the closest match as it represents a 5th percentile female. This ATD already has 2 full arms in standard configuration. Further comparison between the ATDs can be reviewed in Section 2.4.

Table 3.7: ATD setup for virtual tests.

#	ATD model	Arm configuration	Posture	y-displacement [mm]
1	WorldSID-50m	Half arm	–	80
2	WorldSID-50m	Half arm	–	120
3	SID-IIs 05 f	Half arm	–	80
4	SID-IIs 05 f	Half arm	–	120
5	Hybrid III 05 f	Full arm	Driver	80
6	Hybrid III 05 f	Full arm	Driver	120
7	Hybrid III 05 f	Full arm	Passenger	80
8	Hybrid III 05 f	Full arm	Passenger	120

3.3.2.2 Meshing Strategy

The meshing criteria applied in this study are provided by VCC and are based on the company's internally developed meshing standards. In terms of model fidelity, the FE discretization is classified as a medium-sized mesh according to VCC guidelines. A nominal target element size of 5 mm is adopted for the majority of the model.
The overall model is predominantly discretized using shell elements to represent the structural components. In addition, selected interior regions of the dummy model are represented using beam elements and other discrete element formulations, provided by Humanetics to appropriately capture the mechanical behaviour of internal components.

3.3.2.3 Material Models

The material models used in the CAE model were mainly provided by VCC and are representative of production-oriented vehicle CAE modelling. Material cards from VCC and Humanetics are confidential and are therefore not presented in detail. In Table 3.8 there is a summary of the main material model sources and representations used for the different assemblies in the CAE model.

Table 3.8: Overview of project-defined material representations used in the CAE model.

Assembly	Material	Density [kg/mm^3]	Young's modulus [GPa]	Poisson's ratio [-]	Plasticity definition
Plexiglass	PMMA plexiglass	1.18×10^{-6}	3.0	0.35	Yield stress of 0.065 GPa.
Steel frame	DX54 mild steel	7.8×10^{-6}	205.0	0.3	Plastic response defined through the referenced load curve in the material card.

3.3.2.4 Boundary Conditions and Constraints

The boundary conditions and constraints in the CAE model consist primarily of the `*BOUNDARY_SPC` keyword to replicate the plexiglass fram anchoring to the ground, and the `*CONSTRAINED_NODAL_RIGID_BODY` keyword to replicate the screw connections between different components. In the developed model, these definitions are used to represent selected physical constraints and simplified fastening connections in the test rig.

Figure 3.9a shows the boundary-constrained nodes, marked with red dots. These constraints are used at selected locations where translational and rotational degrees of freedom are restricted. In the plexiglass rig, constrained nodes are defined around each mounting hole of the leg posts. In addition, the steering wheel has one constrained master node located at the centre of the hub.

Figure 3.9b shows the nodal rigid body definitions, marked with blue dots. These definitions are used at locations where groups of nodes are connected through the `*CONSTRAINED_NODAL_RIGID_BODY` keyword. In the present model, they are applied to fasten the plexiglass to the plexiglass frame, with the placement distributed throughout the frame to represent the original countersunk screws. They are also applied at the plexiglass legs, where they connect to the upper part of the rear frame, and at the three mounting holes of the SAB bracket, where they fasten the SAB to the seat.

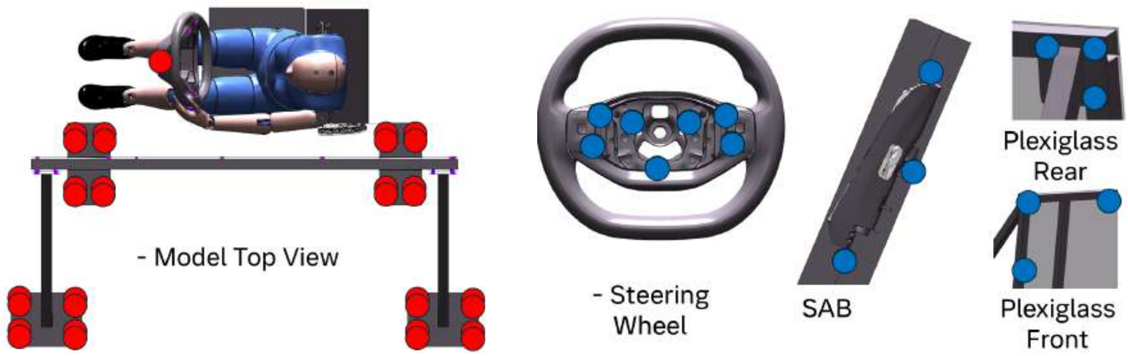

(a) Boundary-constrained nodes marked with red dots.

(b) Constrained Nodal rigid bodies marked with blue dots.

Figure 3.9: Overview of the main boundary-constrained nodes and nodal rigid bodies used in the CAE model.

Together, these constraint definitions provide a simplified representation of the physical test rig.

3.3.2.5 Seat Geometry Adaptation for ATD Positioning

The seat-squashing procedure used in this thesis was implemented as a simplified rigid-body pre-loading step in LS-DYNA. A duplicated seat geometry, referred to here as a "moving rigid ghost", was defined using `*MAT_RIGID`. Its motion was prescribed with `*DEFINE_TRANSFORMATION` and parameterised displacement expressions, allowing the rigid ghost to move towards the seat reference position during the first 4 ms of the simulation. The purpose of the moving rigid ghost was to establish initial contact with the dummy pelvis and back regions, as shown in Figure 3.10, a more detailed technical explanation is presented in Section 2.4.5. The reference seat itself was not contacted by the rigid ghost; instead, the ghost was used only as a displacement-controlled loading body to position the dummy relative to the seat reference. This generated a pre-loaded dummy–seat configuration before the main side-airbag deployment simulation.

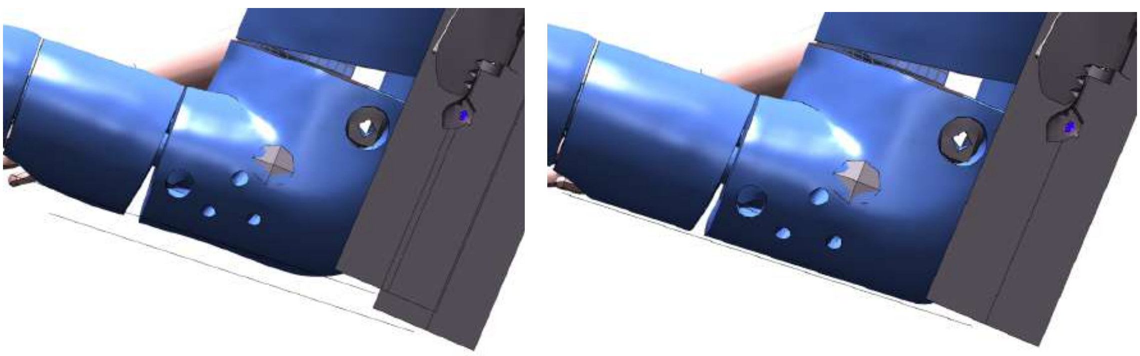

(a) Initial configuration at 0 ms.

(b) Pre-loaded configuration at 4 ms.

Figure 3.10: Seat-squashing procedure for the WSID50 configuration, showing the initial state and the pre-loaded dummy position relative to the seat reference.

The effect of the seat-squashing procedure is visible at 4 ms, where the lower dummy region has developed a locally flattened contact area against the seat reference.

3.3.3 ATD Instrumentation

The SID-IIs and WSID50 ATDs use different test-channel configurations. Therefore, this project selected instrumentation channels that were available in both ATD configurations, allowing the physical tests and CAE results to be compared using a consistent set of response quantities and plotting layouts.

For the SID-IIs and WSID50 configurations, the comparison was based on thoracic and pelvic accelerations, rib deflections, shoulder and rib deflection. The corresponding measurement locations are shown in Figure 3.11, and the channels used in the post-processing are summarised in Table 3.9.

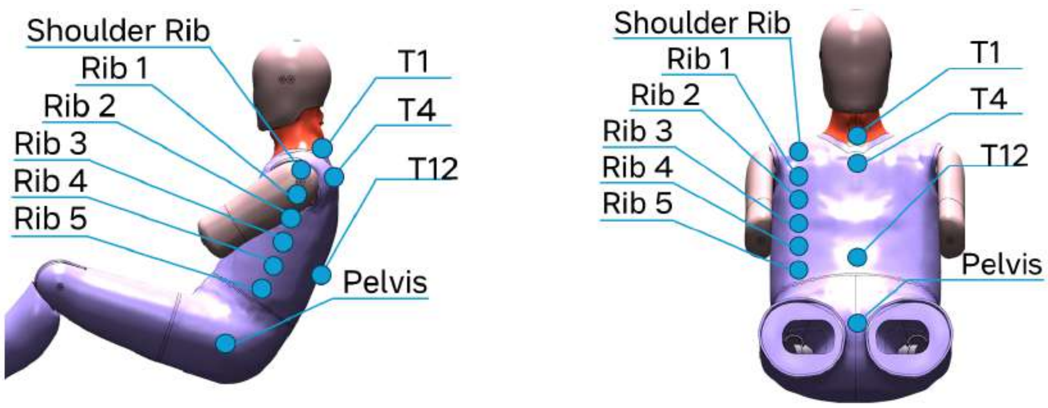

(a) X–Z plane. **(b)** Y–Z plane.

Figure 3.11: Measurement locations used for the SID-IIs and WSID50 configurations, shown in the X–Z and Y–Z planes on the WSID50 dummy.

Table 3.9: Instrumentation channels used for half-arm physical test and CAE comparison.

Instrumentation	Measurement
T1 upper thorax accelerometer	Acceleration in x-, y-, and z-directions
T4 middle thorax accelerometer	Acceleration in x-, y-, and z-directions
T12 lower thorax accelerometer	Acceleration in x-, y-, and z-directions
Pelvis accelerometer	Acceleration in x-, y-, and z-directions
Rib 1–5	Rib deflection
Shoulder rib	Shoulder rib response
Shoulder load cell	Shoulder force response
Pelvis load cell	Pelvis force response
Pubic symphysis load cell	Pelvis force response
Lumbar spine load cell	Lumbar spine force and moment response
Neck load cell	Neck force and moment response

For the full-arm ATD configurations, a separate channel selection was used due to differences in instrumentation of the SID-IIs and Hybrid III. The evaluated responses consisted of upper-arm and forearm moments, pelvis accelerations and pelvis acceleration magnitude. The relevant measurement locations are shown in Figure 3.12, and the corresponding channels are summarised in Table 3.10.

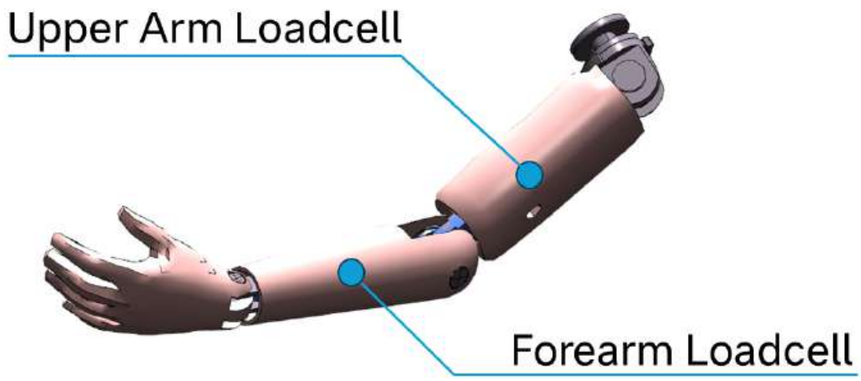

Figure 3.12: Measurement locations used for the full-arm dummy configurations.

Table 3.10: Instrumentation channels used for the full-arm test cases.

Instrumentation	Measurement
Upper arm load cell	Moment in X and Y direction
Forearm load cell	Moment in X and Y direction
Pelvis accelerometer	Acceleration in X, Y and Z direction
Pelvis acceleration magnitude	Resultant acceleration magnitude calculated from X, Y and Z acceleration components

3.3.4 Assumptions and Simplifications

Several simplifications were introduced in the LS-DYNA model to maintain computational feasibility and robust simulation execution. These simplifications define the level of physical detail included in the CAE model and should therefore be considered when interpreting the results.

- **Airbag representation:** The airbag geometry, folding representation, pressure evolution, and internal characteristics were treated as predefined model inputs rather than independently validated physical parameters.
- **Material representation:** Several components were described using simplified constitutive material models. Component-specific calibration, advanced strain-rate effects, thermal effects, and anisotropic behaviour were therefore not included for all materials.
- **Damage and failure:** Failure behaviour, where included, was represented using simplified threshold-based criteria. Progressive damage evolution and detailed crack propagation were not explicitly resolved.
- **Contact and friction:** Contact interactions were modelled using penalty-based contact definitions with prescribed parameters. Friction coefficients were with the exception of a few highly friction dependent airbag cases treated as constant, while effects such as adhesion, wear, surface roughness, pressure dependence, and temperature dependence were neglected.
- **Rigid components:** Selected components of the test environment were modelled as rigid bodies. These components were therefore assumed not to deform or absorb energy through structural compliance.
- **Mesh and geometry:** The model geometry was discretised using a FE mesh, where small geometric details were simplified or omitted. Local stress concentrations and highly detailed geometric effects may therefore not be fully resolved.
- **Numerical controls:** Explicit time integration, timestep control, hourglass control, and numerical damping were used to maintain stable simulations. These numerical settings improve robustness but may introduce non-physical contributions to the response. These parameters were defined by VCC.
- **Neglected physical effects:** Thermal effects, heat transfer, material ageing, and environmental influences were outside the scope of the model.

Overall, the model should be interpreted as a representative CAE approximation of the physical test setup rather than a complete representation of all physical phenomena. The simplifications were considered acceptable for the comparative evaluation performed in this thesis.

3.4 Evaluation Strategy

To enable a meaningful comparison between the two CAE methods, the reliability of the investigated test cases were assessed. Several factors may influence the fairness and robustness of the comparison, including the variation between repeated physical tests and the extent to which the CAE simulations represent the corresponding physical test conditions.

The reliability assessment is based on two metrics: physical repeatability and CAE comparability to Physical Tests. Physical repeatability evaluates the consistency between the two repeated physical tests for each test case. CAE comparability to Physical Tests evaluates whether the CAE simulations are sufficiently representative of the corresponding physical test conditions, including aspects such as initial positioning, test setup, ATD configuration and physically plausible simulation behaviour.

Since the objective of this study is to compare the CPM and CPG methods in relation to physical test behavior, CAE comparability was assigned a higher weight than physical repeatability. Physical repeatability was assigned a lower weight because only two physical tests were conducted for each test case, making the repeatability assessment less robust as a physical reference.

The weight division was based on a engineering judgement. The final reliability score was therefore calculated using a weighted assessment, where physical repeatability accounts for 25% and CAE comparability accounts for 75% of the final score, see Equation (3.1).

$$R = 0.25R_{\text{phys}} + 0.75R_{\text{CAE}} \tag{3.1}$$

where R is the final reliability score, R_{phys} is the physical repeatability score, and R_{CAE} is the CAE comparability score. Both metrics are evaluated on a scale from 1 to 5, where the scale definitions are presented in Table 3.11.

Table 3.11: Assessment scale used for physical repeatability and CAE comparability.

Score	Reliability	Physical repeatability	CAE comparability to Physical Test
1	Very low	The physical tests show clear differences in ATD positioning or overall response behavior.	The simulations show major deviations from the physical tests, with limited similarity in the relevant response characteristics.
2	Low	The physical tests show some similarities, but deviate in important response parameters.	The simulations show major differences compared to the physical tests, although some similarities are still present.
3	Moderate	The physical tests show similar general kinematics, but noticeable differences are observed in some important response parameters.	The simulations have comparable initial conditions, but deviate from the physical tests after trigger time.
4	High	The physical tests show good agreement in the important response parameters. Minor differences are observed, but these do not significantly affect the overall interpretation.	The simulations have nearly identical conditions compared to the physical tests, with only minor differences affecting the comparison.
5	Very high	The physical tests are almost identical in the evaluated response.	The simulations and physical tests are almost identical in the evaluated response.

All test cases were included in the subsequent qualitative and quantitative assessment. However, the reliability score was used as contextual information when interpreting the results, since test cases with lower reliability provide a less robust basis for drawing conclusions regarding the relative performance of CPM and CPG.

3.4.1 Qualitative and Quantitative Assessment

A combined qualitative and quantitative assessment procedure was applied to evaluate the correlation between the CAE simulations and the corresponding physical tests. The purpose of this assessment was to provide a structured basis for comparing the behaviour predicted by the two airbag gas modelling methods, CPM and CPG, against the physical test responses.

The qualitative assessment was based on visual evaluation of snapshots generated at selected timesteps and from predefined viewing directions. The main views used in the assessment were the front view, Left-Hand Side (LHS) view and the detailed LHS view. In the front view, the evaluation focused primarily on the arm trajectory and the overall motion of the ATD during the airbag–occupant interaction, while the LHS view provided further perspective outside of the plexiglass. In the detailed LHS view, emphasis was placed on the early deployment phase of the SAB, including the airbag geometrical shape, creasing behaviour and the general unfolding sequence. The qualitative comparison was performed by visually comparing the CAE simulations with the physical test recordings in order to assess whether the main deployment and interaction phenomena were represented in a physically plausible manner.

The numerical comparison between the physical tests and the CAE simulations was based on post-processed peak response quantities collected from the result curves. For each investigated response signal, the peak event was identified from the maximum absolute amplitude within the evaluated time window. The signed response value at this peak was then retained for Test 1, Test 2, CPM, and CPG. This allowed the individual signal tables to show whether the CAE response had the same polarity as the corresponding physical test response. The extracted quantities included accelerations, rib deflections, arm moments, pelvis response quantities, and side airbag pressure. The pressure response was retained as a reference quantity in the summary tables but was excluded from the grouped mean-difference calculations.

For each response signal, the two physical tests were first combined into a single physical reference value. This was done by calculating the arithmetic mean of the signed peak values from Test 1 and Test 2 for each response signal, as shown in Equation 3.2.

$$\bar{x}_{\text{test},i} = \frac{x_{\text{Test 1},i} + x_{\text{Test 2},i}}{2} \tag{3.2}$$

where $x_{\text{Test 1},i}$ and $x_{\text{Test 2},i}$ are the signed peak response values for response signal i. After the physical reference value had been defined, the deviation between each CAE method and the physical-test mean was calculated. This signed difference was calculated separately for CPM and CPG according to Equation 3.3.

$$\Delta_{m,i} = x_{m,i} - \bar{x}_{\text{test},i} \tag{3.3}$$

where m denotes the gas method, either CPM or CPG. The signed difference indicates whether the simulation response was higher or lower than the physical-test reference for the extracted signed peak value. Since the signed peak value was retained, the sign of the individual response values can also be used to assess whether the CAE response had the same polarity as the physical tests.

To compare CPM and CPG at a grouped response level, the magnitude of the deviation was used. This prevented positive and negative deviations from cancelling each other when several response signals were combined. The absolute difference used for this comparison is given in Equation 3.4.

$$|\Delta_{m,i}| = |x_{m,i} - \bar{x}_{\text{test},i}| \tag{3.4}$$

The grouped values were therefore calculated as mean absolute differences in the original physical units of each response family.

For the half-arm dummy cases, the response quantities were grouped into thoracic, rib, and pelvic response families. The thoracic response family consisted of the T1, T4, and T12 accelerations in the x- and y-directions. The rib response family consisted of shoulder rib deflection and Rib 1–Rib 5 deflections. The pelvic response family consisted of pelvis accelerations in the x-, y-, and z-directions. These grouped responses were evaluated for the WSID-50M and SID-IIs cases at both 80 mm and 120 mm positions.

For the full-arm dummy cases, the response quantities were grouped into arm moment and pelvic response families. The arm moment family consisted of the upper arm and forearm moments in the x- and y-directions. The pelvic response family consisted of pelvis accelerations in the x-, y-, and z-directions, together with the pelvis acceleration magnitude. These grouped responses were evaluated for the driver and relaxed arm positions at both 80 mm and 120 mm.

For each response family, the grouped case-level difference was calculated by averaging the absolute differences of the response signals included in that family. This calculation is shown in Equation 3.5.

$$E_{m,F} = \frac{1}{n_F} \sum_{i \in F} |\Delta_{m,i}| \tag{3.5}$$

where F denotes the response family and n_F is the number of response signals included in that family. The total value reported for each response family was then calculated by averaging the grouped case-level differences across the relevant test cases. This overall family-level mean difference is given in Equation 3.6.

$$\bar{E}_{m,F} = \frac{1}{n_c} \sum_{c=1}^{n_c} E_{m,F,c} \tag{3.6}$$

where n_c is the number of cases included in the group. The gas method with the lower overall mean absolute difference was considered closer to the physical tests for that response family.

Finally, the relative difference between the two gas methods was calculated to express how much lower the mean absolute difference was for the closer method. This relative reduction was calculated according to Equation 3.7.

$$I_F = 1 - \frac{\min\left(\bar{E}_{\mathrm{CPM},F}, \bar{E}_{\mathrm{CPG},F}\right)}{\max\left(\bar{E}_{\mathrm{CPM},F}, \bar{E}_{\mathrm{CPG},F}\right)} \tag{3.7}$$

The resulting percentage was only used to express the relative reduction in mean absolute difference between CPM and CPG within the same response family. It was not used as a general injury score or as a weighted performance index across different physical units.

3.4.2 Computational Time

Computational time was included as an evaluation metric in the comparison between the CPM and CPG gas methods. The evaluation was performed at two levels. First, a stand-alone airbag-only setup was used to isolate the computational cost associated with the airbag gas formulation. Second, the same timing quantities were extracted from the simplified rig simulations to evaluate how the computational cost translated to complete airbag–occupant interaction test cases.

The stand-alone comparison was performed using a simplified simulation setup consisting only of the SAB and its corresponding bracket. The airbag–bracket assembly was fixed in free space, as shown in Figure 3.13. This setup was selected to reduce the influence of occupant contact, seat interaction, and other structural components, thereby allowing the computational performance of the two gas methods to be assessed more directly.

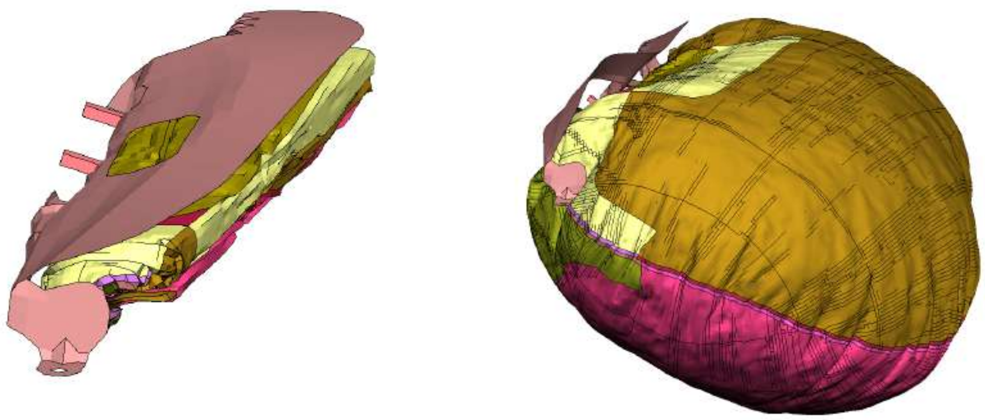

(a) Folded configuration. **(b)** Unfolded configuration.

Figure 3.13: Simplified airbag–bracket setup used for the computational-time comparison between CPM and CPG.

Both CPM and CPG simulations were performed using the same airbag input definitions as those applied in the airbag–occupant interaction simulations. This ensured that the stand-alone comparison was based on equivalent inflator characteristics, airbag definition, and model settings.

The computational performance was evaluated from the solver output files after completion of each simulation. Total wall-clock time was used as the primary runtime measure. In addition, the clock time per zone cycle was extracted as a solver-reported normalized timing measure, describing the elapsed clock time relative to the number of calculated zone cycles. This value was used to compare the computational cost of advancing the CPM and CPG simulations within the same model setup. The relative gas Central Processing Unit (CPU) share was also extracted from the solver timing output to identify how much of the CPU usage was associated with the gas-method contribution.

The stand-alone airbag-only simulations were run using 192 Massively Parallel Processing (MPP) cores, while the simplified rig simulations were run using 128 MPP cores. The computational-time factors were therefore interpreted within each comparison level, where CPM and CPG were evaluated using the same setup and core count. Direct comparison of absolute runtime between the stand-alone and simplified rig levels was not used as the main basis for interpretation, since the model size and core allocation differed between the two evaluation levels.

4

Results

This chapter presents the results from the evaluation of the CPM and CPG airbag gas modelling methods. The results are structured according to the main phases of the study. First, the CPG tuning process is evaluated using the inflator tank test and the linear impactor setup. The airbag–occupant interaction results are then presented, including test-case reliability, side-airbag pressure response, airbag unfolding behaviour, arm trajectory, and occupant-related injury metrics. The chapter concludes with a computational-time comparison, where the two gas methods are assessed using both a standalone airbag-only setup and the applied simplified rig simulations.

4.1 CPG Model Tuning and Response Evaluation

The following section describes the tuning procedure used to adapt the CPG model for the simplified rig test setup. The evaluation is based on the tank test pressure response and the impactor response obtained from the linear impactor test. The purpose is to present the main characteristic differences between CPM and CPG that are relevant for the subsequent simplified rig simulations.

4.1.1 Tank Test

The purpose of the tank test was to evaluate whether the CAE inflator models were able to reproduce the pressure response observed in the physical test. The pressure histories obtained from the physical test, CPM, and CPG are presented in Figure 4.1.

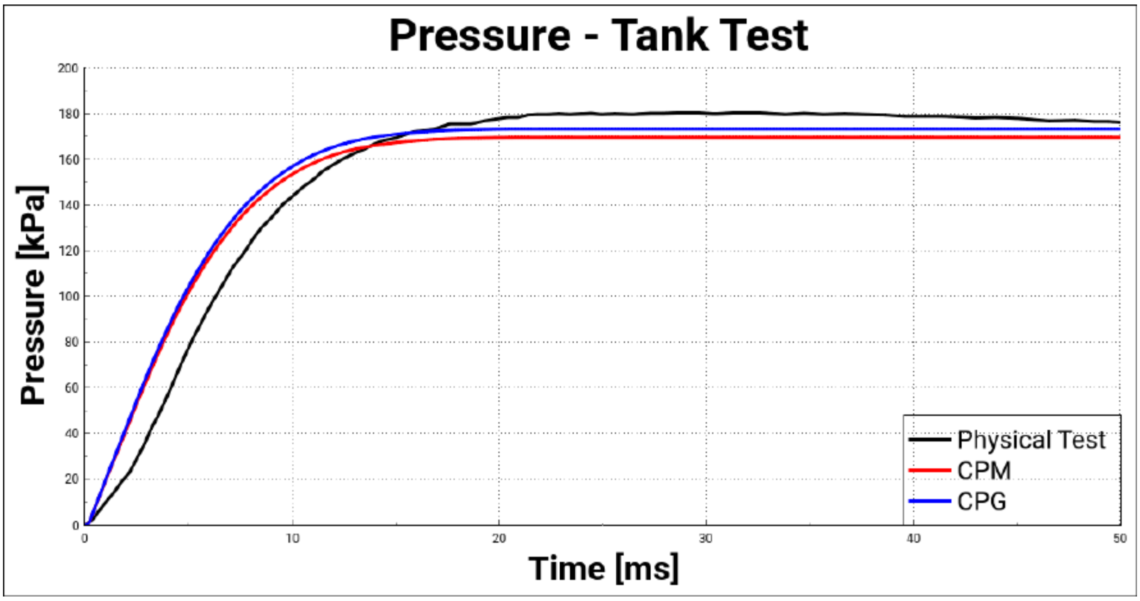

Figure 4.1: Tank test pressure response for the physical test, CPM, and CPG.

Several aspects can be evaluated from Figure 4.1, including the pressure build-up, the converged pressure level, and the overall shape of the pressure curve. A summary of the main observations is provided in Table 4.1.

Table 4.1: Summary of the main observations from the tank test pressure response.

Evaluation aspect	Physical test	CPM	CPG
Pressure build-up	Gradual pressure increase during the initial phase.	Faster pressure increase than the physical test.	Faster pressure increase than the physical test.
Converged pressure level	Stabilizes at approximately 180 kPa.	Stabilizes at approximately 170 kPa.	Stabilizes at approximately 175 kPa.
Overall curve shape	Similar general trend, with a slower initial rise.	Similar overall pressure development, but with a lower final pressure level.	Similar overall pressure development, with a final pressure level closer to the physical test.
Agreement with physical test	Reference response.	Captures the general pressure trend, but underestimates the converged pressure level.	Captures the general pressure trend and shows closer agreement in converged pressure level.

Both CPM and CPG show a faster initial pressure increase compared with the physical test, whereas the physical test exhibits a more gradual pressure rise. The physical test stabilizes at approximately 180 kPa, while CPM and CPG converge at approximately 170 kPa and 175 kPa, respectively. Despite these differences, the overall pressure development is similar for all three curves, indicating that both CAE models capture the general inflator pressure response.

4.1.2 Linear Impactor Test

The linear impactor response was evaluated to assess how the tuned CPG model compares with the correlated CPM reference model under controlled mechanical loading. The comparison was based on the impactor displacement, velocity, acceleration, and force–displacement response, as shown in Figure 4.2. These quantities describe the global motion of the impactor and the resistance generated by the airbag during compression. The acceleration response was filtered using CFC180 and scaled by -1 to improve comparability between the two methods.

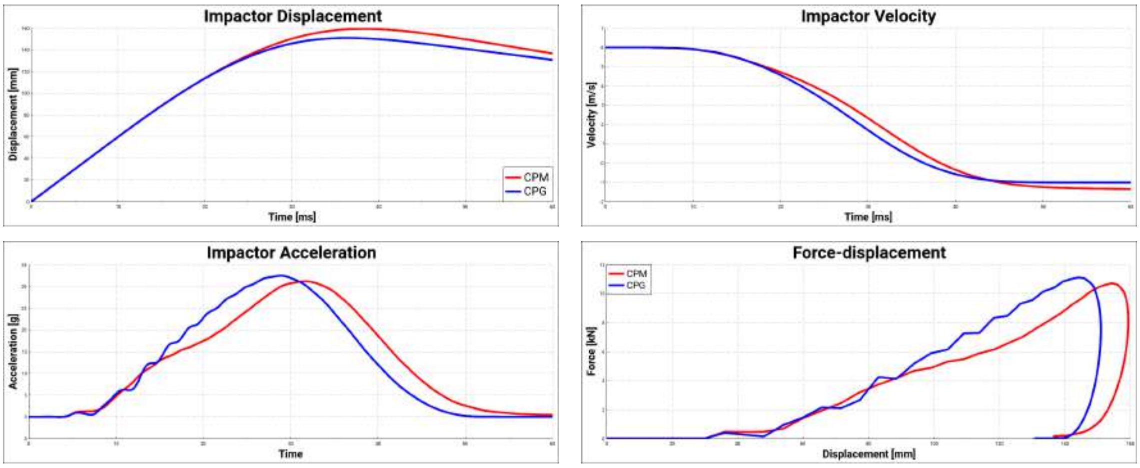

Figure 4.2: Linear impactor response for the correlated CPM reference model and the tuned CPG model.

The results show that CPM and CPG follow the same overall response trend during the early part of the impactor motion. As the airbag loading becomes more pronounced, the two methods begin to deviate. The tuned CPG model generally produces an earlier deceleration of the impactor, which is reflected by a lower displacement response and an earlier acceleration peak. This is also supported by the force–displacement response, where CPG develops a higher force at a lower displacement during the main loading phase. CPM, in contrast, shows a smoother and slightly delayed response, resulting in a higher maximum displacement and a later force build-up.

The main observations from the linear impactor response are summarized in Table 4.2. The table presents the key differences between CPM and CPG for each evaluated response quantity.

Table 4.2: Summary of the linear impactor response comparison between CPM and CPG.

Response quantity	CPM	CPG	Overall observation
Impactor displacement	Peak displacement of approximately 160 mm. Final displacement of approximately 137 mm.	Peak displacement of approximately 150 mm. Final displacement of approximately 130 mm.	Good agreement up to approximately 25 ms. CPG gives a lower peak and final displacement, while both curves show similar curvature.
Impactor velocity	Velocity decreases more gradually and converges at approximately −1.5 m/s around 50 ms.	Velocity decreases earlier and converges at approximately −1 m/s around 43 ms.	Good agreement up to approximately 20 ms. CPG decelerates the impactor earlier than CPM.
Impactor acceleration	Peak acceleration of approximately 0.305 m/s^2 at around 32 ms.	Peak acceleration of approximately 0.32 m/s^2 at around 28–29 ms.	Good agreement up to approximately 15 ms. CPG reaches a slightly higher and earlier peak, while CPM shows a delayed response.
Force–displacement response	Force builds up more gradually and reaches its maximum at a larger displacement.	Force builds up earlier and reaches a slightly higher maximum force at a lower displacement.	CPG shows a stiffer loading response during the main compression phase, while CPM allows a larger displacement before reaching its maximum force.

Overall, the tuned CPG model shows good agreement with the correlated CPM reference during the initial impactor response. The main deviation occurs during the stronger loading phase, where CPG predicts a slightly earlier and stronger resistance from the airbag compared with CPM. This is reflected by the earlier velocity reduction, earlier acceleration peak, lower maximum displacement, and higher force level for a given displacement in the force–displacement response.

4.2 Airbag–Occupant Interaction

This subsection presents the results related to airbag–occupant interaction. First, an assessment of the test-case reliability is presented, followed by the SAB pressure response, airbag unfolding behaviour, arm trajectory, and occupant-related injury metrics.

For each result type, dedicated post-processing was performed to enable a consistent comparison between physical tests and CAE. For the snapshot comparisons, a 5 ms time shift was applied to account for the seat-squash phase in CAE and to ensure equal time-to-fire between the CAE and physical test snapshots. Image and video synchronization was then used to match the frame rate of the physical test videos with the output frequency of the CAE results.

The occupant injury and arm trajectory plots were processed using the same overall post-processing workflow. The physical test signals and corresponding CAE responses were aligned in time, filtered where required, and scaled to account for differences in unit systems and signal conventions. Acceleration channels were converted to gravitational acceleration using source-specific scaling factors, where the CAE acceleration responses were scaled by 102 and the physical test responses by 0.102. For the SAB pressure response, the CAE pressure was shifted by 100 kPa to account for ambient pressure and enable comparison with the physical test pressure signal. Polarity corrections were applied only for channels where the physical and numerical responses had clearly opposite orientations.

Plot trimming was applied where required to focus the comparison on the relevant response phase. For the SAB pressure plots, the displayed range was selected to emphasize the pressure development associated with the airbag deployment characteristics. Consequently, the initial ignition-pressure phase was not used as the primary basis for the visual comparison. Similar trimming was applied to the occupant injury and arm trajectory plots to focus the evaluation on the time interval where the main occupant–airbag interaction occurred.

For the arm-moment plots, an additional scaling factor of 10 was applied in the Y direction. This was introduced to bring the curve amplitudes into a comparable visual range and to support assessment of the relative timing, shape, and dynamic response trends. The CAE arm-moment curves should therefore primarily be interpreted in relation to their dynamic agreement with the physical tests, rather than as direct quantitative output values.

Furthermore, for visual comparison purposes, the right arm of the Hybrid III ATD was hidden in the CAE model. This was done because the arm was not relevant to the evaluated interaction and to provide more consistent visual conditions between the CAE results and the physical tests.

4.2.1 Test Case Reliability

In general, the physical repeatability is high, as most test cases show limited variation between the repeated physical tests. However, the reliability assessment is primarily influenced by the CAE comparability, since this metric determines how representative the simulations are of the corresponding physical test conditions. Table 3.2 presents the eight testcases assessed below.

Test no. 1, corresponding to WorldSID-50M with an initial clearance of 80 mm, is assessed as moderately reliable. This is because a small part of the arm penetrates the plexiglass in the CPM simulation. However, this occurs at a later stage than the primary time interval of interest, meaning that relevant evaluations can still be performed during the early deployment phase. Test no. 2–4 are assessed as highly reliable, as no major issues or deviations are observed between the physical tests and the virtual simulations. The full-arm test cases are assigned lower reliability, primarily because the physical tests and the CAE simulations use different ATDs. For test no. 5 and 6, additional differences related to arm angle and steering-wheel boundary conditions further reduce the CAE comparability.

All test cases are included in the subsequent qualitative and quantitative assessment. A summary of the reliability evaluation is presented in Table 4.3.

Table 4.3: Reliability assessment of the investigated test cases.

Test no.	Physical repeatability	CAE comparability	Reliability score	Comment
1	4 – High	3 – Moderate	3.25/5	Arm penetrates the plexiglass in the CPM simulation at a later stage.
2	5 – Very high	5 – Very high	5/5	–
3	5 – Very high	5 – Very high	5/5	–
4	4 – High	5 – Very high	4.75/5	Minor deviation in the arm trajectory is observed towards the end of the physical test.
5	4 – High	1 – Very low	1.75/5	Different ATD, arm angle, and steering-wheel boundary conditions.
6	4 – High	1 – Very low	1.75/5	Different ATD, arm angle, and steering-wheel boundary conditions.
7	4 – High	2 – Low	2.50/5	Different ATD used in CAE and physical testing.
8	5 – Very high	2 – Low	2.75/5	Different ATD used in CAE and physical testing.

The assessed test cases are therefore carried forward in the report together with their individual reliability scores, allowing the subsequent discussion and conclusions to be interpreted in relation to the assessed reliability of each case.

4.2.2 Side-Airbag Pressure

The SAB pressure response was evaluated to assess how the two CAE gas methods reproduce the pressure development inside the airbag during deployment. An initial observation was that CPG generally produced a higher initial pressure peak than CPM and the physical tests. However, the initial peak pressure should be interpreted with caution and was therefore not used as the primary basis for comparing the gas methods.

The main reason for this is that the initial pressure peak is strongly influenced by the inflator characteristics, ignition phase, and the numerical representation of the gas injection. Small differences in these input conditions can have a large influence on the peak magnitude, even if the subsequent pressure development follows a physically reasonable trend. In addition, the pressure response is not obtained in an identical manner in the physical tests and in CAE. In the physical tests, the pressure is measured locally using a pressure probe, while the CAE pressure represents an averaged pressure quantity in the airbag. As a result, differences in the initial peak may be affected by both the gas method and the measurement approach.

For this reason, the evaluation focuses primarily on the pressure response after the initial peak. This part of the response is considered more relevant for assessing how the gas method represents the pressure development during airbag expansion and occupant interaction. The pressure plots were therefore evaluated with emphasis on the initial post-peak response (10-20 [ms]), the subsequent pressure decay (20-40 [ms]), and the late-stage pressure level (40-60 [ms]). The SAB pressure plots generated in this project are presented in Figure 4.3.

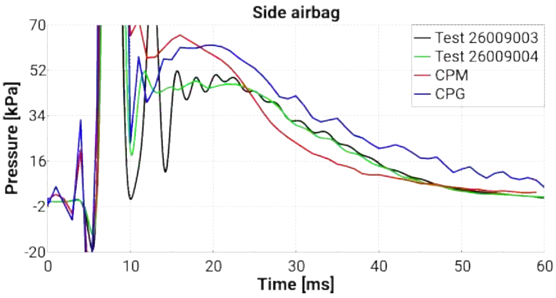

(a) Test Case 1: WorldSID-50M, 80 mm

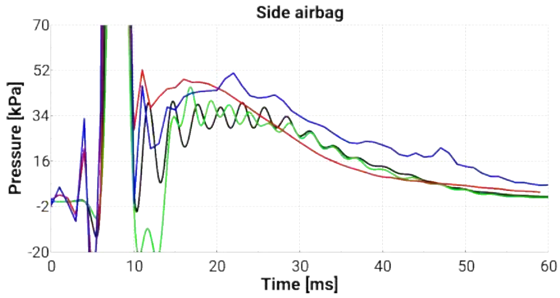

(b) Test Case 2: WorldSID-50M, 120 mm

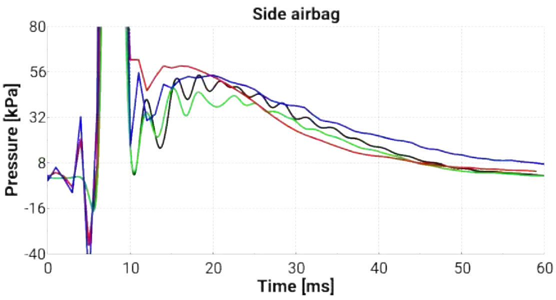

(c) Test Case 3: SID-IIs, 80 mm

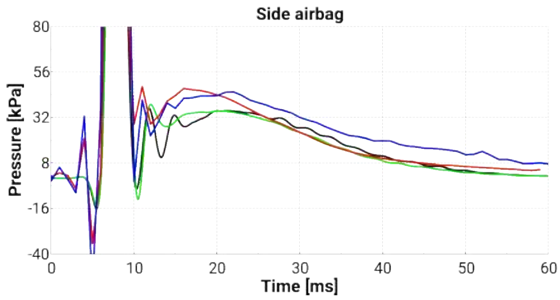

(d) Test Case 4: SID-IIs, 120 mm

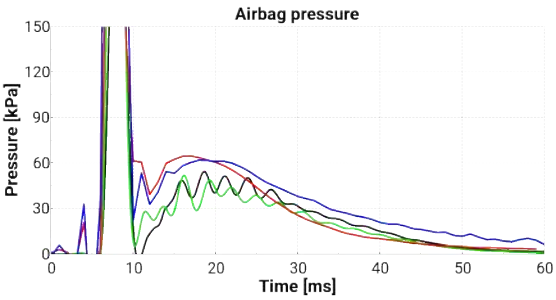

(e) Test Case 5: SID-IIs, full arm, driver position, 80 mm

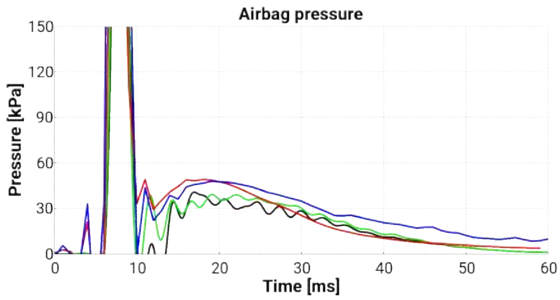

(f) Test Case 6: SID-IIs, full arm, driver position, 120 mm

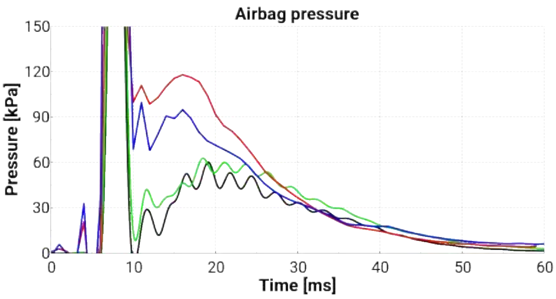

(g) Test Case 7: SID-IIs, full arm, relaxed position, 80 mm

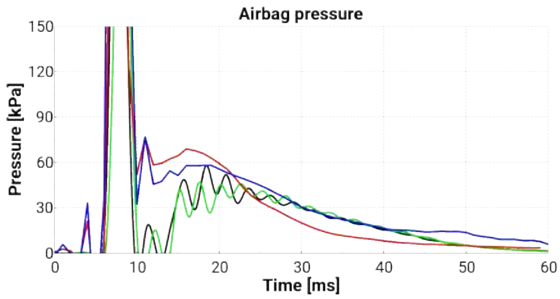

(h) Test Case 8: SID-IIs, full arm, relaxed position, 120 mm

Figure 4.3: SAB pressure response for the investigated test cases.

After the initial pressure peak, the repeated physical tests show some variation in the early post-peak response. This is particularly visible in the pressure recovery immediately after deployment, where the two physical tests may differ in both timing and magnitude. However, during the subsequent pressure decay and late-stage response, the physical tests generally show good agreement. This indicates that the physical pressure response is more consistent during the later part of the evaluated time window. The main pressure-response observations are summarized in Table 4.4.

Table 4.4: Summary of the main observations from the SAB pressure response.

Test no.	Early post-peak	Pressure decay	Late-stage level
1	CPG closer; CPM overpredicts.	CPM approaches tests; CPG remains higher.	CPM converges; CPG remains higher.
2	CPG closer; CPM slightly higher.	CPM closer; CPG remains higher.	CPM converges; CPG remains higher.
3	CPG closer than CPM.	Similar trends; CPM lower, CPG higher.	CPM converges; CPG remains higher.
4	CPG closer; CPM slightly higher.	CPM closer; CPG slightly higher.	CPM correlates well; CPG remains slightly higher.
5	Both overpredict; CPG slightly closer.	CPM closer; CPG remains higher.	CPM approaches tests; CPG remains higher.
6	CPG closer; CPM higher.	Similar decay trend; CPG remains higher.	CPM closer; CPG remains higher.
7	Both overpredict; CPM deviates most.	Both follow the decay reasonably well.	Both converge with minor differences.
8	Both overpredict; CPG closer.	CPG closer; CPM becomes lower.	CPM converges; CPG remains higher.

Overall, the pressure results show a consistent difference between the two gas methods after the initial peak. CPG generally captures the early post-peak response more closely than CPM, particularly during the first part of the pressure recovery after deployment. However, during the subsequent decay phase, CPM more often follows the physical pressure trend and converges towards the physical tests at later times. CPG tends to maintain a higher pressure level during the late-stage response in several test cases. These observations indicate that CPG provides a stronger representation of the early pressure development, while CPM generally shows better agreement during the later pressure decay.

4.2.3 Airbag Unfolding Behavior

This section presents the unfolding behavior of the simulated airbag in comparison with the corresponding physical tests. The evaluation is limited to the SID-IIs 120 mm test case, since the focus is on the early deployment phase before substantial interaction with the ATD occurs. The comparison is performed at selected time steps after the airbag time to fire (TTF), chosen to capture the main stages of the unfolding sequence from initial deployment to a more developed airbag shape. The full unfolding sequence from 0 to 5.5 ms after TTF is shown in Figure 4.4. The remaining unfolding sequences for the other test cases are presented in Appendix C. Since the initial airbag deployment conditions are equivalent across the test cases, no separate qualitative observations are provided for these cases.

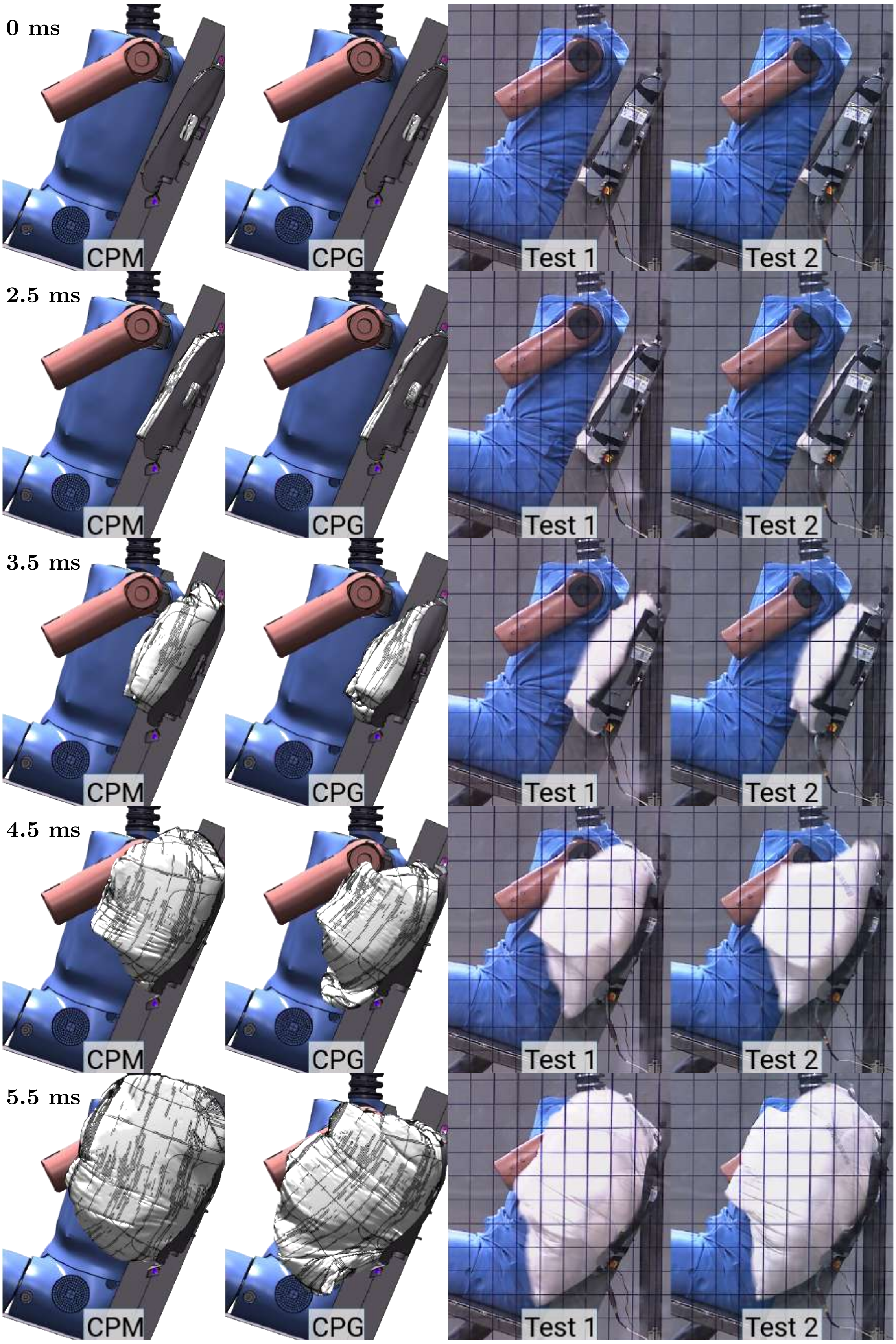

Figure 4.4: Unfolding behavior of the airbag for test case 4: SID-IIs - 120 mm.

The qualitative observations are summarized in Table 4.5. At 2.5 ms after TTF, both CAE methods capture the initial protrusion of the airbag from the housing. CPM shows a slightly larger visible deployed volume than CPG, while the physical tests appear to fall between the two simulations. At this stage, CPM shows closer similarity to Test 1, whereas CPG shows closer similarity to Test 2.

At 3.5 ms after TTF, differences in global airbag shape become more visible. CPM develops a more rounded geometry, while CPG shows a more elongated and elliptical profile. The physical tests show a similar elongated external expansion, indicating that CPG is visually closer in terms of protrusion direction and global shape. The bracket deformation also suggests that both CAE methods are slightly advanced in time relative to the physical tests, with this effect being more pronounced for CPM.

At 4.5 and 5.5 ms after TTF, the later unfolding behavior is characterized by larger differences in fabric shape and crease formation. CPG captures more local folding and lower-region development, while CPM remains smoother and more spherical. At 5.5 ms, CPG shows closer qualitative agreement with the physical tests regarding crease formation and fabric deformation. However, CPM captures the unfolding of the upper airbag region more clearly at the final evaluated time step.

Table 4.5: Qualitative observations of the airbag unfolding behavior for the SID-IIs 120 mm test case.

Time	CPM	CPG	Physical test	Overall assessment
2.5 ms	Earlier and slightly larger protrusion.	Slightly smaller initial protrusion.	Early protrusion between CPM and CPG.	Both methods capture the initial deployment.
3.5 ms	More rounded airbag shape.	More elongated and elliptical profile.	Similar elongated external expansion.	CPG is closer in global shape and protrusion direction.
4.5 ms	Larger and more spherical expansion.	More distinct folds and lower-region development.	Continued expansion with visible fabric deformation.	CPG better represents local folding, while CPM remains more rounded.
5.5 ms	Smoother global contour, but clearer upper-region unfolding.	More visible creases and irregular fabric surface.	Developed airbag shape with visible folding.	CPG better captures crease formation, while CPM better captures the upper unfolding.

Overall, CPG shows closer visual agreement with the physical tests during the later stages of the unfolding process, particularly regarding local folding, lower-region development, and crease formation. CPM captures the general deployment sequence, but tends to produce a smoother and more rounded airbag shape.

4.2.4 Arm Trajectory

This section presents selected arm-trajectory results for the half-arm and full-arm dummy configurations. The half-arm cases are evaluated visually from snapshot comparisons, with focus on the observed arm motion relative to the physical tests. For the full-arm cases, the visual comparison is complemented by arm-moment plots and numerical peak-amplitude summaries, since these provide additional information about the dynamic arm response. The remaining test results are provided in Appendices A, B, D and E

4.2.4.1 Test Case 2

For this test case, selected snapshots are presented at 0, 15, 45, and 60 ms, as shown in Figure 4.5 and Figure 4.6. The physical test repeatability is very good, with Test 1 and Test 2 showing closely matching arm motion at all presented timesteps. Consequently, this test case was assigned a reliability score of 5/5, as presented in Table 4.3.

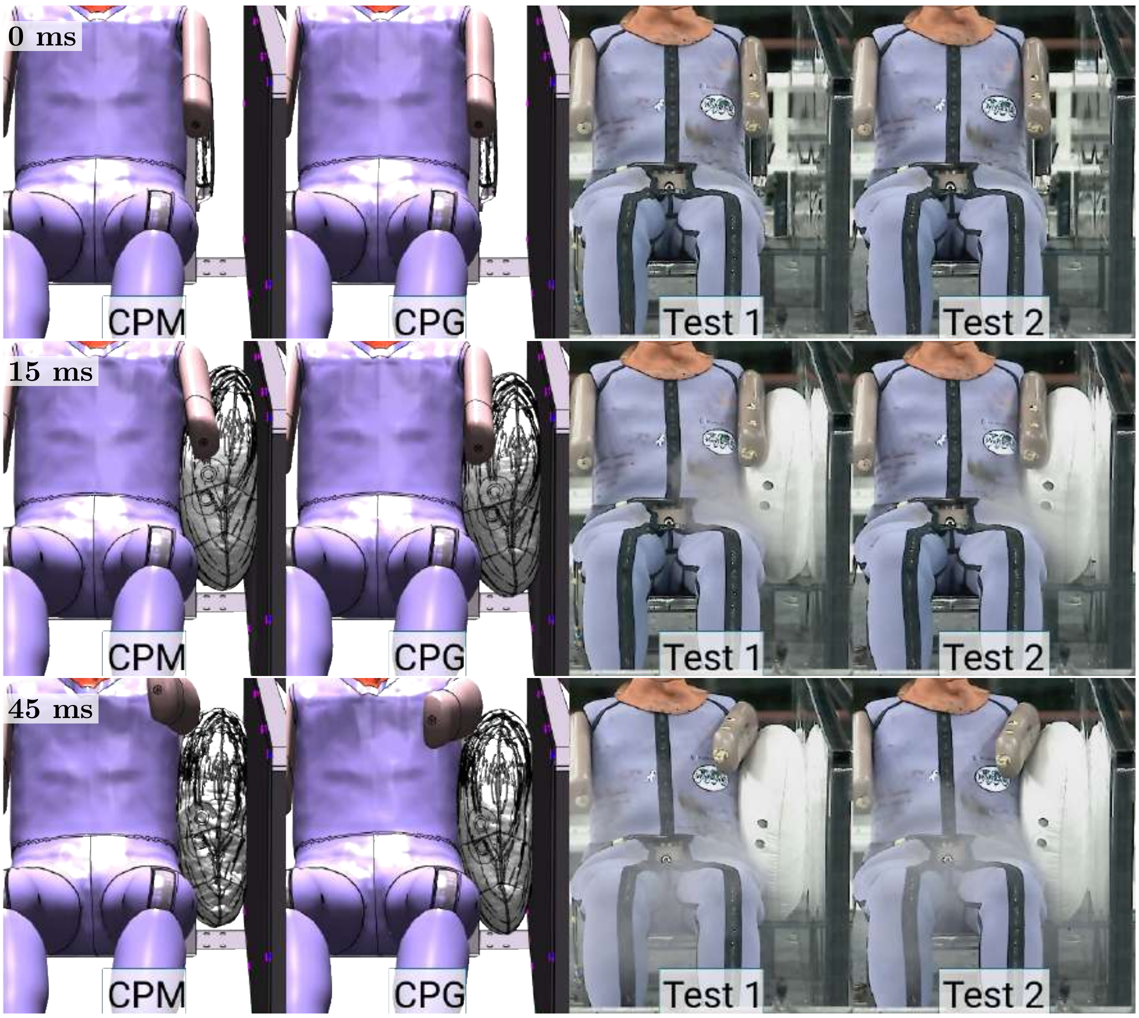

Figure 4.5: Arm trajectory snapshots for the WSID50 120 mm test case.

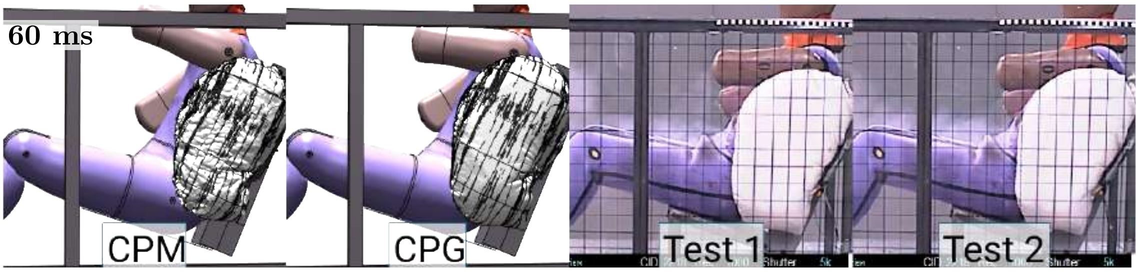

Figure 4.6: LHS view of the WSID50 120 mm test case at 60 ms.

The qualitative observations from the arm-trajectory comparison are summarized in Table 4.6. The assessment focuses on airbag alignment, arm position in the XZ-plane, and arm motion in the YZ-plane.

Table 4.6: Qualitative observations of the arm trajectory for the WorldSID-50M 120 mm test case compared to the physical tests.

Time	CPM	CPG	Overall assessment
15 ms	The airbag appears to deploy between the thorax and the arm, resulting in an arm angle directed toward the plexiglass. This behavior is not observed to the same extent in the physical tests.	The airbag appears to deploy more laterally beside the arm, which is more consistent with both physical tests.	CPG provides a closer representation of the early arm–airbag interaction, while CPM shows a less representative initial arm displacement.
45 ms	The arm position is higher in the XZ-plane compared to the physical tests, while the inward arm motion in the YZ-plane is smaller than observed in the physical tests.	The arm position is also higher in the XZ-plane compared to the physical tests, while the inward arm motion in the YZ-plane is larger than observed in the physical tests.	Both methods show deviations from the physical tests, but CPG provides better overall agreement in the global arm trajectory.
60 ms	The arm remains higher in the XZ-plane compared to the physical tests. However, the inward arm angle in the YZ-plane is similar to the physical response.	The arm is also positioned higher in the XZ-plane, but the final arm position is closer to the physical tests. The inward arm angle in the YZ-plane is also similar to the physical response.	CPG provides a better final arm position compared to CPM. However, both CPM and CPG capture a similar inward arm angle in the YZ-plane.

Overall, CPG provides a closer representation of the arm trajectory compared to

CPM. Although deviations remain between CPG and the physical tests, the deviations are generally larger for CPM.

4.2.4.2 Test case 4

This test case was assigned a reliability score of 4.75/5. The physical test repeatability is good; however, some variation is observed between Test 1 and Test 2, as shown in Figure 4.7. In Test 1, the arm appears to be subjected to a stronger inward interaction, resulting in a more pronounced inward angle in the YZ-plane. In Test 2, the inward angle is less pronounced. Due to this variation, the physical test repeatability was assigned a score of 4/5, as presented in Table 4.3.

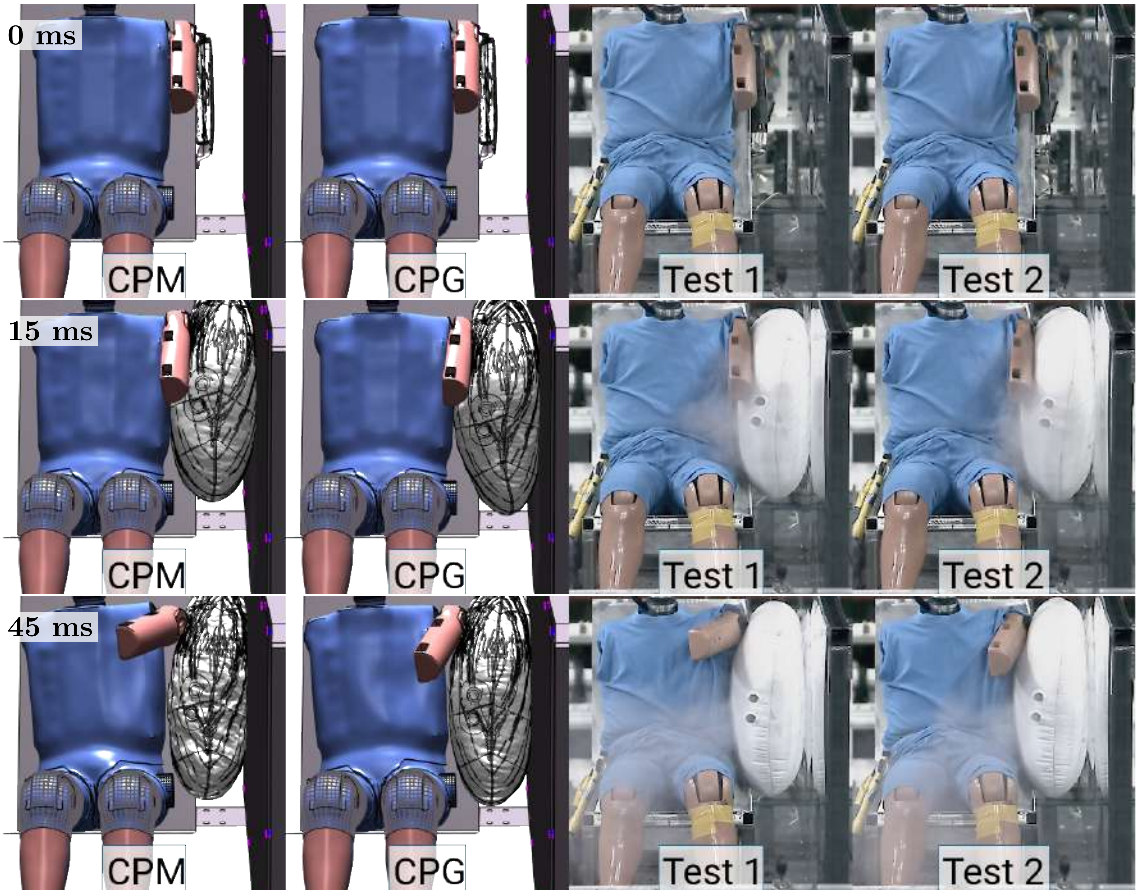

Figure 4.7: Arm trajectory snapshots for the SID-IIs 120 mm test case.

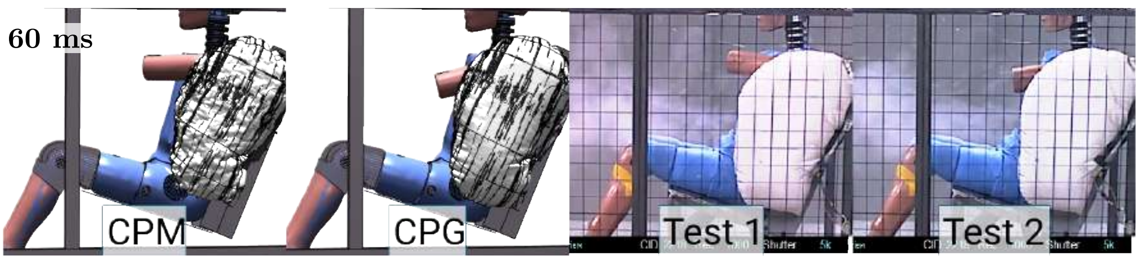

Figure 4.8: LHS view of the SID-IIs 120 mm test case at 60 ms.

The main qualitative observations from the presented snapshots are summarized in Table 4.7.

Table 4.7: Qualitative observations of the arm trajectory for the SID-IIs – 120 mm test case compared to the physical tests.

Time	CPM	CPG	Overall assessment
15 ms	The airbag deploys laterally beside the arm and produces an early outward arm displacement. The arm–airbag interaction appears closer to Test 1.	The airbag also deploys laterally beside the arm, although with a slightly different alignment relative to the arm. The response appears closer to Test 2.	Both methods capture the early lateral airbag expansion and the initial arm displacement. Due to the observed differences between the physical tests, no clear preference between CPM and CPG can be established at this stage.
45 ms	The arm position and rotation are visually closer to Test 1, particularly with respect to the outward arm position in the front view.	The arm position and rotation are visually closer to Test 2, with a slightly different arm angle and airbag alignment.	CPM and CPG each show reasonable agreement with one of the physical tests. The variation between Test 1 and Test 2 limits the possibility of identifying either method as clearly more representative.
60 ms	The final arm position remains close to the trend observed in Test 1, including the arm angle in the LHS view.	The final arm position remains close to the trend observed in Test 2, including the arm angle in the LHS view.	Both methods capture the general final arm position and inward arm angle. Since CPM aligns more closely with Test 1 and CPG aligns more closely with Test 2, the comparison does not indicate a clear advantage for either method.

Overall, both CPM and CPG provide a reasonable representation of the arm trajectory for this test case. However, the physical tests show noticeable variation, with CPM corresponding more closely to Test 1 and CPG corresponding more closely to Test 2. Therefore, this test case does not provide sufficient basis to conclude that either gas method gives a clearly better prediction of the arm trajectory.

4.2.4.3 Test Case 5

For the full-arm driver-position 80 mm case, it is difficult to identify clear differences from the front-view trajectory comparison shown in Figure 4.9, apart from the elbow bending further inward in CAE compared with the physical tests. The steering wheel also shows more deformation in the physical tests than in the CAE simulations. The LHS view shown in Figure 4.10 at 60 ms provides additional information, where the same inward arm motion remains visible relative to the physical tests.

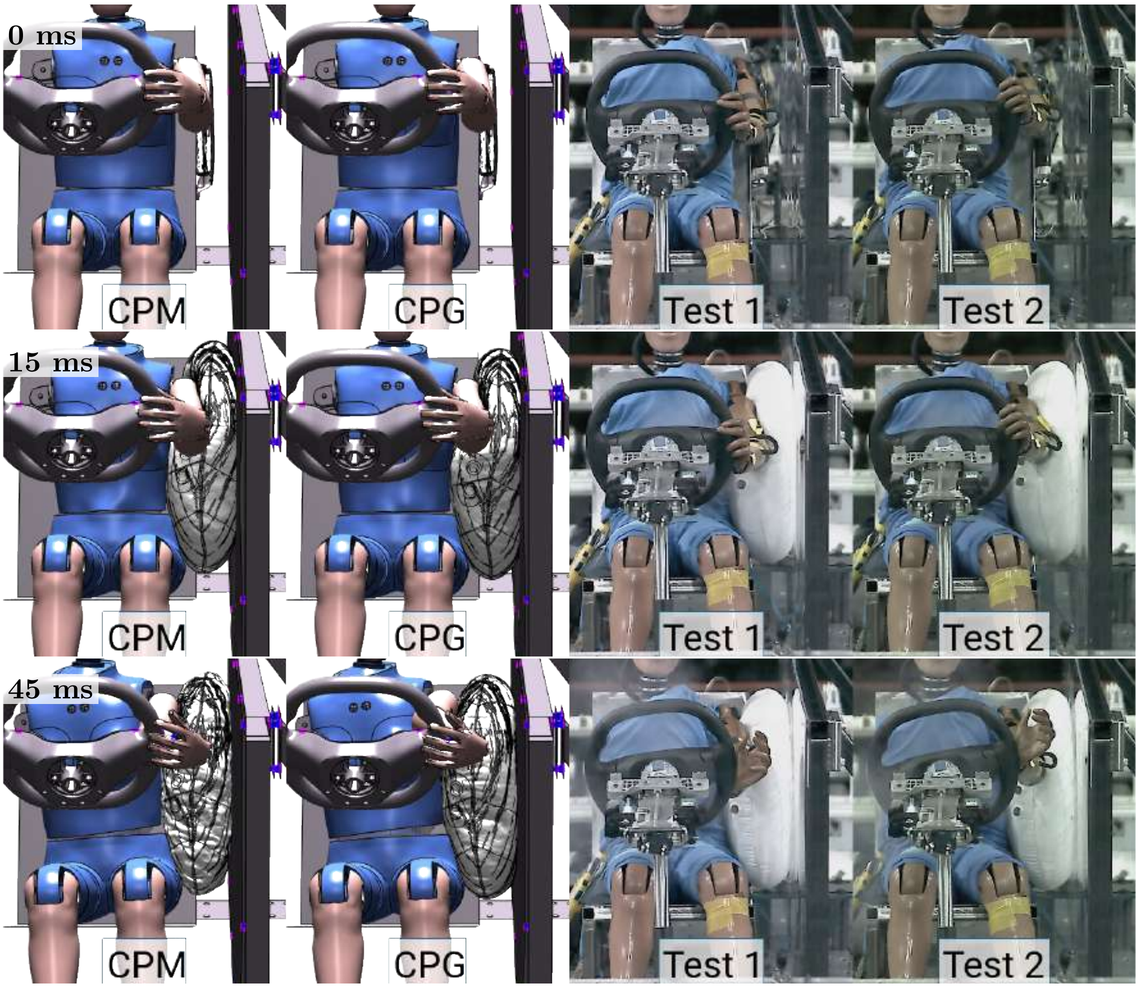

Figure 4.9: Arm trajectory snapshots for the full-arm driver-position 80 mm test case.

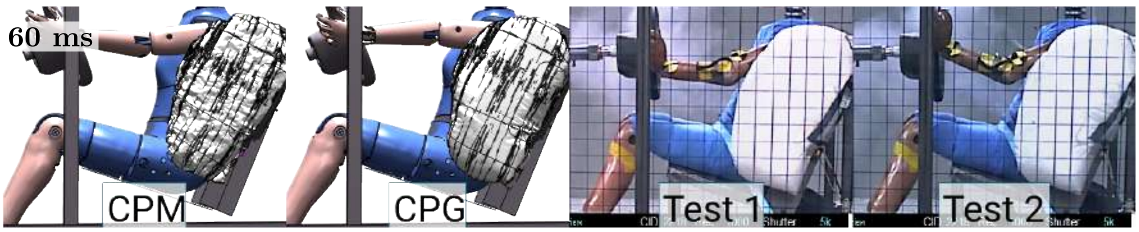

Figure 4.10: LHS view of the full-arm driver-position 80 mm test case at 60 ms.

The arm-moment plots provide additional information for the full-arm driver-position 80 mm case. As shown in Figure 4.11, a large deviation from the physical tests is observed for both CAE methods. A spread between the physical tests is also present, especially for the forearm X moment. The corresponding numerical comparison is provided in Table 4.8.

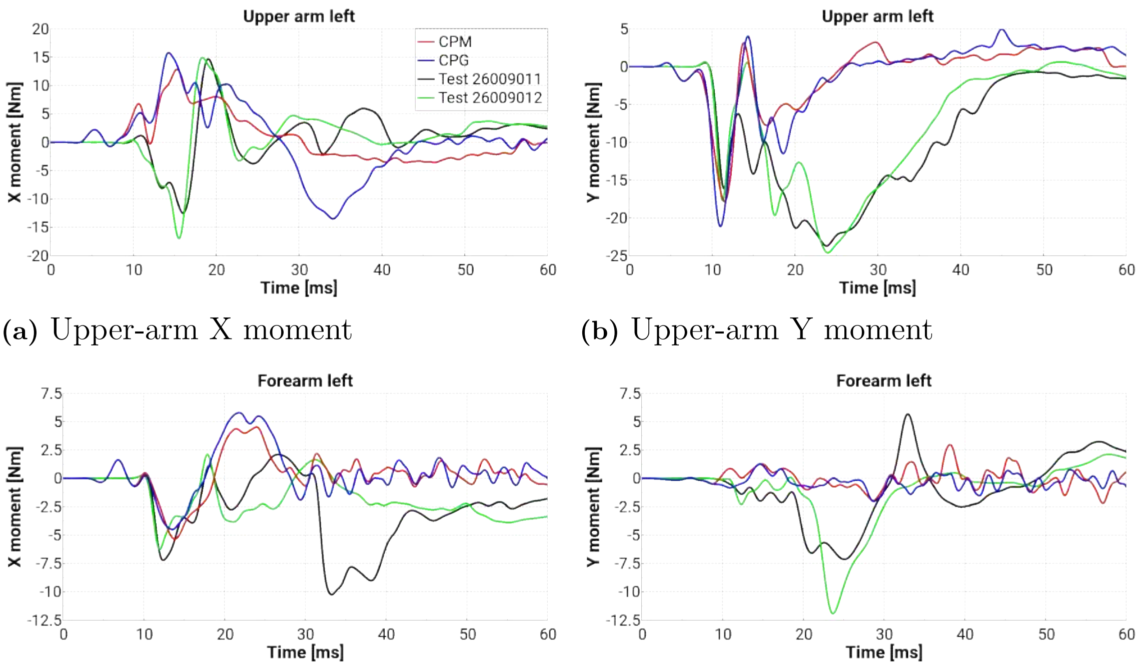

(a) Upper-arm X moment

(b) Upper-arm Y moment

(c) Forearm X moment

(d) Forearm Y moment

Figure 4.11: Arm moment responses for the full-arm driver-position 80 mm test case.

Table 4.8: Numerical arm-moment results for the full-arm driver-position 80 mm case.

Metric [Nm]	$\bar{x}_{\text{test}}$	x_{CPM}	x_{CPG}	$\lvert\Delta_{\text{CPM}}\rvert$	$\lvert\Delta_{\text{CPG}}\rvert$	Closest
Upper-arm X moment	-1.2	12.8	15.8	14.0	16.9	CPM
Upper-arm Y moment	-24.2	-17.8	-21.2	6.3	3.0	CPG
Forearm X moment	-8.3	-5.3	5.8	2.9	14.0	CPM
Forearm Y moment	-9.5	3.0	-2.0	12.5	7.5	CPG
$E_{m,F}$	–	–	–	8.9	10.4	CPM
I_F: CPM mean improvement over CPG = 13.8%						

4.2.4.4 Test Case 7

For the 80 mm relaxed-position test case, the visual differences between CAE and the physical tests are clearer. Both CPG and CPM show the elbow region becoming wrapped inside the airbag fabric, which is not observed in the physical tests, as shown in Figure 4.12. Towards the end of the sequence, CPM appears closer to the physical tests, while CPG reaches further forward. Both CAE methods show yaw-dominated neck and head motion, whereas the physical tests appear mainly influenced by roll motion. The LHS view at 60 ms is shown in Figure 4.13.

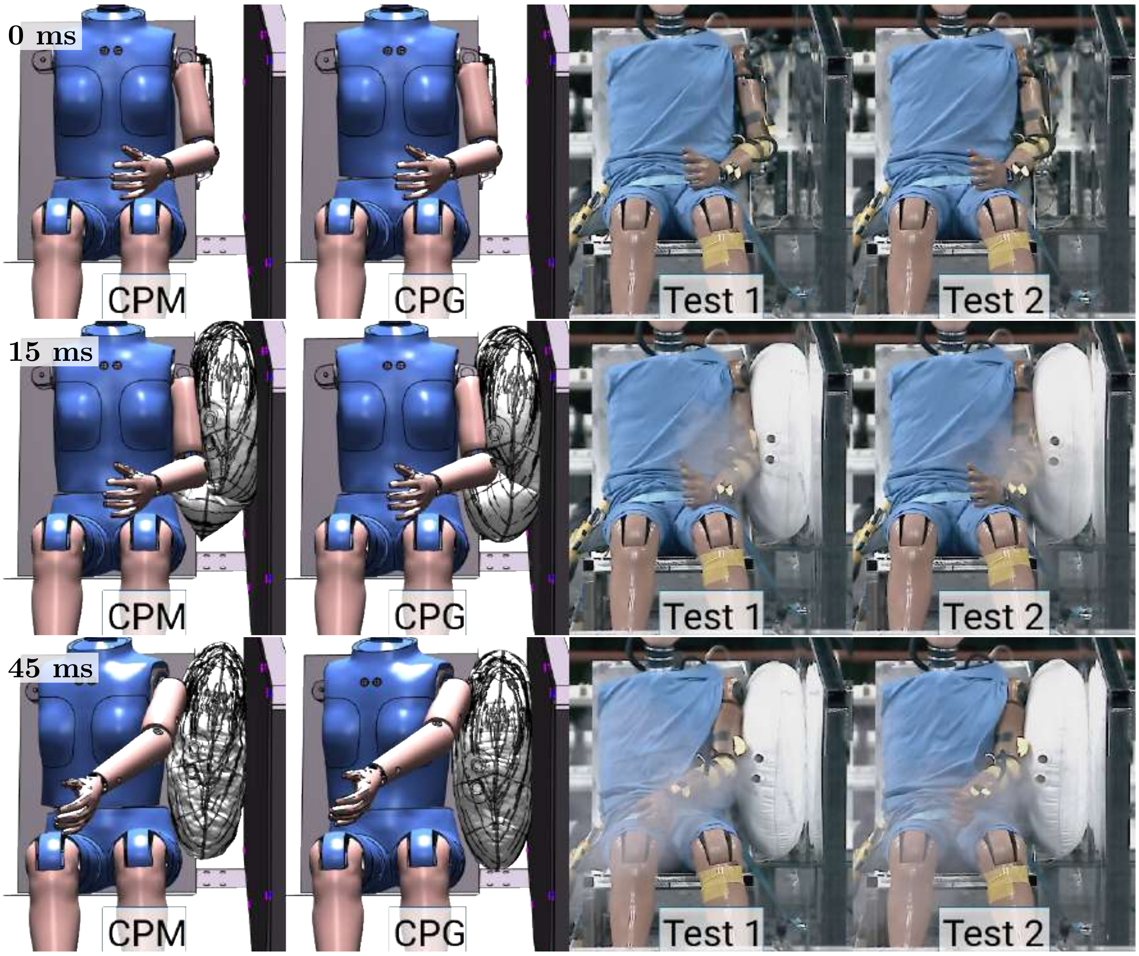

Figure 4.12: Arm trajectory snapshots for the full-arm relaxed-position 80 mm test case.

Figure 4.13: LHS view of the full-arm relaxed-position 80 mm test case at 60 ms.

Regarding the arm-moment plots for the relaxed-position dummy, the CAE results align more closely with the physical tests than in the driver-position configuration. In particular, the upper-arm Y moment aligns closely with the physical tests. Another observed trend is that the CPG results appear to capture the dynamics of the physical tests more closely than CPM, as shown in Figure 4.14. The corresponding numerical comparison is provided in Table 4.9.

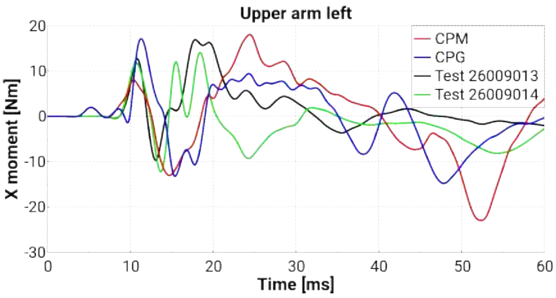

(a) Upper-arm X moment

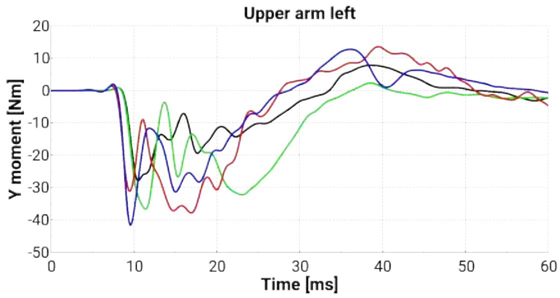

(b) Upper-arm Y moment

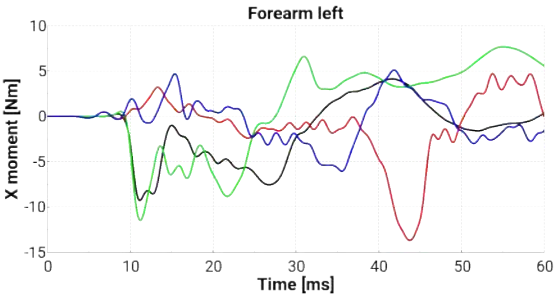

(c) Forearm X moment

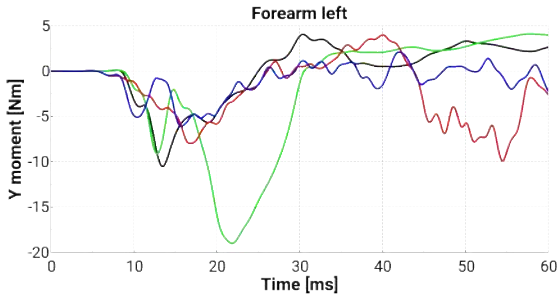

(d) Forearm Y moment

Figure 4.14: Arm moment responses for the full-arm relaxed-position 80 mm test case.

Table 4.9: Numerical arm-moment results for the full-arm relaxed-position 80 mm case.

Metric [Nm]	$\bar{x}_{\text{test}}$	x_{CPM}	x_{CPG}	$\lvert\Delta_{\text{CPM}}\rvert$	$\lvert\Delta_{\text{CPG}}\rvert$	**Closest**
Upper-arm X moment	15.5	-23.0	17.2	38.5	1.7	CPG
Upper-arm Y moment	-32.3	-37.9	-41.6	5.6	9.4	CPM
Forearm X moment	-10.4	-13.7	-6.1	3.3	4.3	CPM
Forearm Y moment	-14.8	-9.9	-6.1	4.8	8.6	CPM
$E_{m,F}$	–	–	–	13.0	6.0	CPG
I_F: CPG mean improvement over CPM = 54.0%						

4.2.5 Occupant-Related Injury Metrics

Table 4.10 summarizes the grouped mean absolute differences between the CAE simulations and the physical-test averages. The values therefore represent the average deviation from the physical tests within each response family, rather than the response magnitudes themselves. Lower values indicate closer agreement with the physical tests.

For the thoracic and rib response families, CPG showed the lowest grouped mean absolute differences, with relative improvements of 34.1% and 38.9%, respectively. This indicates that CPG provided closer agreement with the physical tests for these response families. The pelvic response families also showed lower grouped mean absolute differences for CPG; however, the corresponding improvements were small, with 3.0% for the half-arm pelvic responses and 1.4% for the full-arm pelvic responses. These pelvic differences should therefore be interpreted as marginal in comparison with the thoracic and rib response differences.

Since the grouped values are reported in different physical units, the response families should not be compared directly against each other. Instead, the table is intended to compare CPM and CPG within each response family.

Table 4.10: Magnitude-based grouped average-difference summary.

Response family	Unit	$\bar{E}_{\mathrm{CPM},F}$	$\bar{E}_{\mathrm{CPG},F}$	Closest	I_F
Thoracic	g	3.27	2.16	CPG	34.1%
Rib	mm	2.79	1.70	CPG	38.9%
Half-arm pelvic	g	3.93	3.81	CPG	3.0%
Full-arm pelvic	g	25.17	24.82	CPG	1.4%

4.2.5.1 Test Case 3: Rib Responses

The SID-IIs 80 mm rib responses indicate agreement between the CAE simulations and the physical tests when reviewing the visual response in Figure 4.15. The extracted maximum absolute amplitudes in Table 4.11 show that CPG gives the lower mean absolute difference for the rib response family, although CPM is closest for Rib 1.

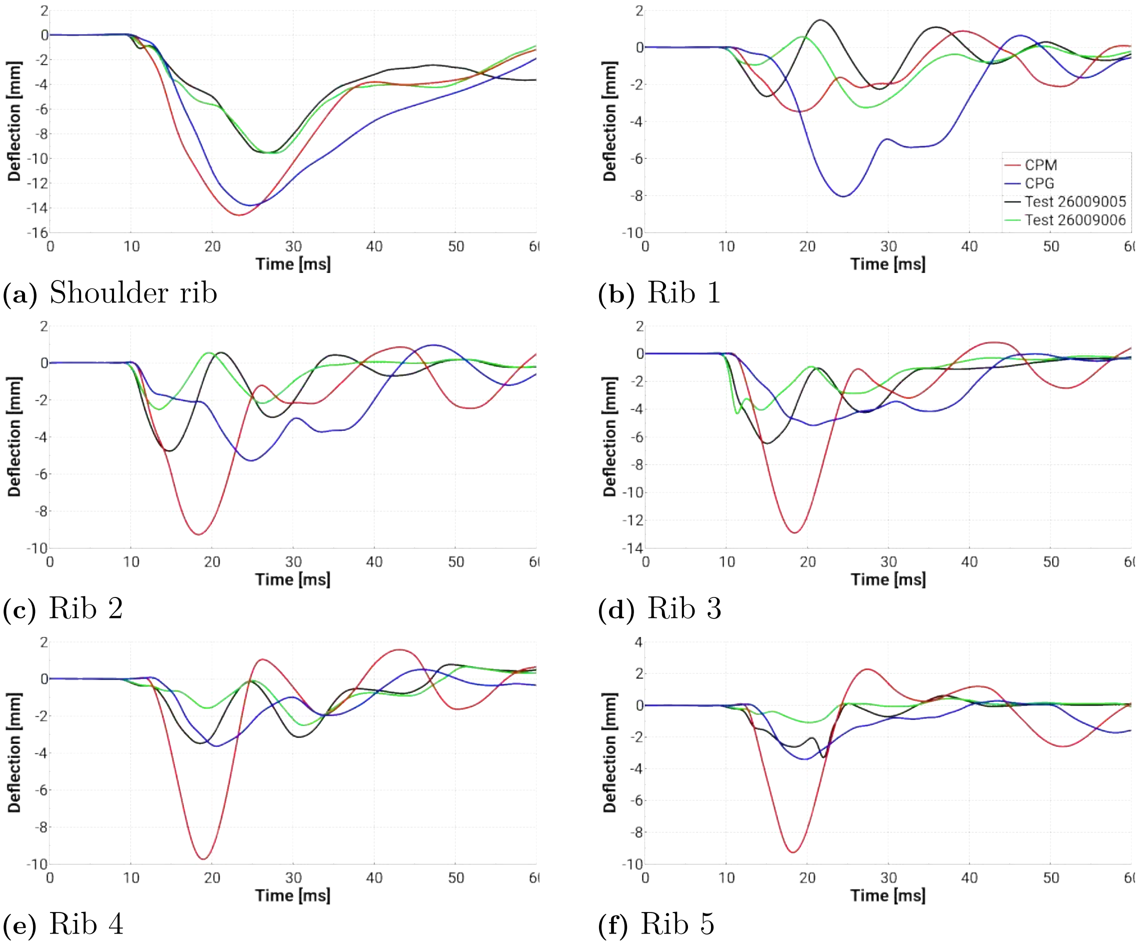

(a) Shoulder rib (b) Rib 1 (c) Rib 2 (d) Rib 3 (e) Rib 4 (f) Rib 5

Figure 4.15: SIDIIS 80 mm rib responses for CPM, CPG and physical testing.

Table 4.11: Signed peak rib-deflection results for the SIDIIS 80 mm case.

Metric [mm]	$\bar{x}_{\text{test}}$	x_{CPM}	x_{CPG}	$\|\Delta_{\text{CPM}}\|$	$\|\Delta_{\text{CPG}}\|$	Closest
Shoulder rib	-9.56	-14.59	-13.80	5.03	4.24	CPG
Rib 1	-2.95	-3.46	-8.05	0.51	5.10	CPM
Rib 2	-3.64	-9.27	-5.29	5.63	1.65	CPG
Rib 3	-5.40	-12.91	-5.17	7.51	0.22	CPG
Rib 4	-2.99	-9.74	-3.63	6.75	0.64	CPG
Rib 5	-2.18	-9.27	-3.40	7.09	1.22	CPG
$E_{m,F}$	–	–	–	5.42	2.18	CPG
I_F: **CPG mean improvement over CPM = 59.8%**						

4.2.5.2 Test Case 2: Thoracic Responses

The WorldSID-50M 120 mm thoracic acceleration responses show a distinct spiking tendency in the physical test data for the X-direction channels. This behaviour is not represented to the same extent by the CAE simulations. The numerical comparison in Table 4.12 indicates that the closest method varies between individual channels, while CPG gives the lower mean absolute difference for the complete thoracic response.

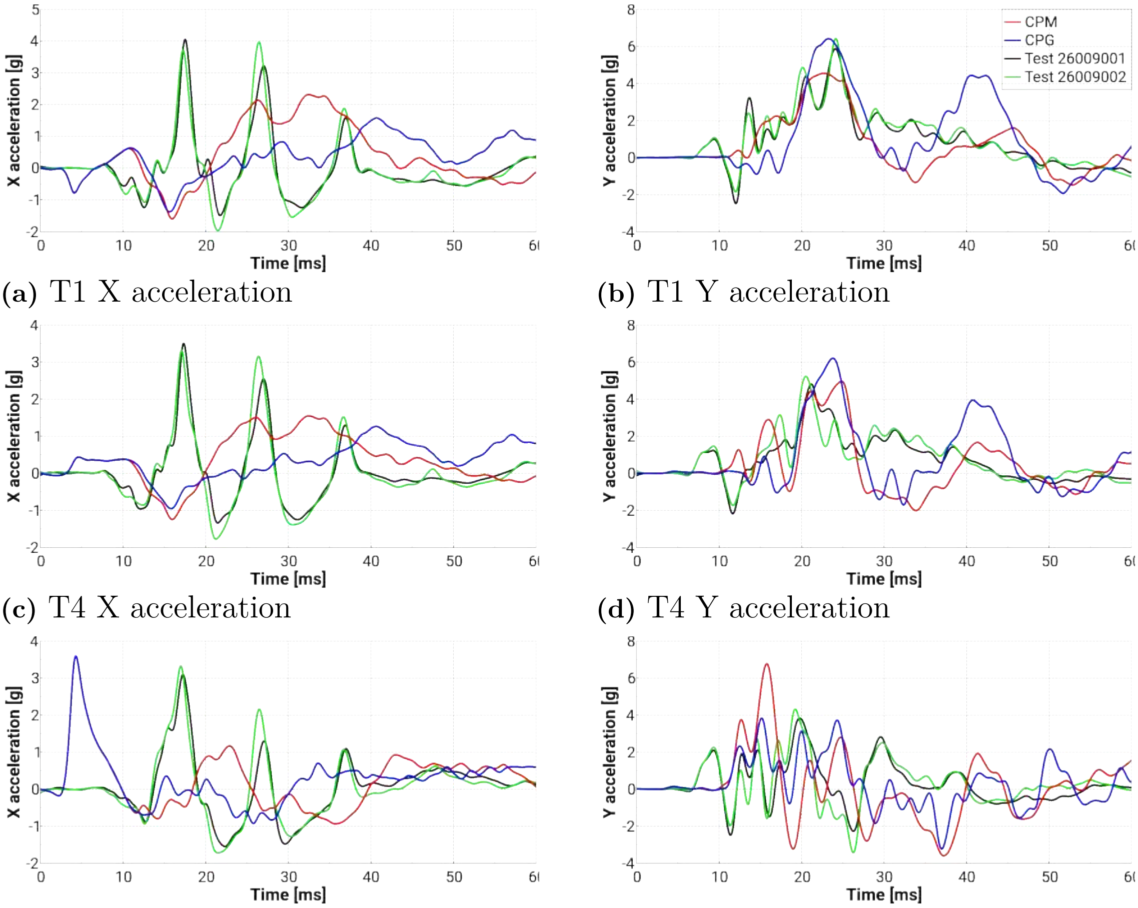

(a) T1 X acceleration
(b) T1 Y acceleration
(c) T4 X acceleration
(d) T4 Y acceleration
(e) T12 X acceleration
(f) T12 Y acceleration

Figure 4.16: WorldSID-50M 120 mm thoracic acceleration responses

Table 4.12: Numerical thoracic acceleration results for the WorldSID-50M 120 mm case.

Metric [g]	$\bar{x}_{\text{test}}$	x_{CPM}	x_{CPG}	$\lvert\Delta_{\text{CPM}}\rvert$	$\lvert\Delta_{\text{CPG}}\rvert$	**Closest**
T1 X acc.	4.01	2.32	1.58	1.69	2.43	CPM
T1 Y acc.	6.14	4.55	6.41	1.60	0.27	CPG
T4 X acc.	3.40	1.55	1.27	1.86	2.14	CPM
T4 Y acc.	5.02	4.96	6.20	0.06	1.18	CPM
T12 X acc.	3.21	3.59	3.59	0.38	0.38	Equal
T12 Y acc.	4.08	6.77	3.84	2.69	0.24	CPG
$E_{m,F}$	–	–	–	1.38	1.11	CPG
I_F: **CPG mean improvement over CPM = 19.7%**						

4.2.5.3 Test Case 6: Pelvic Responses

The pelvic acceleration responses for the SID-IIs full-arm driver-position 120 mm case do not show converging agreement in the X- and Z-directions. However, the

Y-direction response shows partial agreement, where the transition from negative to positive acceleration is captured to some extent when disregarding the oscillatory behaviour observed in the physical tests.

The pelvic X- and Z-direction accelerations also appear to include the influence of the seat-squash phase at approximately 4 ms. This is reflected in Table 4.13, where the X-, Z- and magnitude responses dominate the mean absolute difference. CPM gives the slightly lower mean absolute difference for the evaluated pelvic response family in this case.

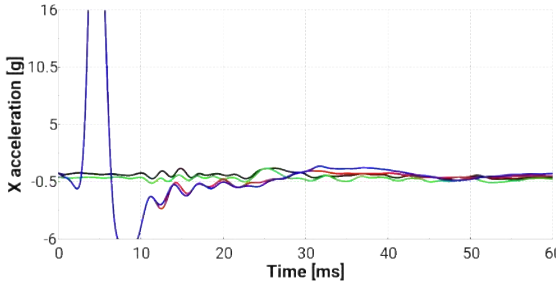

(a) Pelvis X acceleration

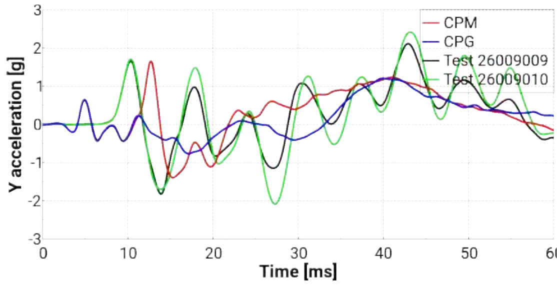

(b) Pelvis Y acceleration

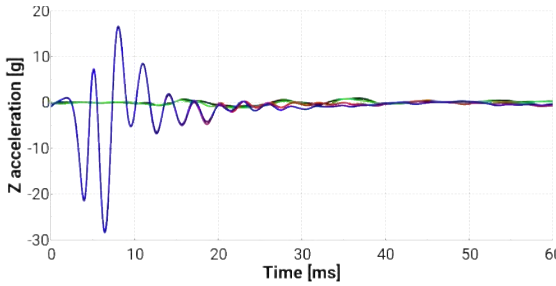

(c) Pelvis Z acceleration

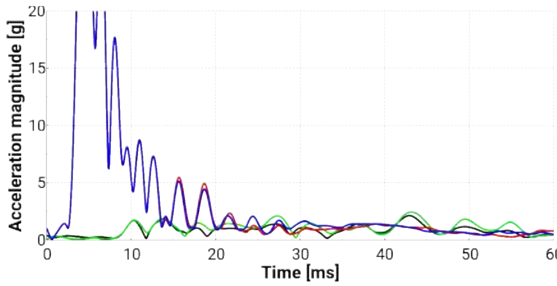

(d) Pelvis acceleration magnitude

Figure 4.17: Pelvic acceleration responses for the SID-IIs full-arm driver-position 120 mm case.

Table 4.13: Signed peak pelvic acceleration results for the SID-IIs full-arm driver-position 120 mm case.

Metric [g]	$\bar{x}_{\text{test}}$	x_{CPM}	x_{CPG}	$\lvert\Delta_{\text{CPM}}\rvert$	$\lvert\Delta_{\text{CPG}}\rvert$	Closest
Pelvis X acc.	0.78	37.27	37.22	36.49	36.43	CPG
Pelvis Y acc.	2.26	1.65	1.20	0.62	1.06	CPM
Pelvis Z acc.	-0.11	-28.38	-28.40	28.27	28.29	CPM
Pelvis acc. magnitude	2.27	38.64	38.56	36.37	36.29	CPG
$E_{m,F}$	–	–	–	25.43	25.52	CPM
I_F: **CPM mean improvement over CPG = 0.3%**						

4.3 Computational Time Comparison

The computational-time comparison was performed to evaluate the additional solver cost introduced by CPG relative to CPM. The results are presented at two levels. First, a standalone airbag-only comparison was used to isolate the computational cost associated with the gas formulation itself. Second, the applied simplified rig simulations were evaluated to assess how this increased cost translates to complete airbag–occupant interaction test cases.

4.3.1 Stand-alone Airbag-Only Comparison

The computational-time metrics from the standalone airbag-only comparison are presented in Table 4.14. This comparison was based on the simplified airbag-only setup described in Section 3.4.2, where both simulations were run using the same airbag definition and simulation time.

Table 4.14: Computational-time comparison between CPM and CPG for the airbag-only setup.

Setup	Wall-clock time			Clock zone-cycle [ns]		Gas CPU share [%]	
	CPM	CPG	Factor	CPM	CPG	CPM	CPG
Airbag only	00:18:35	05:49:43	18.8	127.117	2406.371	56.63	97.18

Wall-clock time is reported as h:min:s. The factor is calculated as CPG wall-clock time divided by CPM wall-clock time. Both standalone simulations were run using 192 MPP cores.

The standalone airbag-only results show that CPG requires substantially higher computational time than CPM. The wall-clock time increases from 1115 s for CPM to 20983 s for CPG, corresponding to an increase by approximately a factor of 19. A similar increase is observed for the clock zone-cycle time, where CPG requires approximately 2406 ns compared with approximately 127 ns for CPM. This indicates that each solver iteration at the zone-cycle level is considerably more computationally expensive when using CPG. The solver timing output also shows that the gas formulation accounts for 97.18% of the CPU usage for CPG, whereas the corresponding contribution for CPM is approximately 57%. Thus, the increased computational cost in the standalone airbag-only setup is primarily associated with the CPG gas formulation.

4.3.2 Simplified Rig Comparison

The computational-time results from the applied simplified rig simulations are presented in Table 4.15. These simulations include the complete airbag–occupant interaction setup for the evaluated test cases and therefore represent the computational cost of the methods in the applied validation environment.

Table 4.15: Computational-time comparison between CPM and CPG for the evaluated simplified rig simulations.

Test no.	Wall-clock time CPM	Wall-clock time CPG	Factor	Clock zone-cycle [ns] CPM	Clock zone-cycle [ns] CPG	Gas CPU share [%] CPM	Gas CPU share [%] CPG
1	11:59:59	69:37:01	5.80	74.549	326.804	9.23	75.63
2	09:45:52	35:36:19	3.65	74.123	304.927	9.24	75.89
3	02:57:43	29:42:33	10.03	47.500	477.178	23.86	91.58
4	02:52:47	29:38:51	10.30	46.180	476.185	23.95	91.97
5	03:33:34	24:25:17	6.86	39.090	268.610	23.58	90.59
6	03:30:25	29:54:01	8.53	38.509	328.861	23.63	90.44
7	02:52:12	30:20:05	10.57	35.967	389.240	21.96	90.14
8	02:44:43	30:54:58	11.26	35.302	398.060	22.04	90.33

Wall-clock time is reported as h:min:s. The factor is calculated as CPG wall-clock time divided by CPM wall-clock time. All simplified rig simulations were run using 128 MPP cores. The CPG simulation for Test 1 was run with `TSSFAC=0.5`.

The applied simplified rig simulations show the same overall trend as the standalone airbag-only comparison. CPG requires longer runtime than CPM for all evaluated test cases. However, the direct comparison for Test 1 should be interpreted with caution, since the CPG simulation was run with `TSSFAC=0.5` instead of `TSSFAC=0.67`. This reduced the timestep and therefore increased the computational time for that specific simulation. Since this setting was only applied to CPG and not to CPM, the Test 1 runtime factor is less suitable for direct CPM–CPG comparison than the remaining test cases.

The average values reported here are calculated using all eight simulations for each gas method, including Test 1. The average CPM runtime is 18129.4 s, corresponding to approximately 5 h 2 min 9 s, while the average CPG runtime is 126068.1 s, corresponding to approximately 35 h 1 min 8 s. Based on the full set of simulations, CPG therefore requires 3-11 times longer wall-clock runtime than CPM on average. Since the average includes the non-identical timestep setting used for the CPG simulation in Test 1, this value should be regarded as an aggregate result for the evaluated simulation set rather than a fully balanced method-to-method comparison.

5 Discussion

This chapter discusses the main findings from the results chapter and the factors that may have influenced their interpretation. The discussion addresses deviations between physical tests and CAE simulations, differences between CPM and CPG, the trade-off between computational time and model fidelity, and the main limitations and uncertainties of the study.

5.1 Physical Tests Compared with CAE Simulations

A possible cause of the deviations between the two physical tests conducted for each test case is the manual modification of the airbag during pressure probe installation and natural variation in the airbag production. As described in Section 3.3.1.2, pressure probes were inserted into each SAB. This procedure may have introduced variation, since the installation was performed on a limited number of components and was partly dependent on manual handling. Possible sources of variation include the insertion depth of the probe, changes to the airbag folding, and damage to the tape during installation.

Another factor that may have affected repeatability is the limited level of detail in the test instructions provided to the VCC test team, as described in Section 3.3.1. For example, no angular measurements were specified for the neck or head orientation, including the head angle relative to the shoulder or upper torso. In addition, no detailed information was provided for leg placement, and only basic measurements were used for ATD positioning. These limitations may have allowed small differences in the initial test setup, which can also be observed in the visual results through variations in dummy position and motion sequence.

The observed spread between the repeated physical tests also affects how the CAE results should be interpreted. If the two physical tests show noticeable differences, the physical average should not be interpreted as a single deterministic reference response. Instead, it should be regarded as an indication of the expected experimental variation. In such cases, it is more relevant to evaluate whether the CAE response follows the same general trend and remains within a reasonable range of the physical tests, rather than requiring an exact match to one individual test curve. This is especially important for qualitative assessments, where deployment path, arm motion, and local airbag deformation may be influenced by small variations in the initial setup.

A further difference between physical testing and CAE is related to the airbag pressure response. As shown in Section 4.2.2, the virtual simulations generally show higher airbag pressure peaks compared with the physical tests. One possible explanation is that pressure is obtained differently in the two environments. In the physical tests, pressure is measured locally using a pressure probe positioned close to the inflator nozzle, as described in Section 3.3.1.2. In CAE, the pressure represents an averaged numerical pressure quantity based on the gas method used in the simulation, as described in Sections 2.3.3 and 2.3.4. The physical and numerical pressure signals therefore do not represent identical measurement conditions. This is particularly relevant during the early deployment phase, where local flow effects near the inflator may influence the physical sensor response more strongly than the averaged numerical pressure response. If the same measurement conditions were applied on both CAE models as for the physical test, a more correlating result could possibly have been obtained.

Another deviation between the physical tests and the CAE simulations is related to the full-arm ATD configuration. In CAE, the Humanetics Hybrid III 05f ATD was used for the full-arm analysis, while the physical tests used a SID-IIs ATD with a full-arm attachment, as described in Sections 3.3.2.1 and 3.3.1.1. This difference is believed to have contributed to the deviations observed in the full-arm moment results. This is especially evident in Figure 4.11, where the upper arm X moment shows opposite polarity. The same behaviour is reflected in the visual snapshot results presented in Figure 4.9, where the elbow rotation in CAE is clockwise, while the corresponding physical test shows counter-clockwise elbow rotation. The Hybrid III ATD also included a right arm, whereas the SID-IIs ATD did not have an arm on the right side. This difference affects the centre of gravity of the Hybrid III ATD relative to the SID-IIs ATD. The differences in proportions and mass properties described in Section 2.4 are therefore likely to have affected the test conditions and the resulting arm response.

A further numerical deviation is related to the lower body response. The dummy positioning and preloading procedure using seat-squashing, described in Section 2.4.5, appears to influence the initial response of the lower thorax and pelvic region. Initial spikes in X and Y accelerations can be observed for both T12 and pelvis at approximately 4 ms. This is visible in Sections 4.2.5.2 and 4.2.5.3, and is also a recurring trend in the combined plots in Appendix D. These initial spikes likely influenced the absolute amplitude peaks and should therefore be considered when interpreting the numerical results.

5.2 Comparison Between CPG and CPM

The pressure response suggests that the relative performance of CPM and CPG depends on the deployment phase rather than one method being consistently more accurate. CPG appears to provide a more representative post-peak response, while

CPM better follows the later pressure decay. Since the early deployment phase is where a large part of the airbag loading is developed, the improved post-peak pressure behaviour of CPG may also help explain its closer qualitative agreement in arm trajectory. Therefore, the pressure response should be interpreted in relation to specific phases of the deployment, rather than as a single overall measure of method performance.

The unfolding behaviour represents one of the clearest qualitative differences between CPG and CPM in this project. In the evaluated early deployment sequence, CPG showed closer visual agreement with the physical tests in terms of local folding, crease formation, lower-region development, and overall deployment path. CPM captured the general deployment sequence, but the airbag shape appeared smoother and more rounded in several of the evaluated time steps. This suggests that CPG may provide a more representative description of the early deployment phase, where local gas transport and fabric motion have a strong influence on the resulting airbag geometry.

This observation is consistent with previous CPG studies. Usta et al. [27] reported that CPG improved the unfolding kinematics and filling behaviour compared with CPM in generic airbag configurations with internal chambers and tethers. Similarly, Ohira et al. [23] showed that CPG was able to reproduce gas flow behaviour in narrow regions and capture gas rebound effects that were less apparent in CPM. These findings support the interpretation that the continuum-based formulation of CPG can be beneficial in the early deployment phase, particularly when the airbag behaviour is governed by local flow paths, chamber filling, and interaction between the gas and fabric.

The arm response also shows differences between the two gas methods. Based on the conducted testing, the majority of the CPM simulations show excessive arm movement compared with CPG and the physical tests. This is particularly visible for the half-arm cases, for example when reviewing the final arm angle of the WorldSID-50M ATD in Figure 4.5. Although CPG also shows excessive behaviour in some cases compared to CPM, such as in Test Case 5 presented in Section 4.2.4.3. One possible reason could be the difference in initial airbag pressure during the critical deployment phase.

For the full-arm dummy cases, it is less valid to determine which method is closer to the physical tests based only on the upper-arm and forearm moment metrics, since different dummy configurations were used in physical testing and CAE. However, the mean absolute arm moment difference indicates that CPM provides a 14 percent improvement over CPG when comparing both upper-arm and forearm moment for all cases against the physical test average.

5.3 Computational Time Versus Added Model Fidelity

Based on the computational resources presented in Section 4.3, CPG should not be described as the superior model solely because it shows comparatively better results in arm trajectory, airbag pressure, and occupant injury metrics. These improvements must be weighed against the increased computational time. The numerical results indicate an improvement in accuracy for CPG compared to CPM, while the computational cost of the simplified test case simulations was between 3–11 times higher for CPG and around 19 times higher in the stand-alone comparison. This creates a clear trade-off between accuracy and cost, since cost is directly influenced by computational time. The suitability of CPG must therefore be evaluated based on the intended application and the level of accuracy required.

A similar trade-off has previously been discussed for airbag simulations in Out-of-Position (OoP) cases. Ruff et al. [25] compared the Uniform Pressure Method with the ALE method and highlighted that simplified pressure-based approaches are less suitable for the first milliseconds of deployment, when the occupant may already interact with the airbag before it is fully inflated. Although the ALE approach increased the runtime from approximately 6 hours to 90 hours, it was still considered relevant because it provided a more accurate representation of the early deployment phase.

This supports the interpretation that a more computationally expensive gas modelling method may be justified when the early deployment behaviour is critical for the safety assessment. In the context of the present study, CPG should therefore not necessarily replace CPM in all airbag simulations. Instead, the two methods should be viewed as complementary. CPM remains advantageous for computationally efficient simulations and larger parameter studies, whereas CPG may be more suitable for selected cases where higher modelling fidelity is required, such as early airbag development or OoP scenarios where local gas-flow effects and early airbag–occupant interaction have a stronger influence on the response.

5.4 Limitations and Uncertainties

Several limitations of this study are related to the physical test setup, the CAE setup, and the comparison between them. One important limitation is that only two physical tests were conducted for each test case. This limited the statistical basis for evaluating repeatability and defining a representative physical reference. In cases where noticeable test spread was present between the two physical tests, it became difficult to determine what the CAE model should be expected to match.

Another limitation is the lack of detailed measurements, camera rig settings, and other specifications linking the physical testing and CAE setup. More accurate measurements of the physical test setup would likely have improved the comparison and reduced the test spread. Better knowledge of the exact camera positions, FOV settings, and lighting conditions would also have improved the visual comparison between the physical tests and CAE simulations.

The simplified static rigid-seat test setup also limits how directly the results can be transferred to a full vehicle environment. The setup is not representative of a complete vehicle cabin or a moving vehicle structure during a real crash. However, for the purpose of this thesis, where the focus is on airbag–arm interaction and the comparison between CPM and CPG, the rigid-seat static test rig provides an indication of the relevant interaction behaviour.

The CPG tuning procedure also introduces uncertainty. The CPM model used in this project was provided by VCC as an already correlated reference model, meaning that several modelling parameters and assumptions had previously been adjusted to reproduce relevant physical test behaviour. In contrast, the CPG model was implemented and tuned within the scope of this project using the linear impactor setup. The objective was to obtain reasonable agreement with the correlated CPM reference model, rather than to directly correlate CPG against physical test data.

Consequently, tuning CPG towards a correlated CPM through the linear impactor setup does not imply that the CPG model is fully correlated with physical testing. Under more ideal conditions, the CPG model should have been correlated directly against physical test data in the same way as the CPM model. Therefore, the comparison in this project should be interpreted as a comparison between an established and correlated CPM model and a newly implemented CPG model with limited tuning, rather than as a fully equivalent comparison between two independently validated gas modelling methods. CPG is still at an early stage of development in LS-DYNA, with limited possibilities for parameter tuning. However, the relatively high accuracy observed for the lightly tuned CPG model from several evaluation perspectives indicates that further development and more method-specific tuning could potentially improve its accuracy even further.

6 Conclusion

The CPG model used in this study was, due to project-related constraints, only lightly tuned. Nevertheless, CPG generally showed improved agreement compared with CPM. For example, CPG predicted the arm trajectory more accurately in the investigated simplified test-rig cases and showed better agreement with the physical tests in the numerical occupant injury results. In addition, CPG showed stronger predictive capability during the critical early deployment phase, where local gas dynamics strongly influence the airbag response. In this phase, CPG was able to reproduce the geometrical shape, creasing, and unfolding behaviour of the physical tests more closely than CPM, which showed larger deviations in some aspects.

However, this improvement is associated with a clear computational trade-off. CPG required substantially longer computational time than CPM, which raises the question of whether the increased computational cost is justified for all applications. Instead, CPG may be most suitable for selected cases, such as detailed SAB development phases where early deployment behaviour is of particular importance. Another potential approach could be to combine the two methods, using CPG during the critical early deployment phase and CPM during less critical stages of the simulation. OoP testing represents one potential application area where these aspects may be of particular relevance, where the early interaction between airbag and occupant is difficult to predict.

In conclusion, CPG should currently be regarded as a complement to CPM for selected applications rather than as a direct replacement. CPM remains a viable alternative when runtime and computational efficiency are prioritized, such as in standardized virtual simulations. In contrast, CPG may be more suitable for applications where detailed early deployment behaviour and local gas dynamics are important.

7

Future Work

Several areas for future work were identified based on the limitations and findings of this study. A first recommendation is to perform future full-arm ATD comparisons using equivalent arm setups in both physical testing and CAE. In this project, the physical tests were conducted using a SID-IIs ATD with a custom full-arm attachment, while the CAE model used a Hybrid III dummy with a full-arm representation. This introduced differences in arm proportions, mass distribution, and joint behaviour, which complicated the interpretation of the arm moment and arm trajectory results. Using equivalent physical and virtual full-arm configurations would provide a more robust basis for comparing CPM and CPG in terms of occupant interaction.

Further work should also focus on direct calibration of the CPG model against physical test data. This would make it possible to evaluate the method under more equivalent conditions and reduce the uncertainty associated with tuning CPG towards a CPM-based reference response.

Future investigations should evaluate strategies for reducing the computational cost of CPG. This could include improvements in solver efficiency, optimization of CPG parameter settings, or alternative simulation strategies such as, model switching, which is not currently available. In such an approach, CPG could potentially be used during the critical early unfolding and airbag–occupant interaction phase, while CPM or a simpler constant pressure model could be used during less critical parts of the simulation. This may improve the balance between model fidelity and computational cost, although further validation would be required.

Future studies should also improve the correspondence between the physical test setup and the CAE model. More detailed documentation of the physical test conditions, including ATD positioning, angular measurements, camera positions, field-of-view settings, lighting conditions, and boundary conditions, would improve the repeatability of the physical tests and the comparability with CAE. One potential improvement is the plexiglass wall. Although the project used deformable material behaviour and realistic boundary conditions, differences in deformation behaviour remained between the physical tests and CAE. Further refinement of the plexiglass model, including its deformation pattern and dynamic response, could improve the agreement between simulations and physical tests.

The physical test reference should also be expanded in future work. Since only two physical tests were conducted for each test case, it was sometimes difficult to determine whether deviations were caused by the CAE model or by test variation. Additional repetitions would provide a clearer estimate of physical test spread, expected behaviour and make it possible to define a more robust validation reference for the CAE results.

Future work should consider applying the CPG method in more realistic vehicle-related environments. The present study was conducted using a simplified static rigid-seat test setup, which was suitable for isolating the airbag–occupant interaction but does not fully represent the complexity of a vehicle interior. Further investigations using a more detailed component-based seat model, including foam, fabric, seams, and more realistic seat deformation, would provide a better understanding of CPG performance in more representative side-impact applications. Such a model would also enable further evaluation of how CPM and CPG behave during seam tear and the subsequent airbag deployment through the seat structure. Finally, the comparison should also be extended to a dynamic full-scale vehicle model to evaluate how the gas modelling methods are affected under more realistic crash conditions.

Bibliography

[1] *Ansys ls-dyna keyword user's manual, volume i*, LS-DYNA Dev, master@79685cced, 03/12/26, ANSYS, Inc., 2026.

[2] Ansys, Inc. "LS-DYNA: Time integration." LS-DYNA knowledge-base article, Accessed: Jun. 1, 2026. [Online]. Available: `https://lsdyna.ansys.com/time-integration-2/`.

[3] Ansys, Inc. "Explicit dynamics theory guide: Time integration." Ansys Explicit Dynamics Analysis Guide, Release 2024 R2, Accessed: Jun. 1, 2026. [Online]. Available: `https://ansyshelp.ansys.com/public/Views/Secured/corp/v242/en/exd_ag/exp_dyn_theory_time_int.html`.

[4] Autoliv Inc. "Inflators & initiators." Manufacturer specifications for airbag inflators, Accessed: Apr. 9, 2026. [Online]. Available: `https://www.autoliv.com/safety-solutions/inflators-initiators`.

[5] K. M. Balavich, N. R. Soderborg, R. C. Lange, and H. Pearce, "Deployment characteristics of seat mounted side impact airbags," in *Proceedings of the 22nd International Technical Conference on the Enhanced Safety of Vehicles*, Paper No. 11-0358; TRID Accession No. 01366511, Washington, DC, USA, 2011. Accessed: Jun. 1, 2026. [Online]. Available: `https://trid.trb.org/View/1366511`.

[6] M. Brown. "Safety for every body in occupant protection," Humanetics, Accessed: Apr. 21, 2026. [Online]. Available: `https://www.humaneticsgroup.com/perspectives/safety-every-body-occupant-protection`.

[7] A. Hirth, A. Haufe, and L. Olovsson, "Airbag simulation with ls-dyna: Past – present – future," in *6th European LS-DYNA Users' Conference*, Daimler-Chrysler AG; Dynamore GmbH; IMPETUS Afea AB, 2003.

[8] Humanetics Innovative Solutions, *User manual: Sid-iis small side impact dummy (sbl d)*, 180-9900 User Manual SID-IIs (SBL D), Rev H, Humanetics Innovative Solutions, 2015. Accessed: Jun. 1, 2026. [Online]. Available: `https://www.humaneticsgroup.com/sites/default/files/2020-11/um-sid-iis-sbl-d.pdf`.

[9] Humanetics Innovative Solutions, *Hybrid III 5th Female*, `https://www.humaneticsgroup.com/products/anthropomorphic-test-devices/frontal-impact/hybrid-iii-5th-female`, Accessed: 2026-05-28, 2026.

[10] Humanetics Innovative Solutions. "Sid-iis (side impact dummy)," Accessed: Apr. 9, 2026. [Online]. Available: `https://www.humaneticsgroup.com/products/anthropomorphic-test-devices/side-impact/sid-iis`.

[11] Humanetics Innovative Solutions. "Virtual crash tests & models," Accessed: Jun. 1, 2026. [Online]. Available: https://www.humaneticsgroup.com/products/virtual-models.

[12] Humanetics Innovative Solutions. "W-sid50s (side impact dummy)," Accessed: Apr. 9, 2026. [Online]. Available: https://www.humaneticsgroup.com/products/anthropomorphic-test-devices/side-impact/worldsid-50m.

[13] Humanetics Innovative Solutions, *Sid-iis small side impact dummy: Technical product sheet*, Technical Product Sheet 2012, Humanetics Innovative Solutions. [Online]. Available: https://www.humaneticsgroup.com/sites/default/files/2020-06/sid-iis-tps.pdf.

[14] Insurance Institute for Highway Safety, *Side impact crashworthiness evaluation 2.0: Rating guidelines*, Version IV, April 2024, Insurance Institute for Highway Safety, 2024. Accessed: Jun. 1, 2026. [Online]. Available: https://www.iihs.org/media/d87f7873-a584-473c-9f23-1c14788b7335/G19jBw/Ratings/Protocols/current/side_impact_2.0_rating_guidelines.pdf.

[15] T. B. Khalil and M. Y. Sheh, "Vehicle crashworthiness and occupant protection in frontal impact by fe analysis: An integrated approach," in *Crashworthiness of Transportation Systems: Structural Impact and Occupant Protection*, ser. NATO ASI Series, J. A. C. Ambrósio, M. F. O. S. Pereira, and F. P. da Silva, Eds., vol. 332, Dordrecht: Springer, 1997, pp. 363–399. DOI: 10.1007/978-94-011-5796-4_15.

[16] A. Leledakis, "Heterogeneity in car occupant safety: Using numerical simulations to address real-world safety," Chalmers full-text version, Doctoral thesis, Chalmers University of Technology, Gothenburg, Sweden, 2024, ISBN: 978-91-7905-986-6. [Online]. Available: https://research.chalmers.se/publication/539494/file/539494_Fulltext.pdf.

[17] A. Leledakis, J. Östh, J. Iraeus, J. Davidsson, and L. Jakobsson, "The influence of occupant's size, shape and seat adjustment in frontal and side impacts," in *Conference Proceedings International Research Council on the Biomechanics of Injury, IRCOBI*, Chalmers full-text version, vol. 2022-September, Porto, Portugal, 2022, pp. 549–584. [Online]. Available: https://research.chalmers.se/publication/532579/file/532579_Fulltext.pdf.

[18] C.-H. Lin, Y.-P. Cheng, and J. Wang, "Evaluation of ls-dyna corpuscular particle method for side impact airbag deployment applications," in *13th International LS-DYNA Users Conference, Session: Fluid Structure Interaction*, General Motors; LSTC, 2014.

[19] S. Mattern, *Overview on airbag-modeling possibilities in ls-dyna*, https://lsdyna.ansys.com/wp-content/uploads/2025/02/201009_dynamore-express__airbag-modeling.pdf, DYNAmore Express Webinar Presentation, accessed June 2, 2026, DYNAmore GmbH, 2020.

[20] National Highway Traffic Safety Administration. "49 CFR Part 572 – Anthropomorphic Test Devices." Electronic Code of Federal Regulations, Title 49, Chapter V, Part 572, Electronic Code of Federal Regulations, Accessed: Jun. 1, 2026. [Online]. Available: https://www.ecfr.gov/current/title-49/subtitle-B/chapter-V/part-572.

[21] R. Nayak, R. Padhye, K. Sinnappoo, L. Arnold, and B. K. Behera, "Airbags," *Textile Progress*, vol. 45, no. 4, pp. 209–301, 2013. DOI: 10.1080/00405167.2013.859435.

[22] Oasys Ltd, *Dummy positioning using ls-dyna*, Oasys PRIMER 20.1 Documentation, Accessed: 2026-05-20, 2023. [Online]. Available: https://help.oasys-software.com/articles/#!primer-20-1/dummy-positioning-using-ls-dyna.

[23] H. Ohira et al., "Preliminary validation of new continuum-based particle gas (cpg) method for airbag deployment simulations," in *JSOL / Toyota / Arup Collaborative Technical Report*, Conference/technical paper, 2024.

[24] L. Porkolab and I. Lakatos, "Possibilities for further development of the airbags in the case of non-conventional seating positions," *Periodica Polytechnica Transportation Engineering*, vol. 53, no. 2, pp. 146–157, 2025. DOI: 10.3311/PPtr.38633.

[25] C. Ruff, A. Eichberger, and T. Jost, "Simulation of an airbag deployment in out-of-position situation," in *Proceedings of the 5th LS-DYNA Anwenderforum*, Passive Sicherheit I, Ulm, Germany: DYNAmore GmbH, 2006, J-I-5–J-I-16. Accessed: Jun. 11, 2026. [Online]. Available: https://lsdyna.ansys.com/wp-content/uploads/2025/02/simulation-of-an-airbag-deployment-in-out-of.pdf.

[26] S. Schneider et al., "Effectiveness of thorax & pelvis side airbag for improved side-impact protection," in *Proceedings of the 19th International Technical Conference on the Enhanced Safety of Vehicles*, Paper No. 05-0273; TRID Accession No. 815296, Washington, DC, USA, 2005. Accessed: Jun. 1, 2026. [Online]. Available: https://trid.trb.org/View/815296.

[27] E. Usta et al., "Testing and verification of the new cpg method for complex internal structures in airbags," in *2025 Ansys EMEA Transportation Summit and LS-DYNA Conference*, DYNAmore GmbH; Ansys Inc.; Toyoda Gosei Europe NV; BMW AG, Munich, Germany, 2025.

[28] *Virtual far side simulation & assessment protocol, version 1.0*, Implementation 2024. Version 1.0, published 18 May 2023., Euro NCAP, Brussels, Belgium, 2023.

[29] Volvo Car Corporation. "Volvo ex90 support: Side airbags," Accessed: Apr. 9, 2026. [Online]. Available: https://www.volvocars.com/mt/support/car/ex90/25w46/article/47d2c97fd33effd3c0a8cc3718c999b7-dc8d1323d325cb39c0a8cc3741
8664b2fa77a7e089c0a8296870d1a409/47d2c97fd33effd3c0a8cc3718c999b7-bbd2d0ead3267338c0a8cc37502ab65b-8664b2fa77a7e089c0a8296870d1a409/47d2c97fd33effd3c0a8cc3718c999b7-03d2b0fed326ca44c0a8cc3723b9d353-8664b2fa77a7e089c0a8296870d1a409/.

[30] C. M. Wai, A. Rivai, and O. Bapokutty, "Modelling optimization involving different types of elements in finite element analysis," *IOP Conference Series: Materials Science and Engineering*, vol. 50, p. 012 036, 2013. DOI: 10.1088/1757-899X/50/1/012036.

[31] E. Yreux, J. Wang, I. Caldichoury, and M. M. Atif, "Continuum-based particle gas (cpg): A new approach for airbag deployment simulations," in *2024 International LS-DYNA Conference*, Ansys Inc., 2024.

A

Front view snapshots & Arm Trajectory observations

Appendix A I – WSID50 – 80 mm and 120 mm test cases.

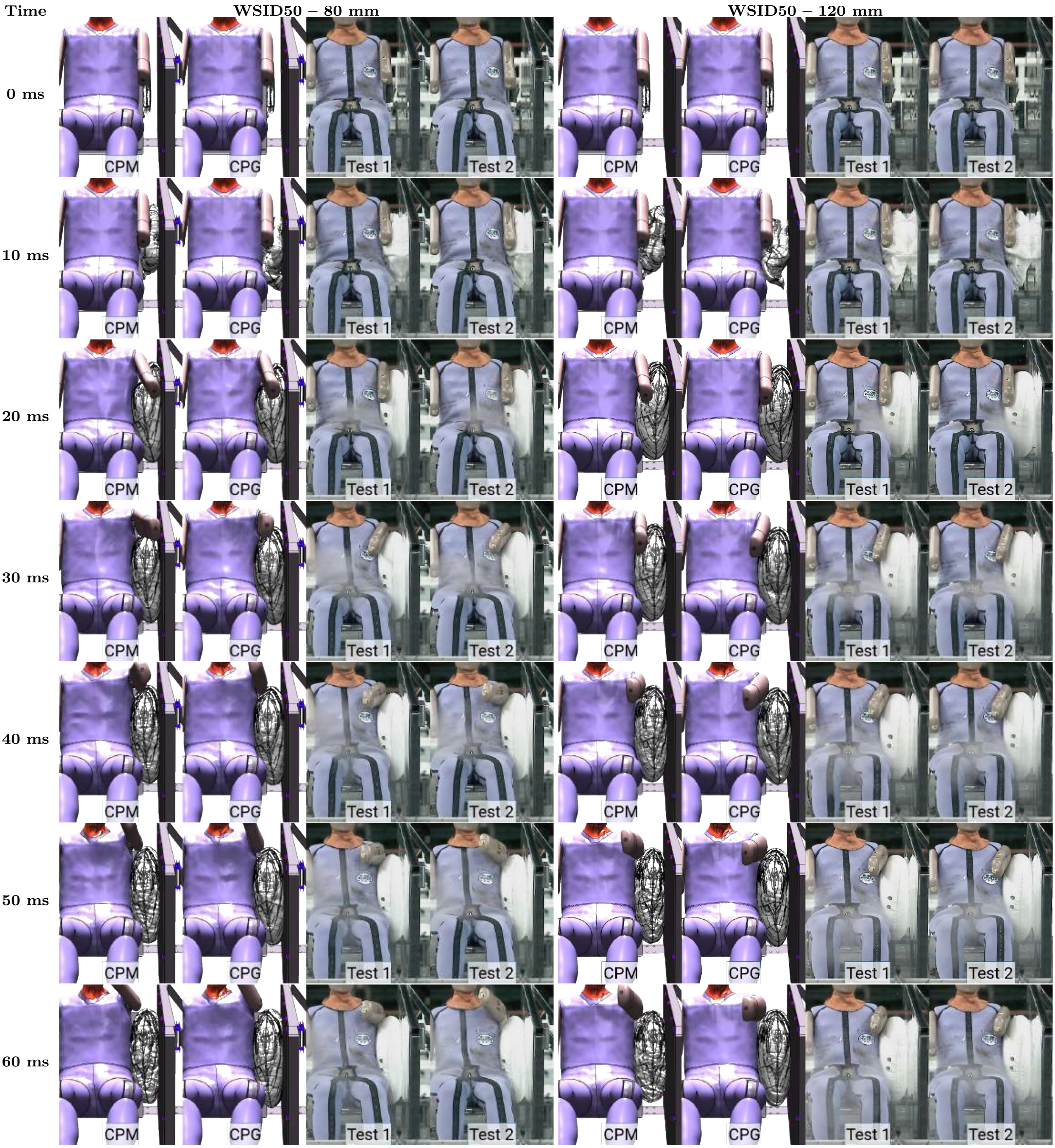

Table A.1: Summary of qualitative arm-trajectory observations for the WSID50 80 mm and 120 mm test cases.

Time	Main observation	CPM–CPG comparison
Test Case 1: WorldSID-50 – 80 mm		
20 ms	Both tests show the airbag below the arm; Test 2 has a slightly larger inward arm angle.	CPM shows more airbag intrusion between body and arm than CPG.
30 ms	Similar arm height in both tests; Test 2 shows a larger inward arm angle.	Both methods place the arm higher than the physical tests.
40 ms	Similar inward arm angle in both tests; Test 1 has a lower XZ-plane arm angle.	CPG captures the inward angle better, but both methods place the arm too high.
50 ms	Test 1 reaches shoulder level; Test 2 reaches neck level. Both show inward rotation.	Both methods show a higher arm trajectory than the physical tests.
60 ms	Test 1 is near neck level; Test 2 is near chin level. Both retain inward rotation.	Both methods capture inward rotation, but the arm trajectory remains too high.
Test Case 2: WorldSID-50 – 120 mm		
20 ms	Continued lateral expansion with similar arm motion in both tests.	CPG remains closer to the physical arm–airbag alignment.
30 ms	Increasing arm rotation with consistent behaviour between the tests.	Both methods capture the trend, but CPM shows a larger arm-angle deviation.
40 ms	Continued arm rotation with consistent global trajectory.	Both methods place the arm too high; CPG shows closer overall agreement.
50 ms	The arm reaches a higher position with inward motion toward the body.	Both methods deviate in arm height, but CPG follows the trajectory trend better.
60 ms	Similar final inward arm angle and arm position in both tests.	Both capture inward rotation; CPG gives a closer final arm position.

Appendix A II – SID-IIs – 80 mm and 120 mm test cases.

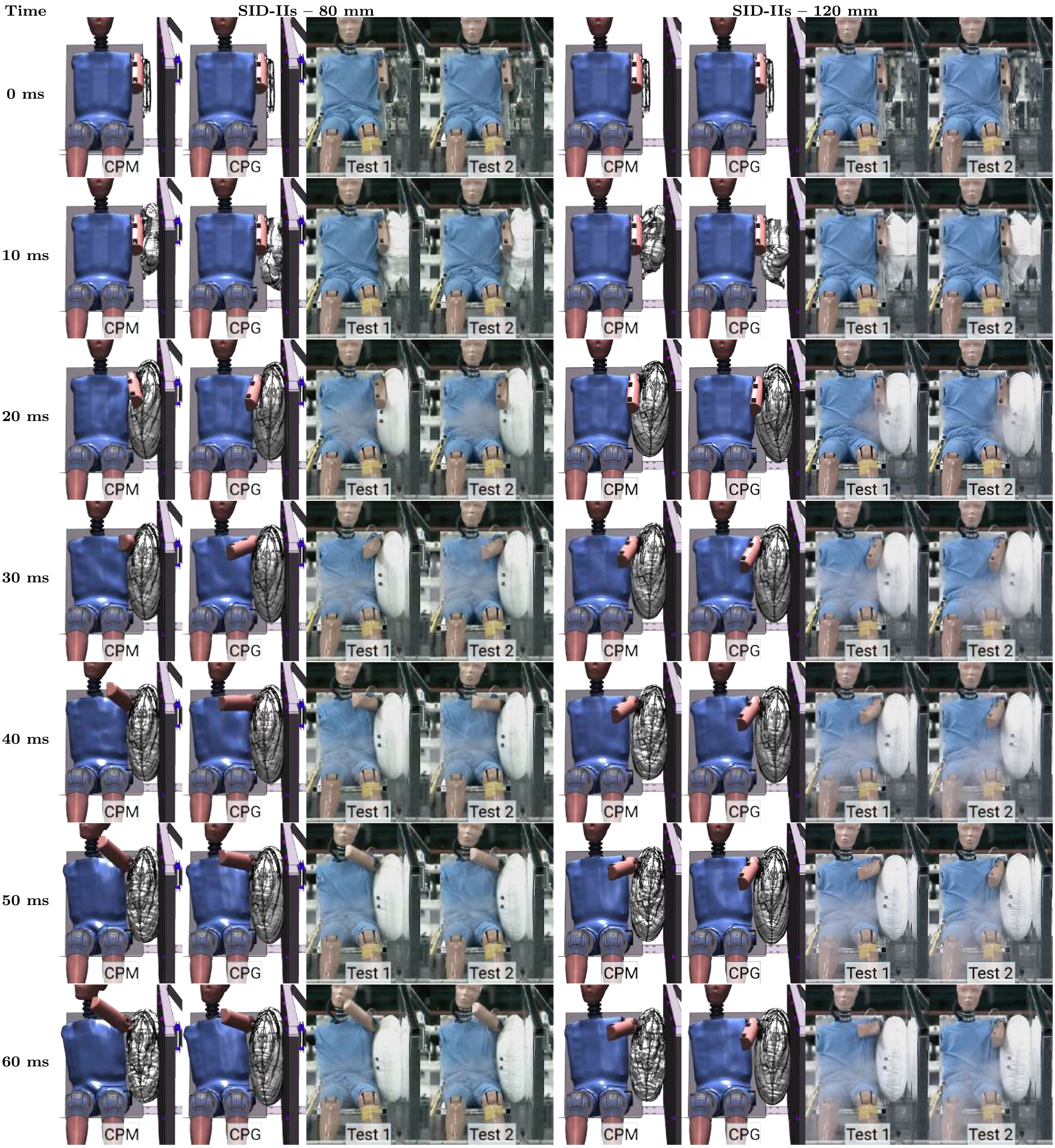

Table A.2: Summary of qualitative arm-trajectory observations for the SID-IIs 80 mm and 120 mm test cases.

Time	Main observation	CPM–CPG comparison
Test Case 3: SID-IIs – 80 mm		
20 ms	Similar early arm motion in both tests, with an initial upward component.	CPM shows a more outward response; CPG shows a more inward response.
30 ms	Similar arm height in both tests; Test 2 has a larger inward arm angle.	CPM is closer to Test 1; CPG is closer to Test 2.
40 ms	Similar arm height in both tests; Test 2 shows a stronger inward angle.	CPG agrees better, especially with Test 2. CPM places the arm higher.
50 ms	Both tests show an upward and inward arm trajectory.	CPG captures the inward angle well but is slightly lower; CPM is higher.
60 ms	Good repeatability with an upward and inward final arm trajectory.	CPM is closer at this timestep; CPG remains slightly lower.
Test Case 4: SID-IIs – 120 mm		
20 ms	Early outward arm displacement, with variation between the tests.	CPM is closer to Test 1; CPG is closer to Test 2.
30 ms	Continued outward arm rotation as the airbag expands.	Both methods capture the trend but follow different physical-test responses.
40 ms	Continued arm rotation, with Test 1 and Test 2 differing in arm angle.	CPM is closer to Test 1; CPG is closer to Test 2.
50 ms	Variation remains in the final arm position and angle.	Both methods show reasonable agreement, with no clear preference.
60 ms	Final arm position differs between the tests, but both show inward arm angle.	CPM is closer to Test 1; CPG is closer to Test 2.

Appendix A III – SID-IIs full arm driver position 80 mm and 120 mm test cases.

Table A.3: Summary of qualitative arm-trajectory observations for the SID-IIs full arm driver position 80 mm and 120 mm test cases.

Time	Main visual observation	CPM–CPG comparison
Test Case 5: SID-IIs, full arm, driver position – 80 mm		
20 ms	Different steering wheel grip positions and arm alignment relative to the SAB are observed between the physical tests.	Both CAE methods show similar positioning.
30 ms	The physical tests are similar, with the palm pushed into the steering wheel.	Both CAE methods are similar, but the thumb is pushed into the steering wheel.
40 ms	The palm is pushed into the steering wheel, while the fingers begin to release.	The hand begins to release in both CAE methods.
50 ms	The hand is released, with Test 1 showing a lower position than Test 2.	Both CAE methods are similar, but the hand release differs from the physical tests.
60 ms	The hand is pushed away from the steering wheel.	Both methods are similar, although an unnatural hand angle is observed.
Test Case 6: SID-IIs, full arm, driver position – 120 mm		
20 ms	Different hand positions are observed, while the arm alignment is similar.	Identical initial conditions make both CAE methods identical.
30 ms	No distinct change from the previous timestep is observed.	No distinct change from the previous timestep is observed.
40 ms	The elbow moves inward, while the hand moves away from the steering wheel with a clockwise moment.	Both CAE methods show similar motion, but with opposite hand moment compared to the physical tests.
50 ms	The elbow moves inward, while the hand moves outward.	The elbow motion is captured, but the hand also moves inward.
60 ms	The elbow moves further inward, and the hand is released from the steering wheel.	The elbow motion is captured, but the hand also rotates inward.

Appendix A IV – SID-IIs full arm relaxed position 80 mm and 120 mm test cases.

Table A.4: Summary of qualitative arm-trajectory observations for the SID-IIs full arm relaxed position 80 mm and 120 mm test cases.

Time	Main visual observation	CPM–CPG comparison
Test Case 7: SID-IIs, full arm, relaxed position – 80 mm		
20 ms	Test 1 and test 2 show different initial airbag–arm positioning.	Both CAE methods are visually closer to test 2, with the airbag behind the arm.
30 ms	Test 1 shows mainly lateral motion, while test 2 shows initial arm lift.	Both CAE methods follow the upward arm motion observed in test 2.
40 ms	Test 2 shows clearer arm lift, while test 1 remains more laterally displaced.	Both CAE methods reproduce the arm lift, but the motion appears slightly advanced.
50 ms	Test 2 shows the arm moving upward and slightly inward.	Both CAE methods overpredict the arm lift and outward rotation.
60 ms	Test 1 shows moderate lift, while test 2 reaches approximately chest height.	Both CAE methods show larger arm motion than the physical tests.
Test Case 8: SID-IIs, full arm, relaxed position – 120 mm		
20 ms	Both physical tests show similar initial airbag–arm contact.	Both CAE methods show comparable initial interaction, with slight positioning differences.
30 ms	The physical tests show initial lateral arm loading.	Both CAE methods show lateral loading, with additional upward motion.
40 ms	The arm is lifted diagonally in both physical tests.	Both CAE methods capture the diagonal motion, but appear slightly ahead.
50 ms	The physical tests show continued diagonal arm lift.	Both CAE methods show a higher and more extended arm position.
60 ms	The arm remains partly flexed in the physical tests.	Both CAE methods overpredict the final arm displacement and extension.

B
Left-hand-side view snapshots

Appendix B I – WSID50 80 mm and 120 mm test cases.

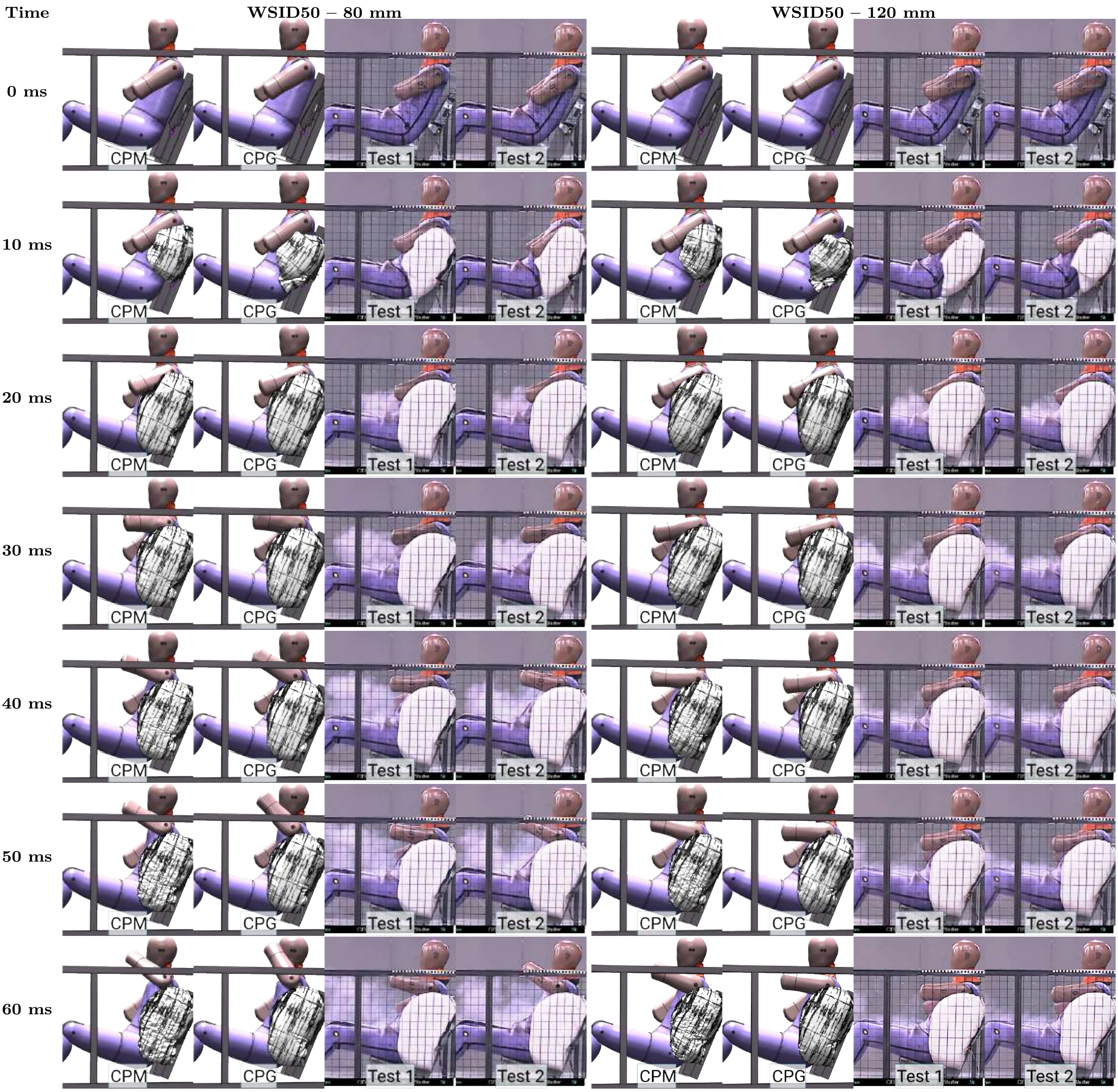

Appendix B II – SID-IIs 80 mm and 120 mm test cases.

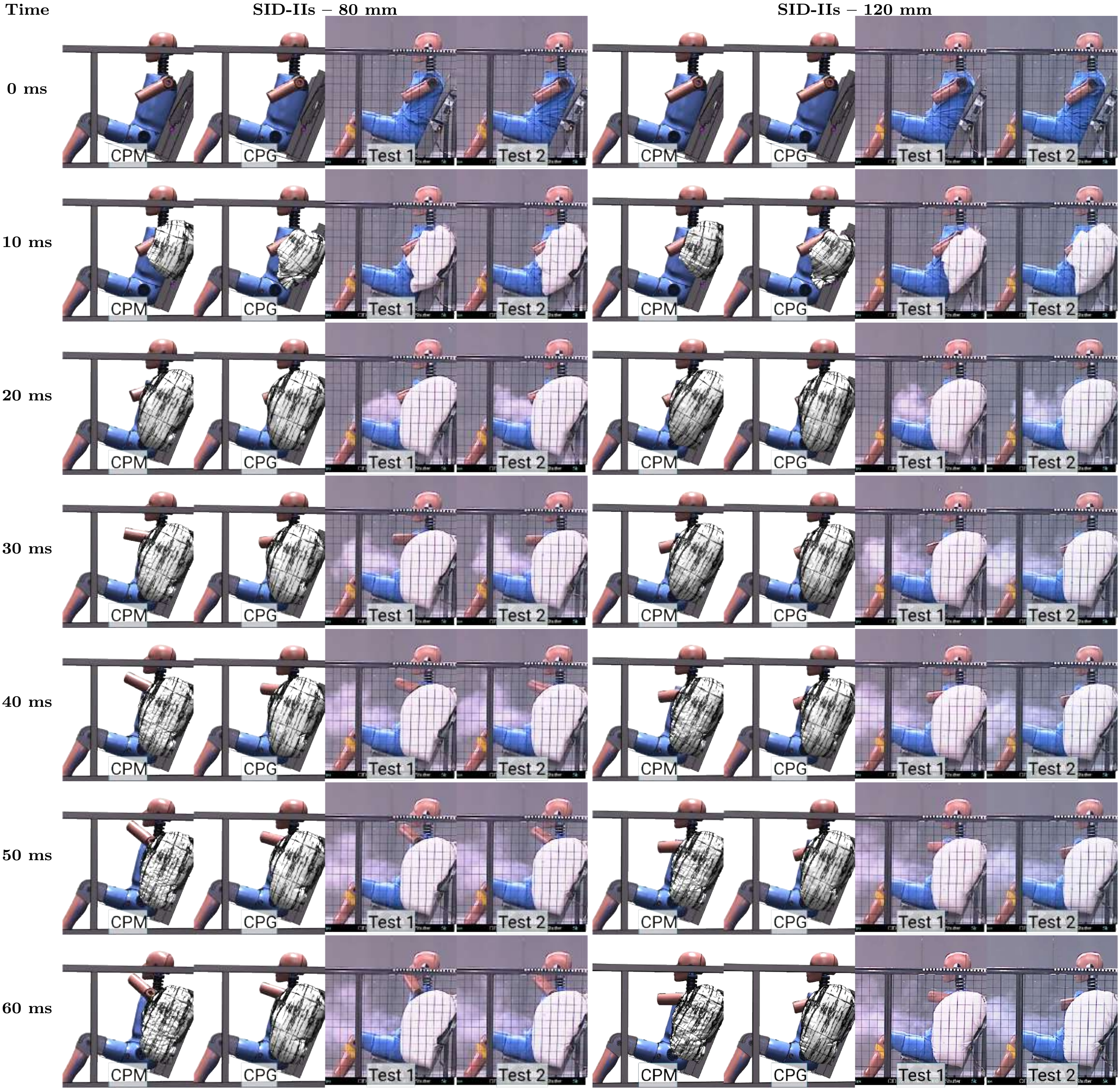

Appendix B III – SID-IIs full arm driver position 80 mm and 120 mm test cases.

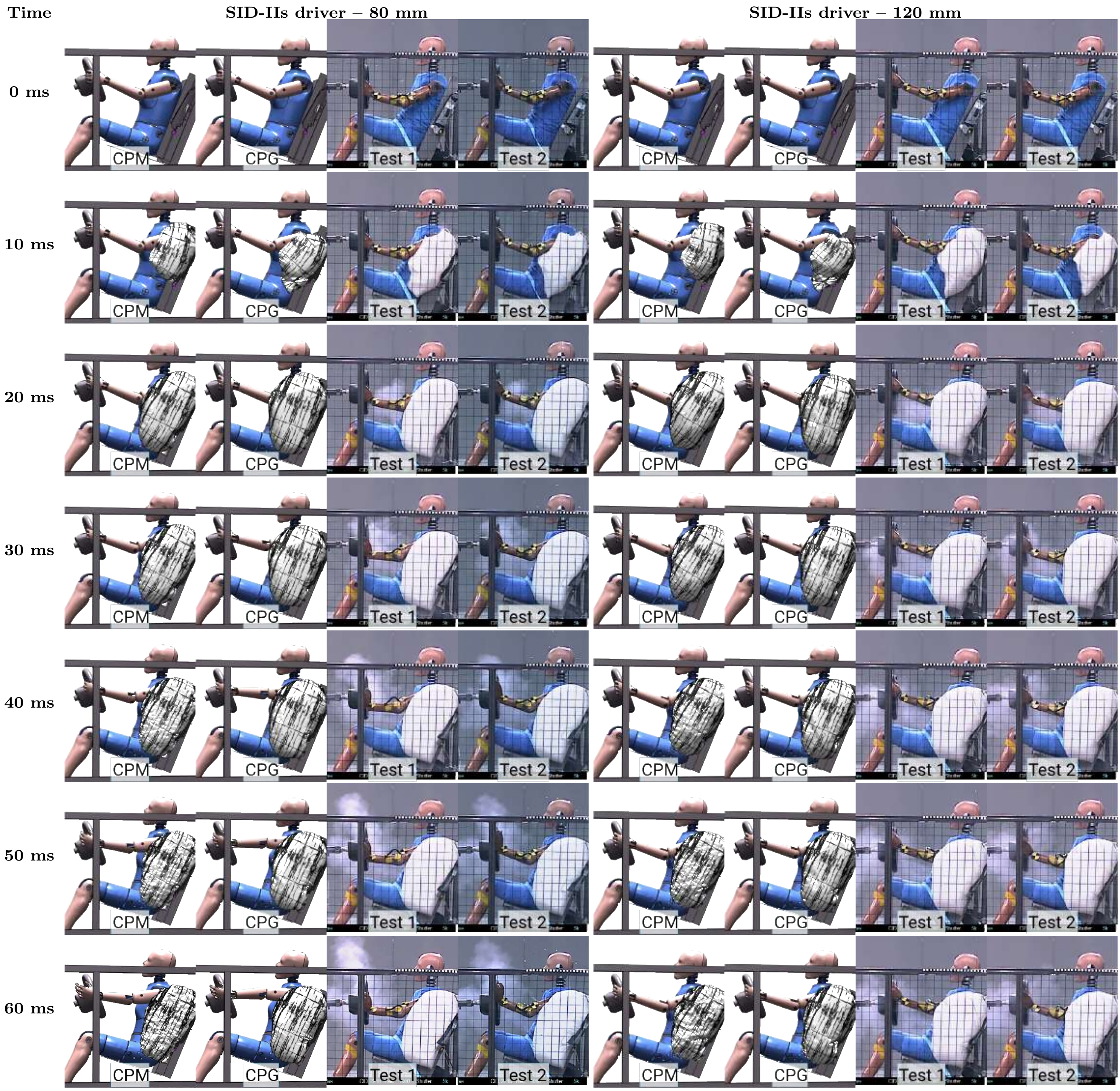

Appendix B IV – SID-IIs full arm relaxed position 80 mm and 120 mm test cases.

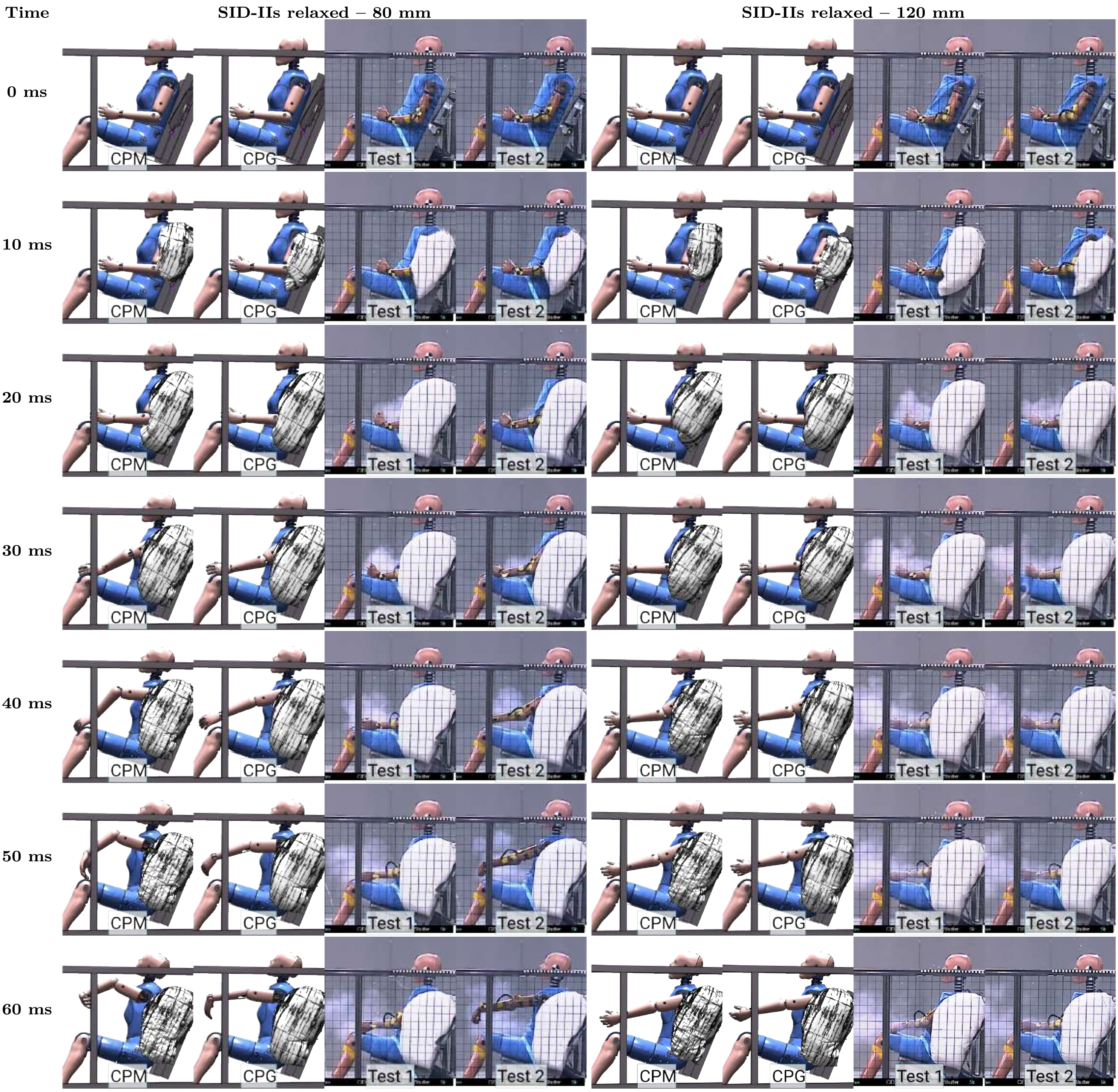

C
Detailed Unfolding Snapshots

Appendix C I – WSID50 80 mm and 120 mm test cases.

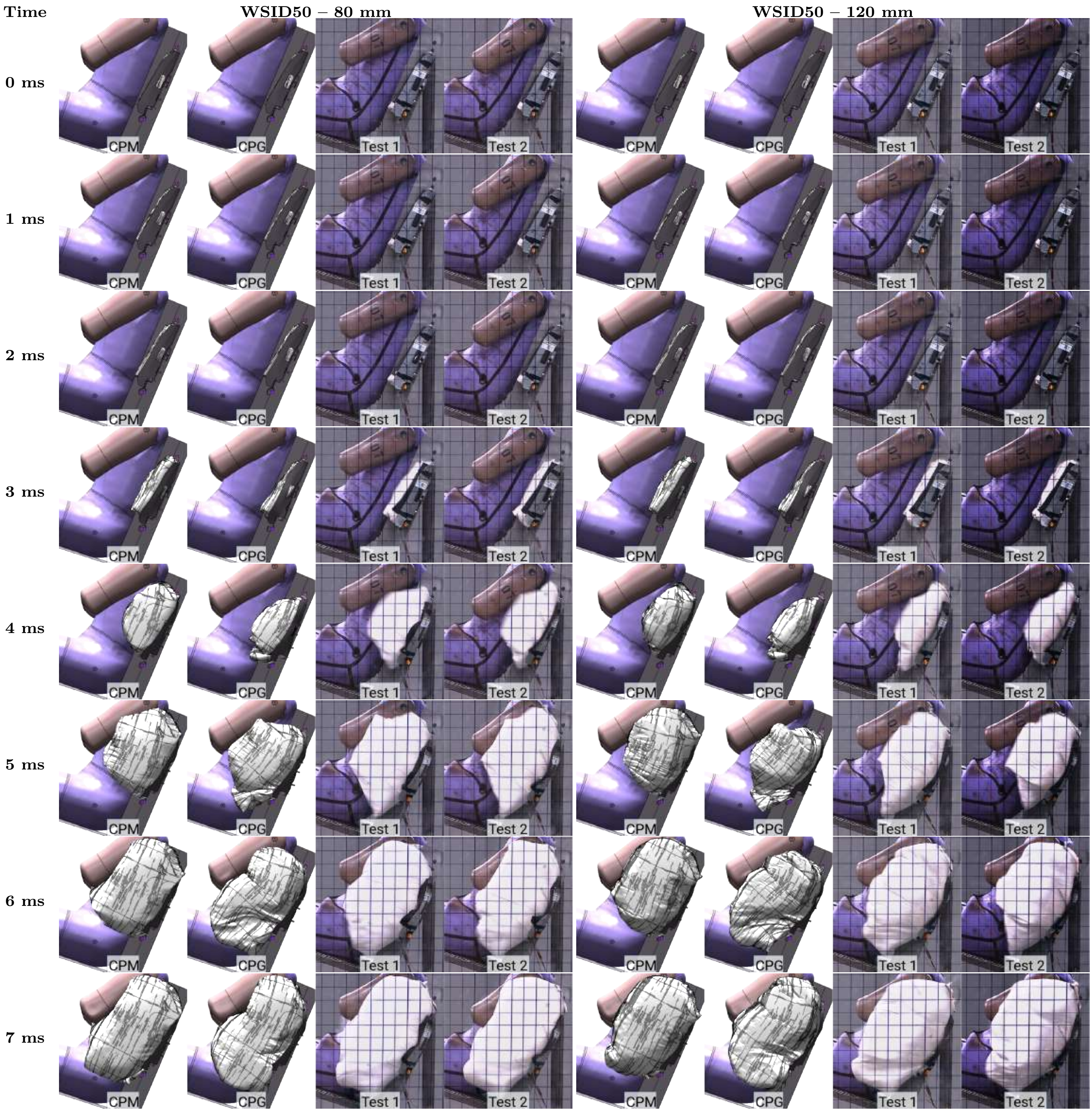

Appendix C II – SIDIIS 80 mm and 120 mm test cases.

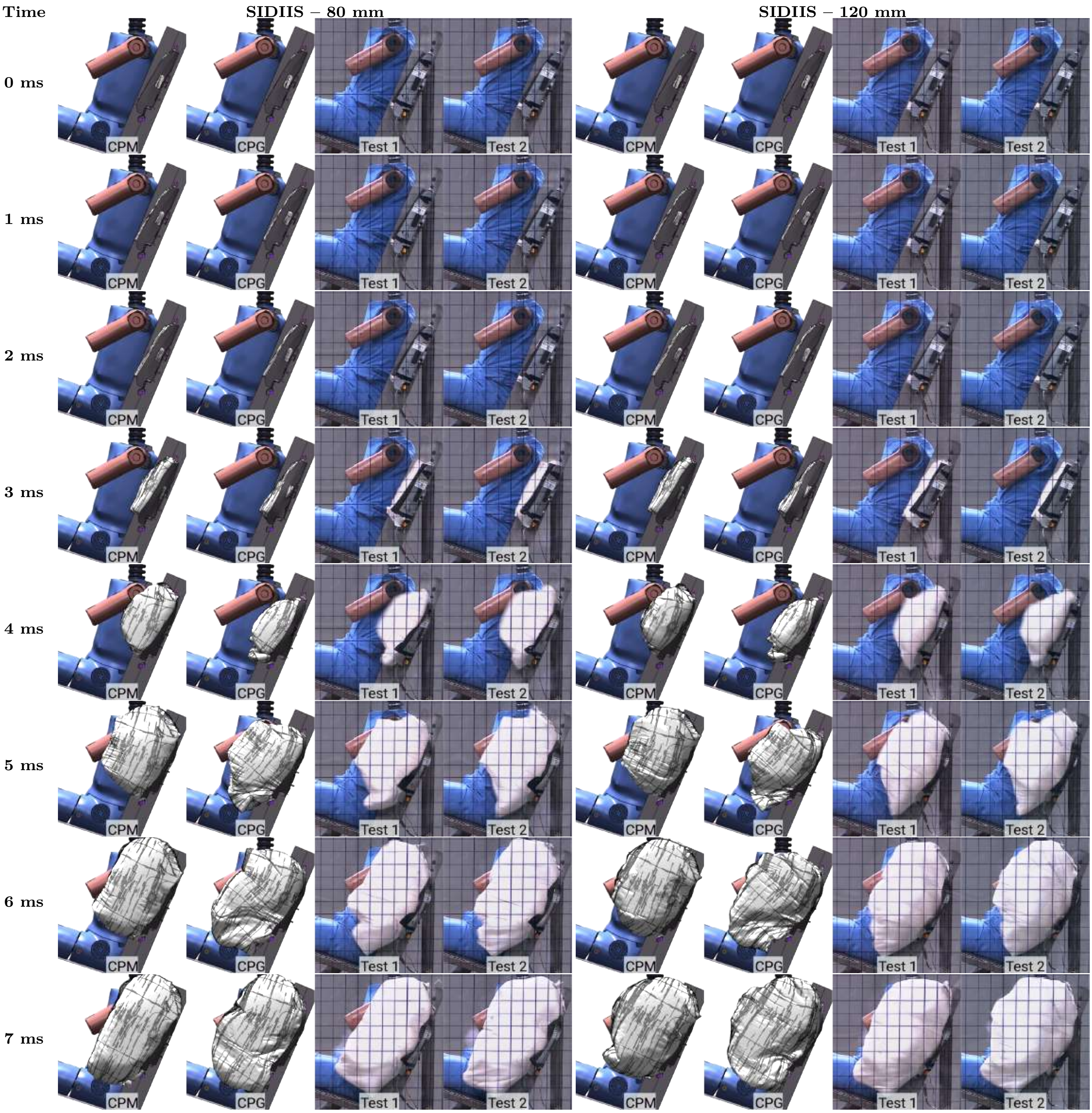

Appendix C III – SIDIIS full arm driver position 80 mm and 120 mm test cases.

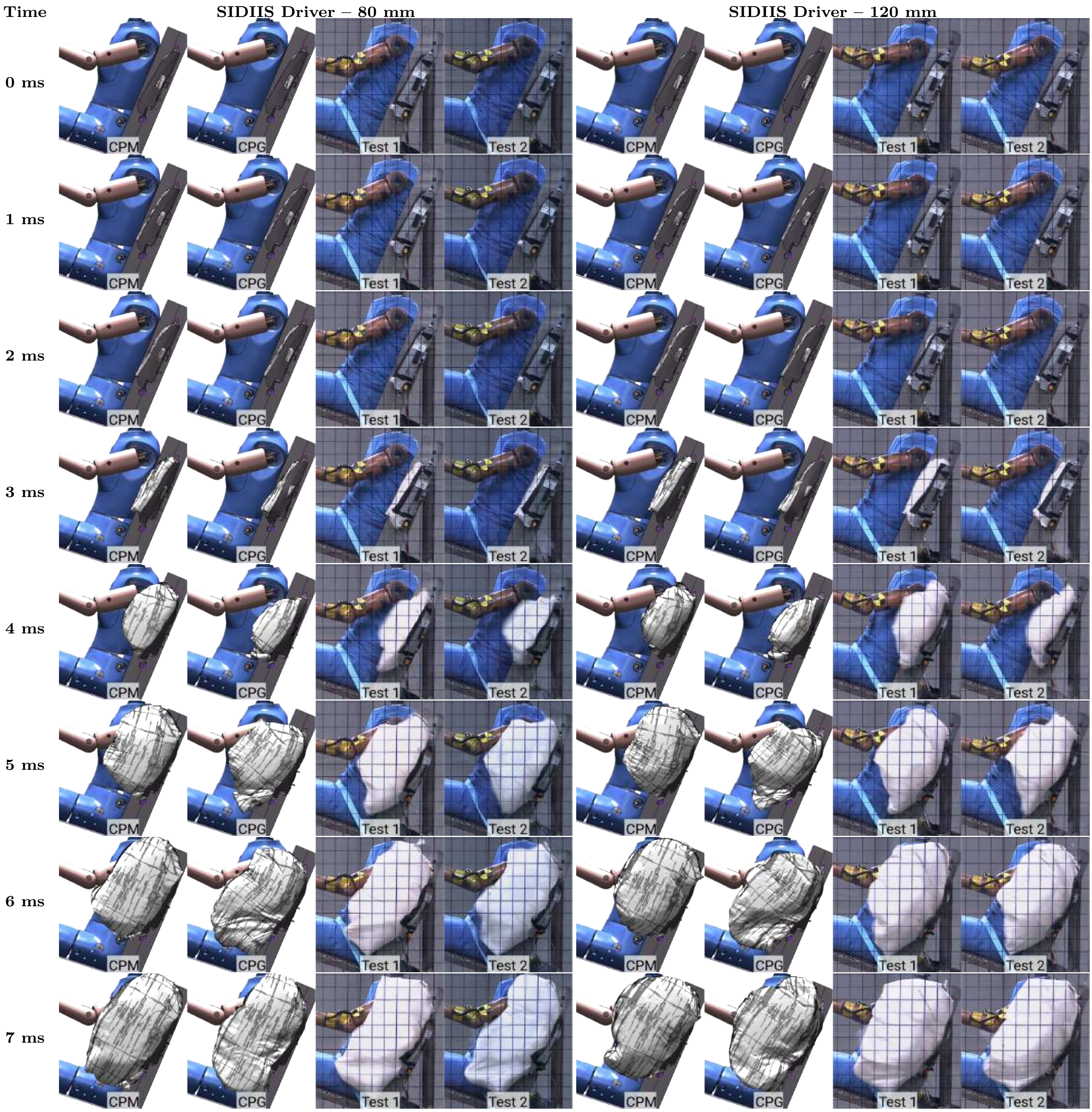

Appendix C IV – SIDIIS full arm relaxed position 80 mm and 120 mm test cases.

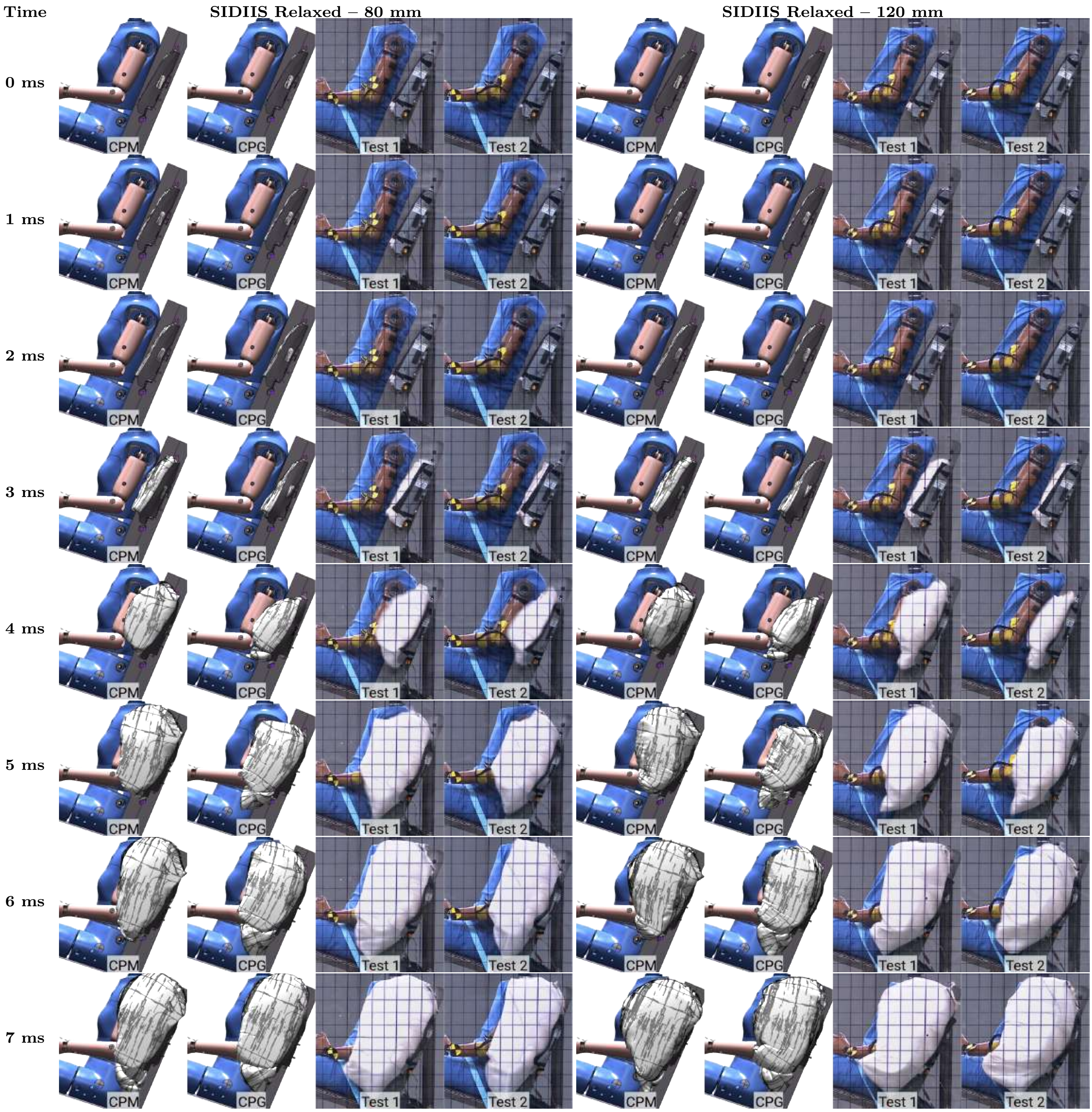

D
Occupant Injury Criteria Plots

Appendix D I – WSID50 120 mm

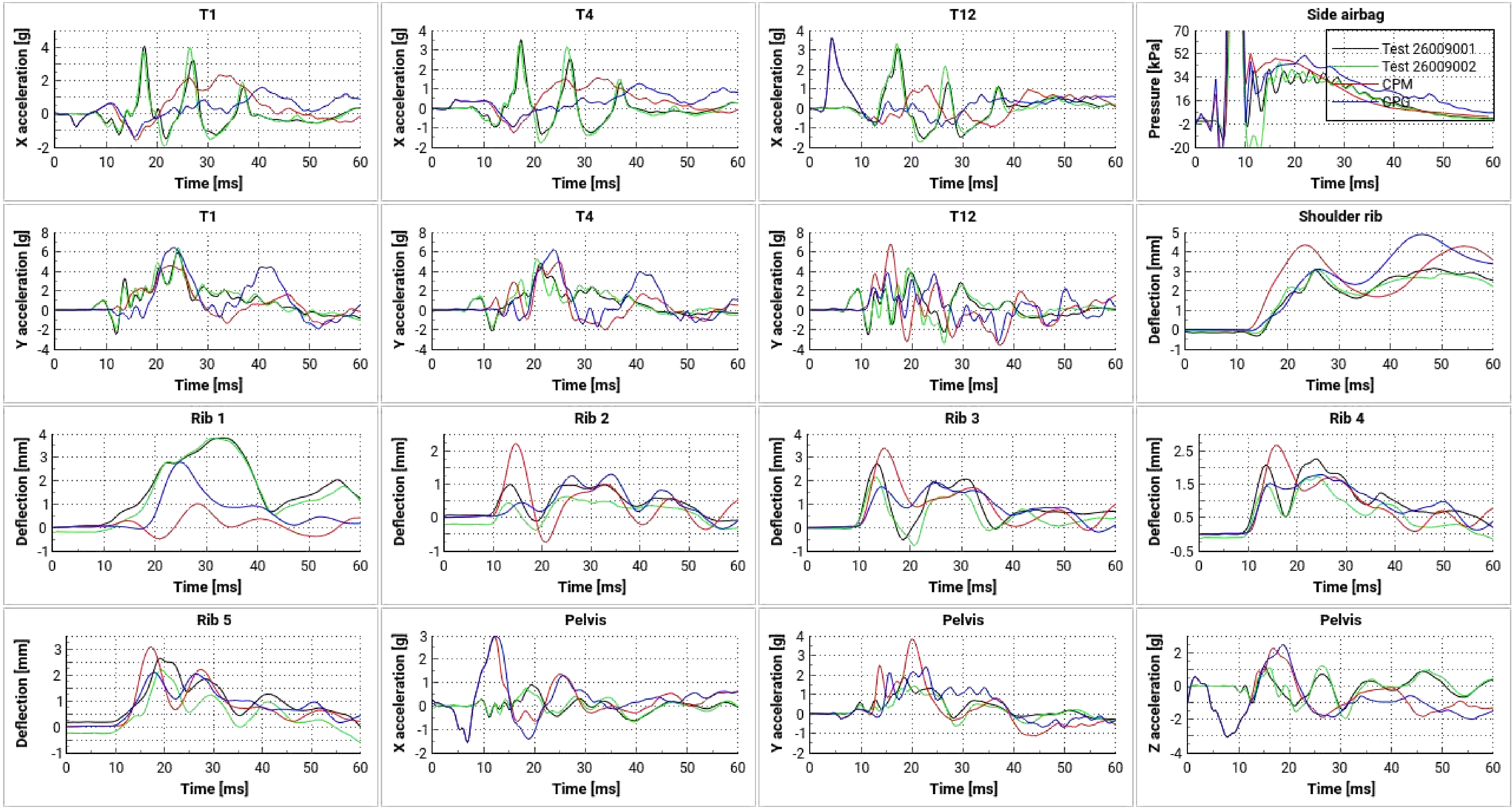

Appendix D II – WSID50 80 mm

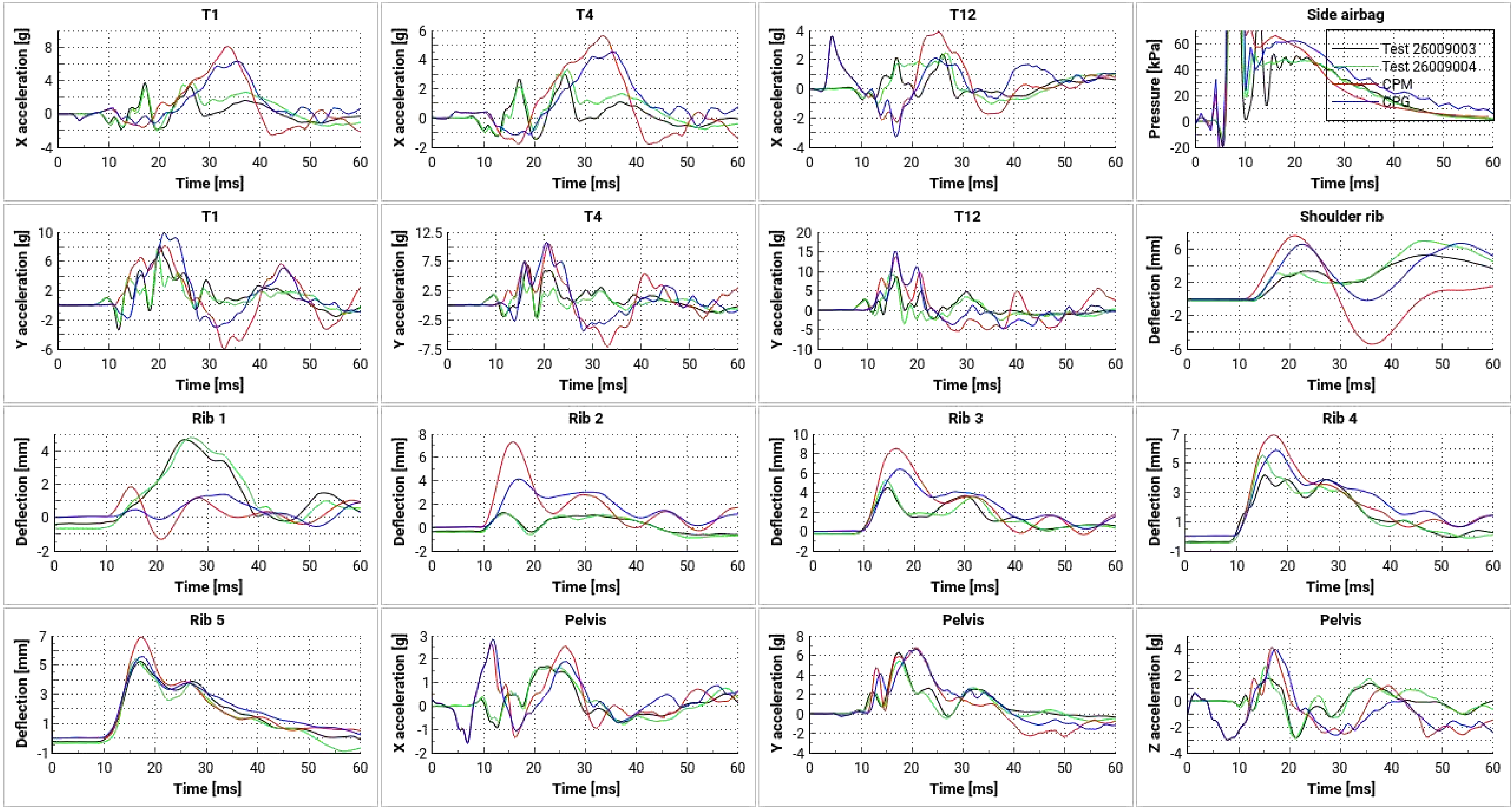

Appendix D III – SID-IIs 80 mm

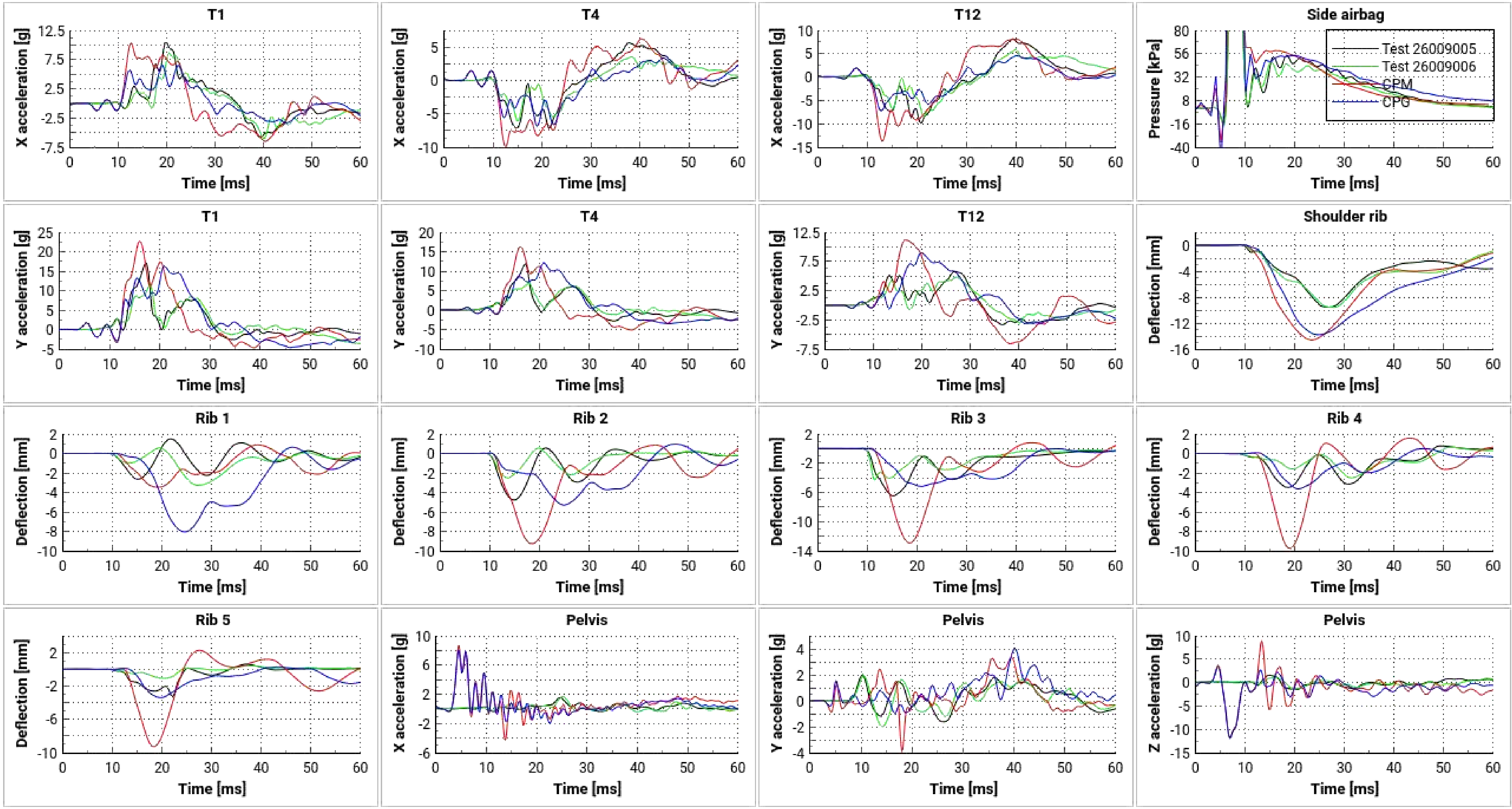

Appendix D IV – SID-IIs 120 mm

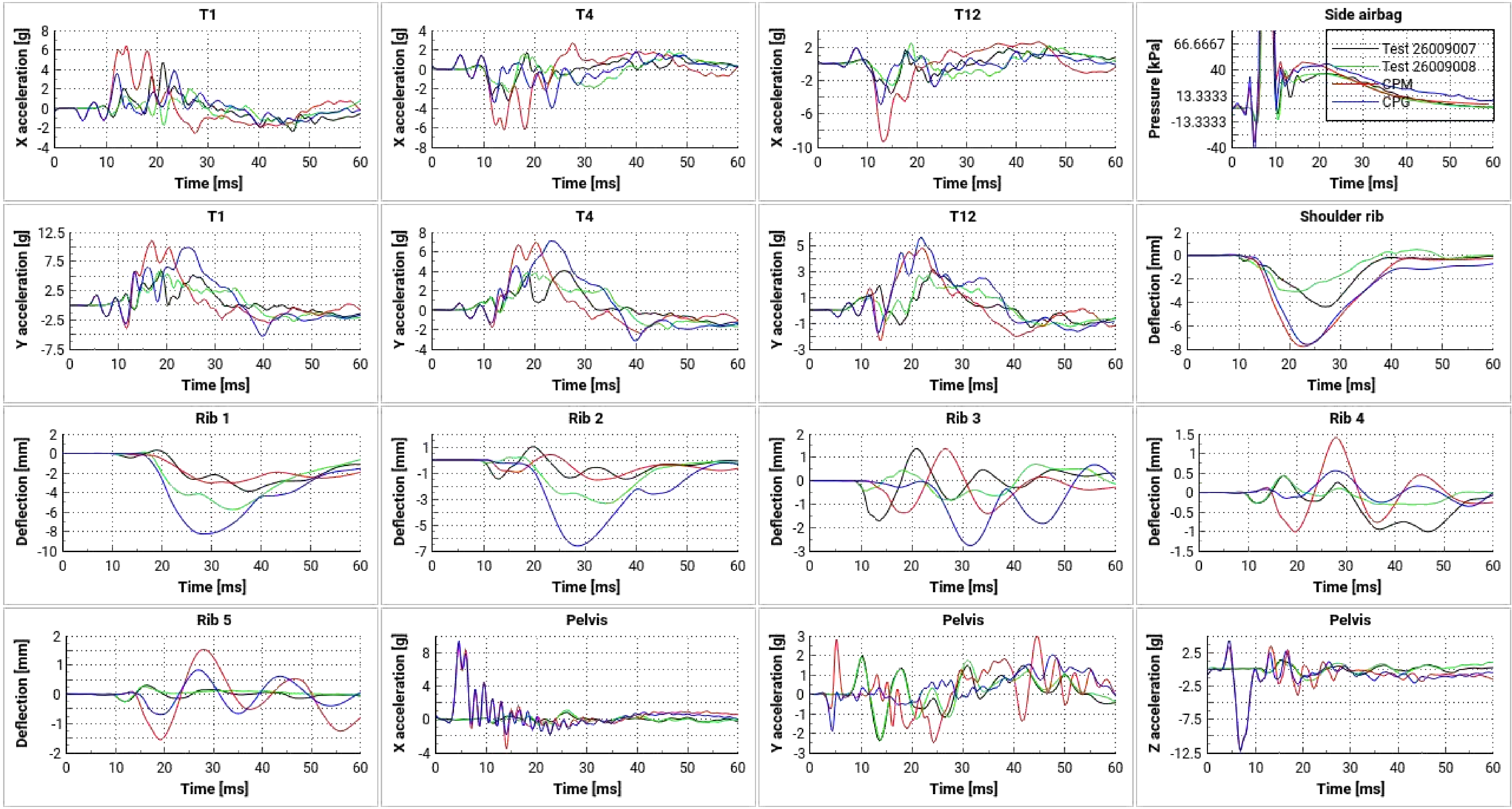

Appendix D V – SID-IIs Full Arm DP 120 mm

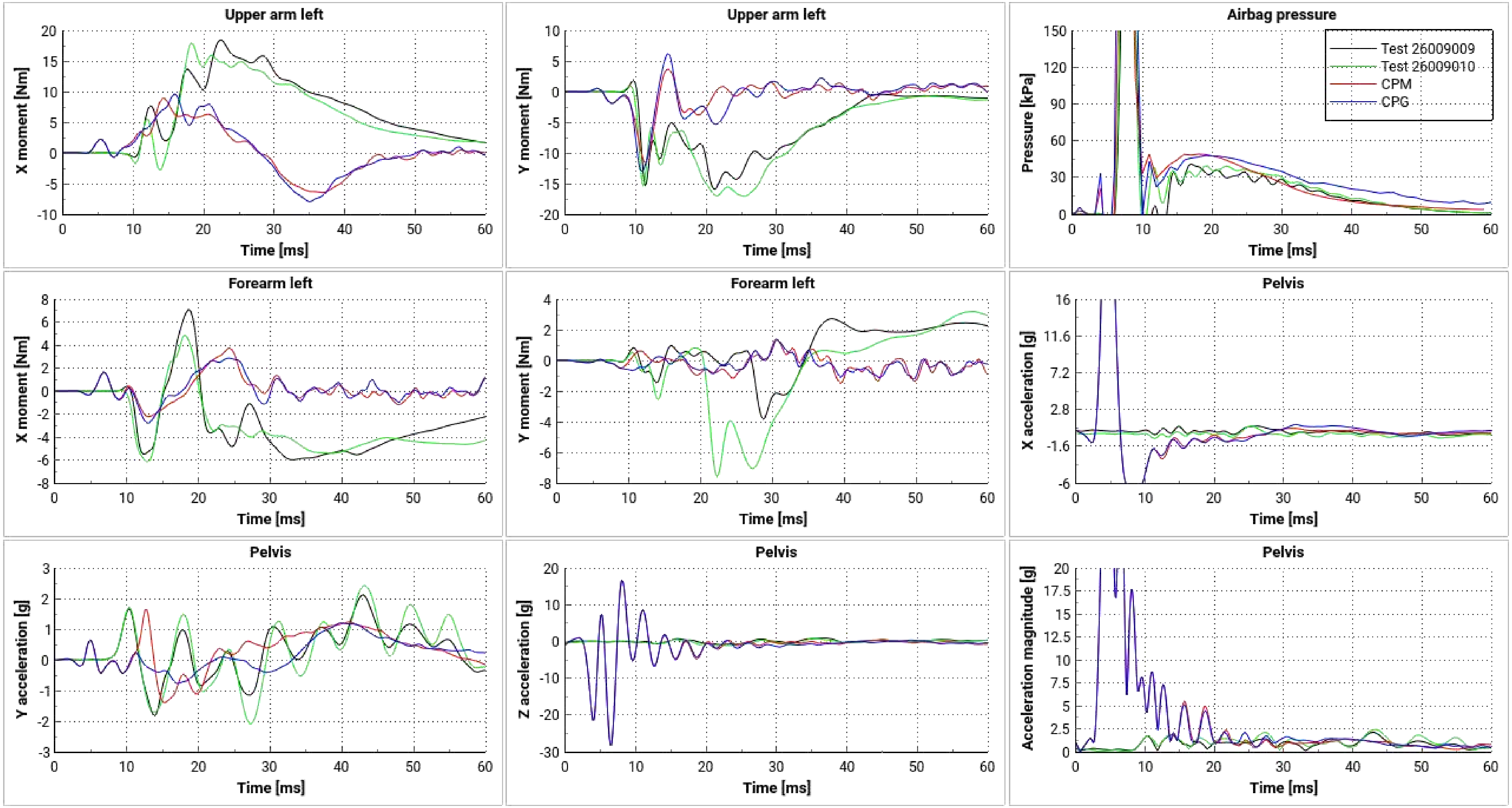

Appendix D VI – SID-IIs Full Arm DP 80 mm

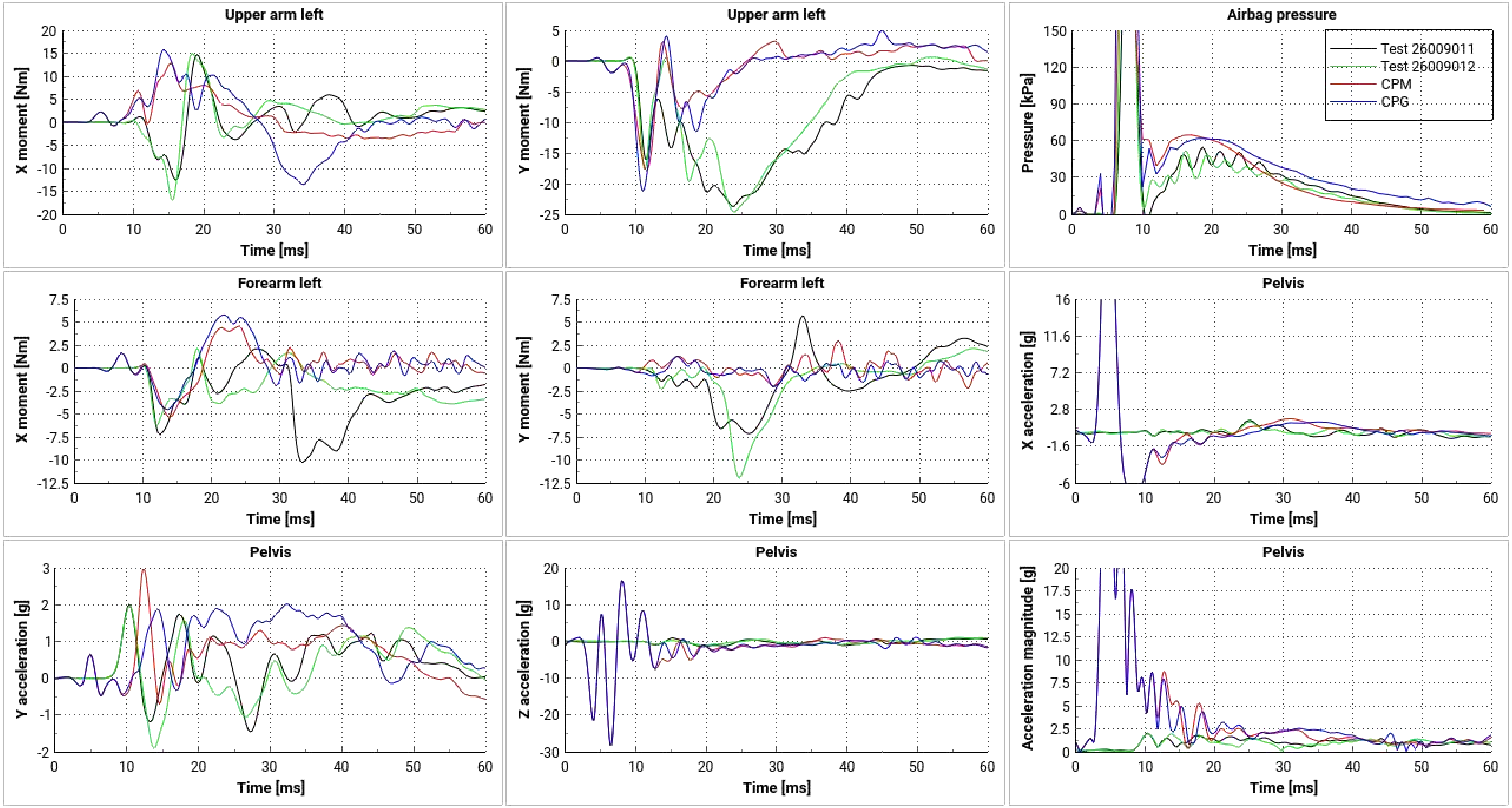

Appendix D VII – SID-IIs Full Arm RP 80 mm

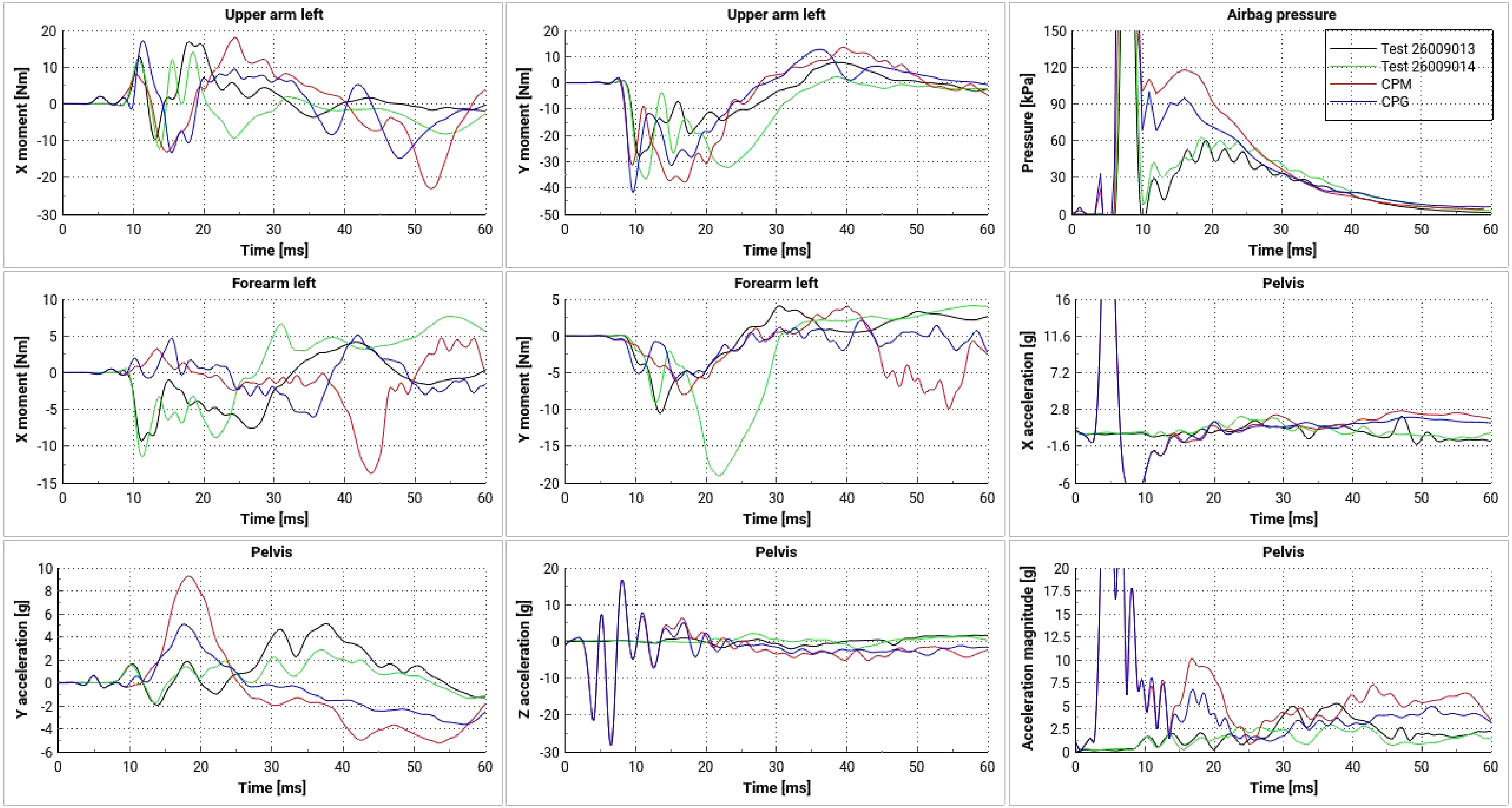

Appendix D VIII – SID-IIs Full Arm RP 120 mm

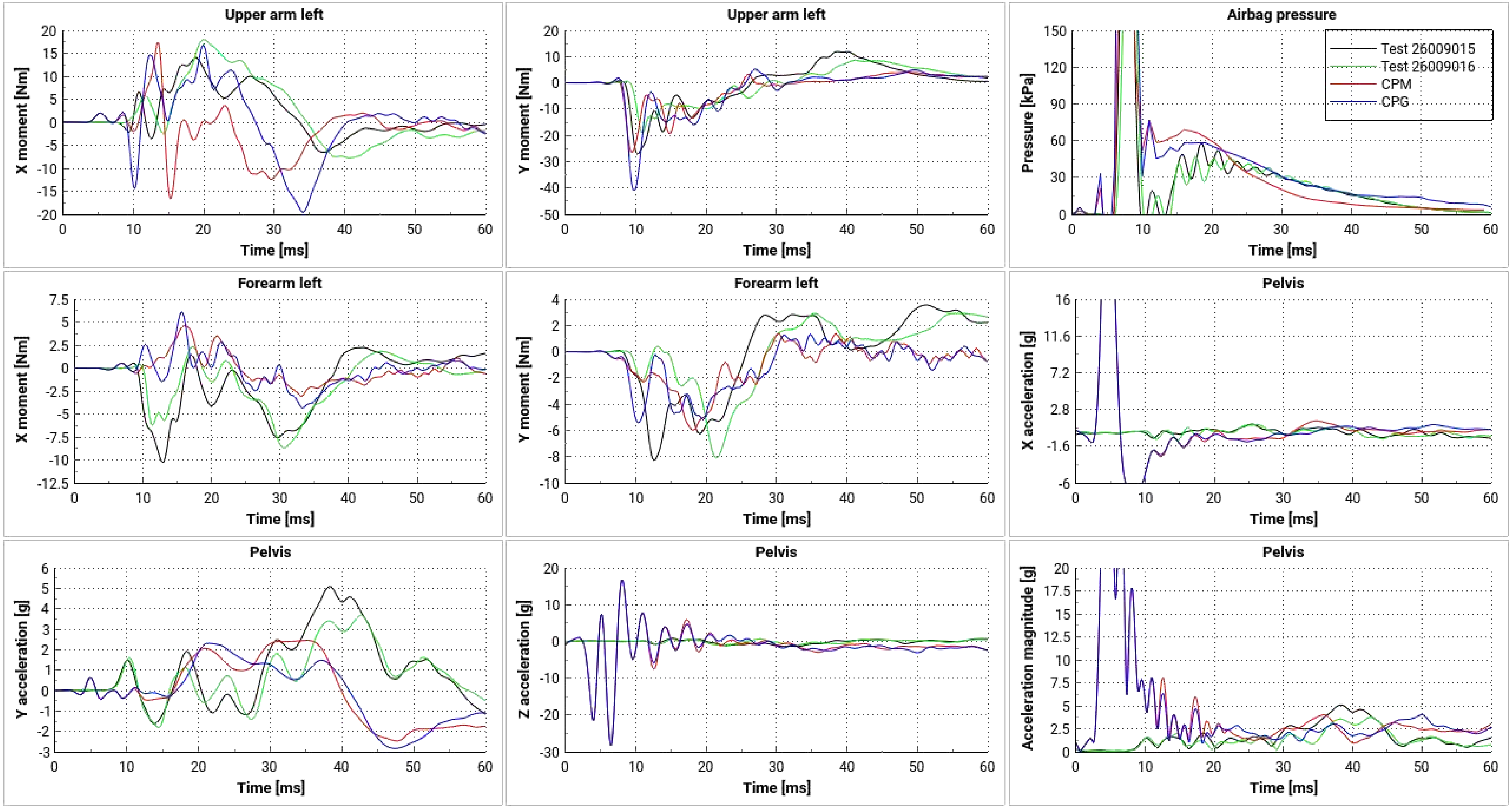

E

Signed Peak Response Summary

The following appendix page summarises the signed peak response values extracted from the final scaled and filtered comparison curves. The peak event was identified from the maximum absolute amplitude of each signal, while the sign of the corresponding response value was retained.

Appendix E I – Signed Peak Response Summary

Signed peak response values for the half-arm test cases.

		WSID50 80 mm				WSID50 120 mm				SID-IIs 80 mm				SID-IIs 120 mm			
Quantity	Unit	Test 1	Test 2	CPM	CPG	Test 1	Test 2	CPM	CPG	Test 1	Test 2	CPM	CPG	Test 1	Test 2	CPM	CPG
T1 X acceleration	g	3.68	3.71	8.06	6.24	4.05	3.97	2.32	1.58	10.52	8.59	10.30	6.59	4.72	1.96	6.40	3.82
T1 Y acceleration	g	8.15	7.54	8.13	9.91	5.87	6.42	4.55	6.41	17.07	11.33	22.61	16.28	5.94	5.79	11.01	9.89
T4 X acceleration	g	3.00	3.30	5.62	4.50	3.50	3.31	1.55	1.27	-7.22	-6.11	-9.97	-6.85	-3.19	-2.34	-6.18	-3.96
T4 Y acceleration	g	6.84	5.06	10.43	10.73	4.81	5.23	4.96	6.20	11.78	7.00	16.26	12.11	4.03	3.88	6.95	7.08
T12 X acceleration	g	2.39	2.47	3.88	3.59	3.09	3.32	3.59	3.59	9.85	-8.49	-13.70	-7.24	-3.57	-2.57	-9.33	-4.89
T12 Y acceleration	g	8.56	9.34	13.65	15.18	3.84	4.32	6.77	3.84	5.78	4.78	11.15	8.98	3.11	2.65	4.76	5.59
Shoulder rib deflection	mm	5.26	6.94	7.56	6.66	3.14	3.07	4.34	4.88	-9.54	-9.58	-14.59	-13.80	-4.38	-3.08	-7.79	-7.61
Rib 1 deflection	mm	4.67	4.79	1.83	1.39	3.83	3.83	1.01	2.79	-2.65	-3.25	-3.46	-8.05	-3.86	-5.76	-3.02	-8.26
Rib 2 deflection	mm	1.26	1.18	7.31	4.14	0.99	0.62	2.21	1.30	-4.77	-2.51	-9.27	-5.29	-1.48	-3.34	-1.54	-6.62
Rib 3 deflection	mm	4.46	5.25	8.50	6.39	2.72	2.14	3.39	1.91	-6.46	-4.33	-12.91	-5.17	-1.70	-0.81	-1.40	-2.77
Rib 4 deflection	mm	4.18	5.51	6.93	5.88	2.25	1.73	2.65	1.78	-3.48	-2.51	-9.74	-3.63	-1.01	0.42	1.41	0.56
Rib 5 deflection	mm	5.25	5.40	6.90	5.57	2.63	2.20	3.07	2.09	-3.28	-1.09	-9.27	-3.40	0.31	0.25	1.55	0.83
Pelvis X acceleration	g	1.69	1.63	2.63	2.85	0.91	0.74	2.98	2.98	1.52	1.67	8.65	8.02	0.81	1.08	8.96	9.38
Pelvis Y acceleration	g	6.26	5.42	6.75	6.61	1.87	1.42	3.82	2.39	1.98	-1.98	-3.86	4.02	-2.36	-2.33	2.99	2.01
Pelvis Z acceleration	g	-2.86	-2.88	4.09	3.97	-1.43	-1.95	-3.06	-3.05	1.58	-1.26	-11.74	-11.91	1.39	-1.67	-11.98	-12.21
Side airbag pressure	kPa	513.77	403.62	371.99	737.87	409.03	263.13	367.84	756.39	463.07	489.68	371.66	762.86	430.02	504.67	364.66	740.76

Signed peak response values for the full-arm test cases.

		Driver 80 mm				Driver 120 mm				Relaxed 80 mm				Relaxed 120 mm			
Quantity	Unit	Test 1	Test 2	CPM	CPG	Test 1	Test 2	CPM	CPG	Test 1	Test 2	CPM	CPG	Test 1	Test 2	CPM	CPG
Upper arm left X moment	Nm	14.66	-16.99	12.83	15.77	18.41	17.88	8.89	9.61	16.92	14.06	-23.00	17.16	14.08	18.03	17.42	-19.55
Upper arm left Y moment	Nm	-23.71	-24.61	-17.83	-21.16	-15.90	-17.07	-11.49	-12.99	-27.92	-36.66	-37.86	-41.64	-27.18	-19.07	-26.42	-41.01
Forearm left X moment	Nm	-10.25	-6.26	-5.34	5.78	7.08	-6.18	3.73	2.86	-9.28	-11.47	-13.68	-6.05	-10.25	-8.67	4.58	6.08
Forearm left Y moment	Nm	-7.13	-11.91	2.96	-2.05	-3.82	-7.58	-1.49	1.33	-10.51	-19.01	-9.93	-6.11	-8.28	-8.11	-5.99	-5.40
Pelvis X acceleration	g	1.48	1.30	37.44	37.23	0.80	0.77	37.27	37.22	1.97	1.98	37.27	37.30	1.04	0.99	37.37	37.29
Pelvis Y acceleration	g	1.99	1.95	2.97	2.01	2.11	2.41	1.65	1.20	5.13	2.87	9.28	5.09	5.09	3.68	-2.47	-2.84
Pelvis Z acceleration	g	-1.45	1.06	-28.40	-28.38	0.91	-1.14	-28.38	-28.40	-2.04	2.16	-28.32	-28.34	1.38	-1.04	-28.31	-28.34
Pelvis acceleration magnitude	g	2.00	1.95	38.76	38.59	2.12	2.42	38.64	38.56	5.25	2.94	38.61	38.65	5.09	3.75	38.70	38.65
Side airbag pressure	kPa	323.68	510.49	379.13	763.75	345.54	464.59	361.95	762.92	411.30	482.70	376.22	750.07	366.01	337.16	368.64	745.12

DEPARTMENT OF MECHANICS AND MARITIME SCIENCES
CHALMERS UNIVERSITY OF TECHNOLOGY
Gothenburg, Sweden 2026
www.chalmers.se

CHALMERS
UNIVERSITY OF TECHNOLOGY